UNIVERSITY OF OKLAHOMA

GRADUATE COLLEGE

ON THE POTENTIAL OF ADAPTIVE BEAMFORMING FOR PHASED-ARRAY WEATHER RADAR

A DISSERTATION

SUBMITTED TO THE GRADUATE FACULTY

in partial fulfillment of the requirements for the

Degree of

DOCTOR OF PHILOSOPHY

By

FENG NAI
Norman, Oklahoma
2017

ON THE POTENTIAL OF ADAPTIVE BEAMFORMING FOR
PHASED-ARRAY WEATHER RADAR

A DISSERTATION APPROVED FOR THE
SCHOOL OF ELECTRICAL AND COMPUTER ENGINEERING

BY

Dr. Robert Palmer, Co-Chair

Dr. Sebastián Torres, Co-Chair

Dr. Nathan Goodman

Dr. Tian-You Yu

Dr. Xuguang Wang

Dedication

To my mother and father, whose enduring support allowed me to focus all my attention on completing my school work. To my grandparents, whose love and wisdom helped me to push through the most difficult times during this journey. To my aunts and uncles, whose brief visit brought me the delicious food I had always missed since I left home. To my cousins, whose competitiveness always drove me to do better and achieve more. To my friends, whose jokes and stories always cheered up my day. To my best friend, Ms. Zhichao Chen, for her encouragement, patience, and unshakable faith in me.

Acknowledgements

I would like to thank my advisors, Dr. Sebasián Torres and Dr. Robert Palmer, who also served as my M. S. advisors. Without their guidance and support, it would not be possible for me to achieve my dream of earning a doctoral degree. From my first day in graduate school, Dr. Torres and Dr. Palmer encouraged me to explore, to read, and to learn as much as possible. When I made progress on my research, no matter how small the advancement was, they always gave me praise and encouragement to keep me motivated. When my research was stuck, they always offered critical analysis and new ideas for me to investigate. More importantly, they always had faith in me to overcome any challenge no matter how insurmountable it seemed at the time. Their patience and understanding allowed me to grow and overcome many of the problems I faced. In my eight years of graduate school, my advisors gave me the opportunity to interact with and to learn from the best role models I can possibly imagine. I would have never become who I am today without the help of my advisors.

I also would like to thank my doctoral committee members, Dr. Tian-You Yu, Dr. Nathan Goodman, and Dr. Xuguang Wang, for their help and support during my years at the University of Oklahoma. Dr. Yu's class on radar engineering taught me the necessary background information on radar systems to understand the importance and nuances of many trade-offs in a radar design.

Dr. Goodman's class on radar signal processing taught me the different approaches to translate radar data from random signals to useful information. I would not be able to complete my research without the solid fundation these classes provided to me.

The journey through graduate school would have been much more difficult without the help of many friends and colleagues in the ARRC. Kenta Hood, who was also a graduate student advised by Dr. Palmer and Dr. Torres, served as my first role model on how to be a graduate student. I will always remember how he printed out and presented his latest results in our weekly meetings. By teaching me how to operate the AIR, Brad Isom set me on the path to spend numerous spring days chasing tornadoes in Oklahoma. David Bodine and Jim Kurdzo are two of the most intelligent and hard-working students I have ever had the pleasure to work with. By operating the AIR together, I learned important teamwork and communication skills from them. Jim's constant drive for perfection and David's calmness are both qualities I respect deeply and aspire to have. My officemate, Fanxing Kong, provided numerous discussions that helped me with my research and future career goals. Redmond Kelly, John Meier, and Matt McCord also provided help to me whenever I needed them, and I am deeply grateful to have known and worked with them.

Finally, it would have been impossible for me to complete this work without the support of my family. My parents, Li Wei and Kang Nai, always

supported me as I spent year after year in school. Without their care and love, it would be easy for me to get distracted and lost along the way. They taught me to be humble, to work hard, and to dedicate myself to my dreams. I would not have succeeded without these important life values. For that, I am deeply thankful.

Contents

List Of Tables

List Of Figures

Abstract

As the Weather Surveillance Radar 1988 Doppler network reaches the end of its expected life, a network of multifunction phased-array radars (MPAR) supporting both aircraft and weather surveillance missions has been proposed. A phased-array system should match the sensitivity, spatial resolution, and data quality of the WSR-88D while having a update time of 60 seconds for weather surveillance. Since an MPAR system must complete both weather and aircraft surveillance missions, the update time reduction provided by having multiple faces is insufficient to achieve the desired 60 second update time for weather surveillance. Therefore, it is likely that multiple simultaneous beams would be needed per face to meet the timeline requirements. An approach to achieve multiple receive beams is to use a spoiled transmit beam and to form a cluster of simultaneous receive beams. However, a significant challenge for this approach is the potential of high sidelobe levels in the two-way radiation pattern, which can result in significantly biased estimates of the radar variables in situations where the signal power has large spatial variation. This dissertation proposes an adaptive beamspace algorithm designed for phased-array weather radar that utilizes a spoiled transmit beam and a cluster of simultaneous receive beams to achieve the desired timeline. Taking advantage of the adaptive algorithm's ability to automatically adjust sidelobe levels to match the scene, the high-sidelobe problem associated with a spoiled

transmit beam is mitigated. Through extensive simulations, it is shown that adaptive beamspace processing can produce accurate and calibrated estimates of weather radar variables. Furthermore, it is demonstrated that the adaptive beamspace algorithm can automatically reject interference signals and reduce their impact on the radar-variable estimates. Additionally, it is shown that, despite higher sidelobe levels, the adaptive beamspace algorithm can perform similarly to a conventional system based on a dish antenna in terms of biases when reflectivity gradients are present. Finally, the adaptive beamspace algorithm is shown to compare favorably to some alternative solutions that can also achieve the desired MPAR timeline requirement while preserving data quality.

Chapter 1

Introduction

Hazardous weather has a long history of causing economic damage to the United States of America (USA). The nation's large size, covering multiple different types of climate, means that the country is subject to floods, draughts, hurricanes, blizzards, tornadoes, hail, and many other types of damaging events. In data compiled by NOAA's National Centers for Environmental Information (NCEI) (2016), the USA has sustained 200 high-damage weather and climate events from 1980 to 2016, where each event has caused damage exceeding one billion dollars. In 2015 alone, there were 10 such events resulting in over 22 billion dollars in damage and over 150 fatalities. In particular, severe storms accounted for half of these events and more than a third of the fatalities. If smaller weather events are taken into account, the total weather-related fatalities raise to more than 500 in 2015 (The U.S. Natural Hazard Statistics 2016). Beyond just damage and deaths, weather and climate also affect the economy of the USA by an estimated 500 billion dollars each year (Lazo et al. 2011). Therefore, it is of vital public interest to be able to forecast and forewarn hazardous weather events to prevent the loss of life and property. The National

Weather Service (NWS), originally the United States Weather Bureau, was first established in 1870 to provide such forecasts and warnings to the population. Since the late 1950s, one important tool used by the NWS to monitor the atmosphere has been a network of weather-surveillance radars. RAdio Detection And Ranging (RADAR) operates by transmitting electromagnetic energy and receiving the energy backscattered by targets of interest. The earliest radars were developed to detect ships and aircraft in the early 1900s (Skolnik 2001). After World War II, radar technology experienced a rapid growth to achieve higher transmit power, expanded volume coverage, and more accurate identification and tracking of targets. One important post-war development was the application of radar to study weather in the 1940s (Doviak and Zrnić 1993).

The first network of weather radars deployed in the USA was the Weather Surveillance Radar 1957 (WSR-57), which provided reflectivity estimates only. Despite the limited information provided by these weather radars, meteorologists were able to identify storm cells to provide warnings for population centers (Rockney 1958; Whiton et al. 1998). In the mid-1970s, the Weather Surveillance Radar 1974 (WSR-74) was deployed across the nation to augment the WSR-57 network to improve forecasts and severe weather warnings (Whiton et al. 1998). After demonstrating that radial velocity information

could bring significant benefits in terms of detecting and forewarning tornadoes (Brown et al. 1978) and microbursts (Wilson et al. 1984; Wolfson et al. 1994), the Weather Surveillance Radar 1988 Doppler (WSR-88D) was developed to be the new weather radar network covering the USA. A total of 159 WSR-88Ds were deployed across the USA to provide long-range weather surveillance (Crum and Alberty 1993). With the upgrade to the WSR-88D, the mean warning lead time for deadly tornadoes increased from 5.3 minutes to 9.5 minutes, and the percentage of warned tornadoes increased from 35% to 60% (Simmons and Sutter 2005). In the early 2000s, research into polarimetric weather radars showed that the additional information allowed for improvements in hydrometeor classification (Bringi and Chandrasekar 2001; Park et al. 2009), rain rate estimation (Ryzhkov et al. 2005a), drop-size-distribution retrieval (Brandes et al. 2004b,a; Cao et al. 2010; French et al. 2015), hail detection (Ryzhkov et al. 2002; Kumjian and Ryzhkov 2008), tornadic debris detection (Ryzhkov et al. 2005b; Bodine et al. 2013), and biological scatterer studies (Chilson et al. 2012; Frick et al. 2012; Horton et al. 2015; Stepanian and Horton 2015). In 2013, all 159 WSR-88Ds were upgraded to include polarimetric capabilities (Crum et al. 2013).

Despite the continued upgrades and improvements to the hardware and software of the WSR-88D, the mechanically rotating dish antenna places a fundamental limit on volumetric update time. With the current volume coverage

patterns (VCP), the WSR-88D can complete a volumetric scan in four to five minutes when observing convective storms (FMH Apr. 2006). It is understood that high-temporal-resolution observations can lead to improved understanding and warning of hazardous weather phenomena (Miller and Kropfli 1980; Carbone et al. 1985). Not surprisingly, a survey of National Weather Service forecasters and television weather forecasters showed that the current update time of four to five minutes for the WSR-88D could miss significant storm evolution and transition. Tornadic storms, squall lines, and downbursts were pointed out as especially problematic due to the coarse temporal resolution of the WSR-88D (LaDue et al. 2010). To address some of the concerns about the slow update time, the Supplemental Adaptive Intra-Volume Low-level Scan (SAILS) has been proposed to improve the update time for the lowest elevations of a volume scan (ROC 2013). Used in conjunction with the Automated Volume Scan Evaluation and Termination (AVSET) (Chrisman 2012), SAILS can almost cut in half the update time for the lowest elevation (0.5° usually) by inserting an additional scan of the lowest elevation angle in the middle of a volume scan. However, providing faster updates only for the lowest elevation is not a perfect solution because there are phenomena that develop in the upper atmosphere that could be missed by SAILS. Also, by inserting additional scans for the lowest elevations, the update time for the entire volume is increased in

some cases. In 2014, the Multiple Elevation Scan Option for SAILS (MESO-SAILS) was proposed that allows the insertion of up to three additional scans of the lowest elevation evenly spaced in the volume scan (Chrisman 2014). The additional scans would significantly improve the coverage of the lower atmosphere, but the update time for the entire volume is further increased and the coverage of the upper atmosphere is sacrificed.

A natural solution to achieve faster update times is to transition from dish-antenna radars to phased-array antenna radars. A phased-array radar uses discrete radiating elements to emulate a continuous distribution that would be applied to a reflector antenna. Each radiating element is excited by signals that have a carefully determined amplitude and phase such that the sum of signals from all the radiating elements produces the desired radiation pattern. Being able to rapidly change the radiation pattern electronically, phased-array radars can execute adaptive scanning strategies much more easily. The National Weather Radar Testbed phased-array radar (NWRT PAR) was developed as a proof-of-concept phased-array weather radar in Norman, OK. By utilizing the electronic steering ability of the PAR and adaptive scanning strategies (Reinoso-Rondinel et al. 2010; Priegnitz et al. 2014), it was shown that the NWRT PAR can achieve 60-second volumetric update times without sacrificing data quality (Heinselman et al. 2008; Heinselman and Torres 2011; Curtis

and Torres 2011; Torres et al. 2016). The 2010 Phased-Array Innovative Sensing Experiment (PARISE) showed that the high-temporal-resolution data from the NWRT PAR resulted in increased tornado warning lead times for weak tornados and increased confidence levels in the data (Heinselman et al. 2012). The 2012 PARISE experiment confirmed that high-temporal-resolution data led to forecasters' improved ability to match the data to their conceptual model for the storms, which resulted in higher confidence levels in the warnings and increased tornado warning lead time (Heinselman et al. 2015). In severe hail and wind events, high-temporal-resolution data improved the probability of detection, lowered the probability of false alarm, and increased the median warning lead-time (Bowden et al. 2015; Bowden and Heinselman 2016).

In addition to the WSR-88D network, the USA also has multiple radar networks supporting aviation missions. The Terminal Doppler Weather Radars (TDWR) are deployed near major airports to detect hazardous weather and wind shear (Michelson et al. 1990), the Airport Surveillance Radar (ASR) series is used for short-range terminal air traffic control, and the Air Route Surveillance Radar (ARSR) series is used for long-range air route surveillance. Operating, maintaining, and upgrading multiple single-mission radar networks is costly. As the WSR-88D network reaches the end of its expected life, there is an opportunity to use a network of multifunction radars to replace several single-mission radar networks; this would significantly reduce

the number of radars and the associated maintenance cost. A network of multifunction phased-array radars (MPAR) supporting both aircraft and weather surveillance missions has been proposed (Weber et al. 2007; Zrnić et al. 2007; Weadon et al. 2009). An MPAR system should to match the sensitivity, spatial resolution, and data quality of the WSR-88D while having a update time of 60 seconds for weather surveillance; it is also required to have the same revisit time and minimum detectable signal as the current air traffic control radars (FAA 2013). Assuming MPAR has four faces that can be operated independently, a quick calculation shows that reducing the WSR-88D update time (four to five minutes) by a factor of four is not enough to meet MPAR's weather surveillance update time requirements since the radar must also allocate time for aircraft surveillance missions. A potential solution to meet the timeline requirement for MPAR is to utilize multiple receive beams, which has already been exploited by the wind profiling radar community (Palmer et al. 1998; Cheong et al. 2004). Calculations in Zrnić et al. (2015) showed that a four-faced MPAR radar would need to transmit and receive three beams per face to achieve the desired timeline. To achieve the required receive beams, a multiple-frequency (Weber et al. 2007), time multiplexing (Melnikov et al. 2015), spilt transmit beam (Fadlallah et al. 2008), or spoiled transmit beam (Isom et al. 2013) approach can be used. Figure 1.1 illustrates a multiple

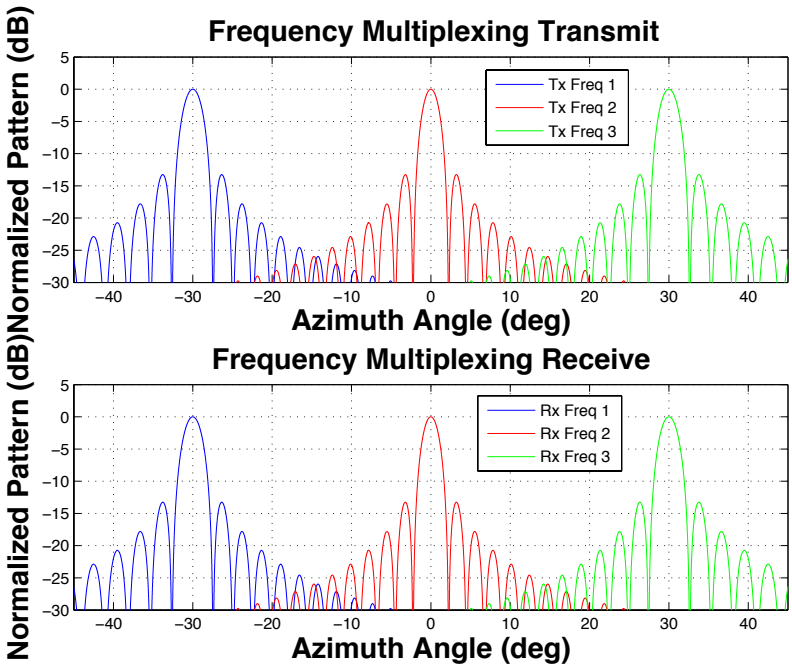

Figure 1.1: Illustration of the multiple frequency approach to achieve multiple receive beams. The different colors correspond to beams operating on different frequencies. The three transmit beams (top) and receive beams (bottom) are steered to -30°, 0°, and 30° respectively. The downside of this approach is that the bandwidth requirement is large.

frequency approach where three beams with different frequencies are transmitted sequentially and steered to scan in different directions. The top panel of Figure 1.1 shows the radiation patterns of three transmit beams operating with different frequencies (different color) and scanning in different directions. The bottom panel shows the receive beams that are steered in the direction of the transmit beam with the matching frequency. Essentially, three independent radars are operating at the same time sharing a single antenna. A significant downside to this multiple frequency approach is that it requires a large bandwidth to operate, which is an expensive resource.

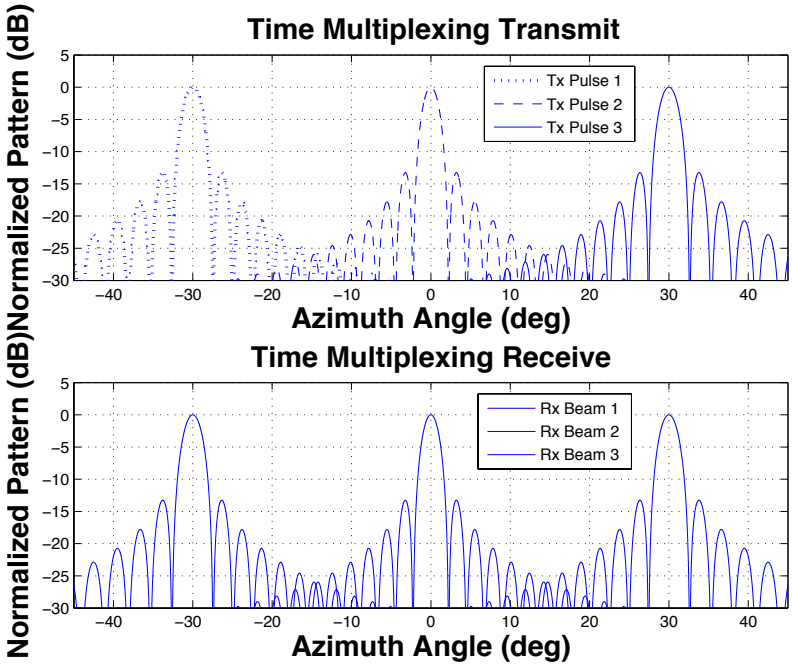

Figure 1.2: Illustration of time multiplexing approach to achieve multiple receive beams. Transmit beams pointed in different directions are transmitted in succession, and the receive beam is formed to receive simultaneously from all illuminated directions. This approach increases the blind range of the radar and can only be used with short transmit pulses.

Instead of multiple frequencies, it is possible to transmit successive pulses in different directions and receive from all those directions simultaneously. This time multiplexing approach is illustrated in Figure 1.2, where the top panel shows the three successive transmit beams pointed in different directions and the bottom panel shows the receive beam that receives simultaneously from the three directions illuminated by the succession of transmit beams. Signal processing techniques can be used to mitigate cross-beam contamination, but the successive transmissions increase the blind range of the radar and require short transmit pulses (Melnikov et al. 2015).

Other approaches take advantage of the ability of a phased-array radar to synthesize desirable beam patterns. The split transmit beam approach utilizes a transmit beam with multiple mainbeams as shown in the top panel of Figure 1.3. The key difference between Figures 1.3 and 1.2 is that the energy is radiated toward -30°, 0°, and 30° simultaneously in the split transmit beam approach. The receive beam in this approach also receives simultaneously from all directions illuminated by the transmit beam. One obvious downside to this approach is the loss of sensitivity due to the spreading of energy in multiple directions. Moreover, it is difficult to synthesize and maintain the required beam pattern to reduce contamination from different directions.

Instead of using a transmit beam that illuminates directions that are far apart, it is possible to generate a spoiled transmit beam that illuminates a large volume where a cluster of receive beams can be formed within the illuminated volume. Figure 1.4 illustrates this spoiled transmit beam approach. In this example, the spoiled transmit beam (top panel) illuminates a volume where three simultaneous receive beams (bottom panel) can be formed. The loss of sensitivity is similar to that of the split transmit beam approach, but it is much easier to synthesize and maintain the types of transmit and receive beams in this approach. However, a significant disadvantage of using a spoiled transmit beam and simultaneous receive beams is that the two-way radiation pattern sidelobe levels are high because they are mainly determined by the (one-way)

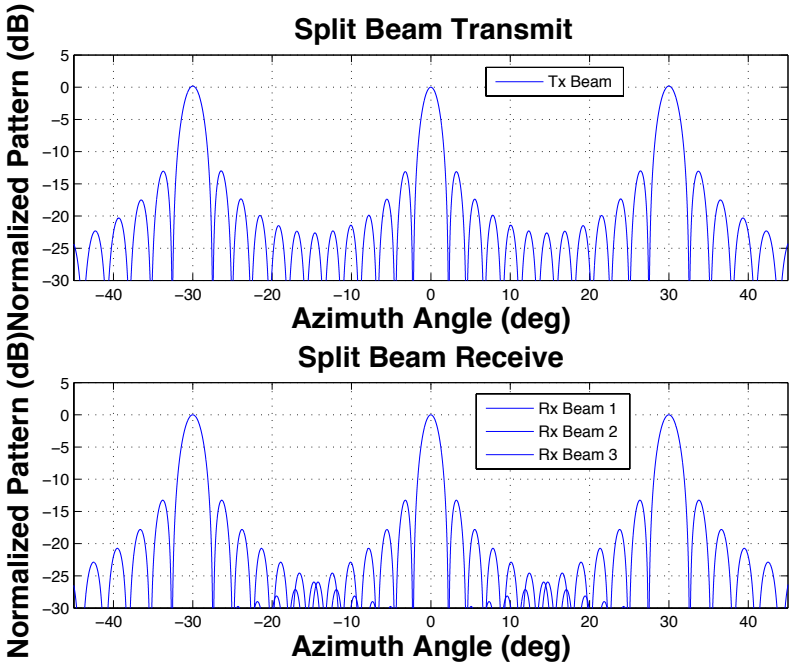

Figure 1.3: Illustration of split transmit beam approach to meet the timeline requirement. A transmit beam that illuminates multiple directions is used, and the receive beam is formed to receive simultaneously from all illuminated directions. A sensitivity loss is expected since energy is spread over multiple directions. Difficulties to synthesize and maintain the required beam pattern are also concerns.

sidelobe levels of the receive beams. The spoiled transmit beam is also more likely to illuminate unwanted clutter targets. This, combined with the high sidelobe levels of the two-way pattern, means that estimates of radar variables are more likely to be biased. Traditionally, aggressive tapering is used to drive down the sidelobe levels of the receive beams, which leads to loss of spatial resolution and sensitivity (Harris 1978). A potential solution to this sidelobe issue with spoiled transmit beams is to take advantage of a digitized phased-array weather radar's capability to change the receive radiation pattern via

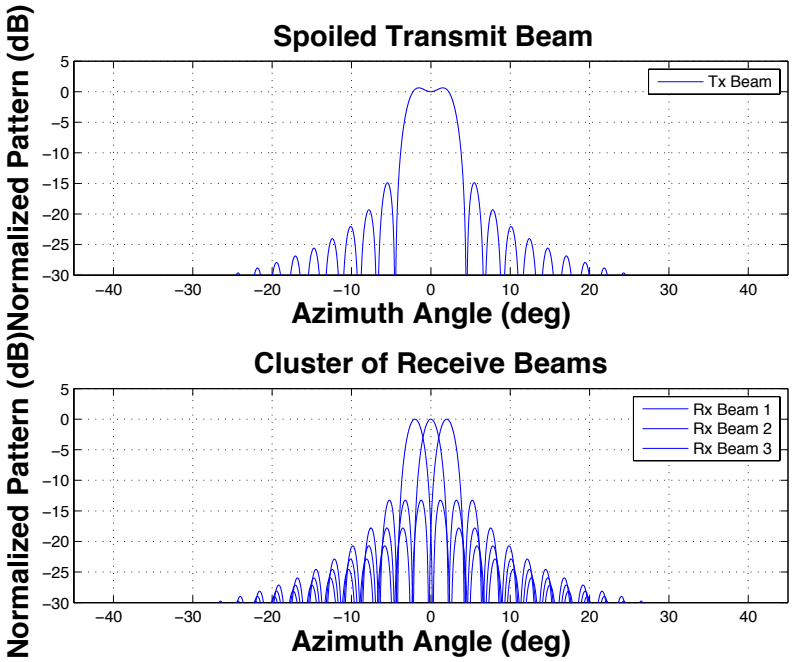

Figure 1.4: Illustration of the spoiled transmit beam approach to meet the timeline requirement. A transmit beam that illuminates a large volume is used, and a cluster of simultaneous receive beams is formed within the illuminated volume. A sensitivity loss similar to the split transmit beam approach is expected, but the required beam pattern is easier to synthesize and maintain in this approach. However, the sidelobe levels become a major concern for weather radars.

adaptive beamforming, which can help reject unwanted interference signals through spatial filtering (Stoica and Moses 2005).

Many adaptive beamforming methods have been developed in the literature for applications involving signals that can be modeled as point sources (Stoica and Moses 2005; Capon 1969; Er and Cantoni 1985; Cox et al. 1987;

Li et al. 2003, 2004; Elnashar et al. 2006; Lie et al. 2010). The minimum-variance distortionless response beamformer, also known as the Capon beamformer (Capon 1969), forms the foundation of many later versions of adaptive beamforming algorithms. Many authors recognized that the Capon beamformer is sensitive to errors in the steering vector and proposed alternative methods to improve its robustness. Diagonal loading quickly became a well-known method to control the white-noise gain and improve the robustness of the beamformer (Stoica and Moses 2005), but in many cases, the choice of the loading factor is ad-hoc and has no theoretical basis. A method that uses an uncertainty set to calculate the optimum loading factor was proposed in Li et al. (2003), but the parameter controlling the size of the uncertainty set becomes another data-independent parameter. Furthermore, the majority of the existing adaptive beamforming algorithms in the literature are designed to detect and reject a finite number of point targets. However, for weather radars, the signal of interest is from distributed targets, namely the hydrometeors that fill spaces much larger than the radar resolution volume. Thus, direct application of adaptive beamforming methods intended for point sources to weather radars could lead to significant biases in estimated radar variables (Nai et al. 2013a; Yoshikawa et al. 2013). A minimum-mean-squared-error (MMSE) framework to iteratively estimate the weather signal was developed by Yoshikawa et al. (2013). One advantage of the MMSE approach is that it can produce accurate

estimates with limited samples, unlike methods based on inverting the sample covariance matrix that require a number of samples large enough to ensure the sample covariance matrix is not singular. However, the iterative nature of the MMSE method means it is computationally complex and time consuming, and is best suited for offline processing instead of real-time implementations. In an attempt to reduce the number of samples needed for adaptive beamforming, approaches based on the concept of beamspace were proposed (Chapman 1976; Bienvenu and Kopp 1984; Brookner and Howell 1986; Li and Liu 1994). Some classical direction-of-arrival estimation methods, such as MUSIC and ESPIRT, have been adapted to operate in beamspace as well (Zoltowski et al. 1993; Xu et al. 1994). More recently, adaptive beamspace beamforming also has found application in medical imaging (Rodriguez-Rivera et al. 2006; Nilsen and Hafizovic 2009), sonar (Somasundaram 2011), communications (Vook et al. 2013), and radar (Li and Lu 2006; Hassanien and Vorobyov 2009; Lamare et al. 2010). The essential property of adaptive beamspace processing is the reduction of data dimensionality via pre-processing. Instead of applying the adaptive algorithm to the output of the receive channels directly, beamspace methods first form a set of non-adaptive beams, where the number of beams formed is usually much smaller than the number of receive channels. By feeding the output of the non-adaptive beams (instead of the output of the receive

channels) into an adaptive algorithm, the dimensionality of the problem in the adaptive step can be significantly reduced.

This dissertation proposes an adaptive beamspace algorithm designed for phased-array weather radar that utilizes a spoiled transmit beam and a cluster of simultaneous receive beams to achieve the desired timeline. Taking advantage of the adaptive algorithm's ability to automatically adjust sidelobe levels to match the scene, the high-sidelobe problem associated with a spoiled transmit beam is mitigated. Chapters 2 and 3 will provide background information on weather radars and phased-array radars. Chapter 4 will describe the proposed adaptive beamspace algorithm in detail, and will show that adaptive beamspace processing can produce accurate and calibrated estimates of weather radar variables through extensive simulations. Furthermore, simulation results in Chapter 4 will show that the adaptive beamspace algorithm can automatically reject interference signals and reduce their impact on the radar-variable estimates, and it can perform similarly to a low-sidelobe dish antenna system in terms of data loss due to large biases when reflectivity gradients are present despite the higher sidelobe levels. Finally, in Chapter 5, the adaptive beamspace algorithm will be shown to compare favorably to some alternative solutions that can also achieve the desired MPAR timeline requirement. Conclusions and future work will be discussed in Chapter 6.

Chapter 2

Weather Radar Fundamentals

Weather radars, such as the WSR-88D, are some of the most advanced instruments available to remotely observe the atmosphere. By radiating pulses of electromagnetic energy at microwave frequencies and collecting information about the atmosphere based on the energy backscattered to the radar by hydrometeors or other targets, weather radars are capable of monitoring severe weather and producing advanced measurements that can further our understanding of the atmosphere (Serafin and Wilson 2000). The spectral moments (and more recently the polarimetric variables) are the fundamental weather radar measurements that are used by operational forecasters and as inputs to many automatic algorithms, such as quantitative precipitation estimation (QPE) and mesocyclone detection. Signals from non-meteorological scatterers, also referred to as clutter, can bias the measurements from the signals of interest and must be mitigated to ensure the quality of radar products. To better understand how a weather radar functions, this chapter will first discuss the basic components of a weather radar. Then the discussion will focus on the signal processing techniques required to accurately estimate the statistical

properties of the targets. Lastly, the current scanning strategies and the need for faster update times for the next generation of weather radars are presented.

2.1 Fundamentals of Radar Design

A weather radar is generally composed of three major components: the transmit chain, the antenna, and the receive chain. A simplified block diagram of a Doppler radar is shown in Figure 2.1. In Figure 2.1, the pulse modulator and power amplifier form the transmit chain of the radar; and the mixers, low-pass filters (LPF), and signal processing unit form the receive chain. Each major component will be discussed in detail next.

2.1.1 Transmit Chain

The transmit chain starts with the stable local oscillator (STALO), which generates a continuous-wave signal at a fixed radio frequency. This signal is denoted by $f(t)$ in Figure 2.1 and can be expressed as

$$f(t) = \cos(2\pi f_o t + \psi_t), \tag{2.1}$$

where f_o is the carrier frequency, t is time, and ψ_t is the initial transmitter phase. After the continuous-wave signal is generated, it is modulated by a pulse signal given by

$$u(t) = \begin{cases} 1 & 0 \leq t \leq \tau \\ \\ 0 & \text{otherwise} \end{cases}, \tag{2.2}$$

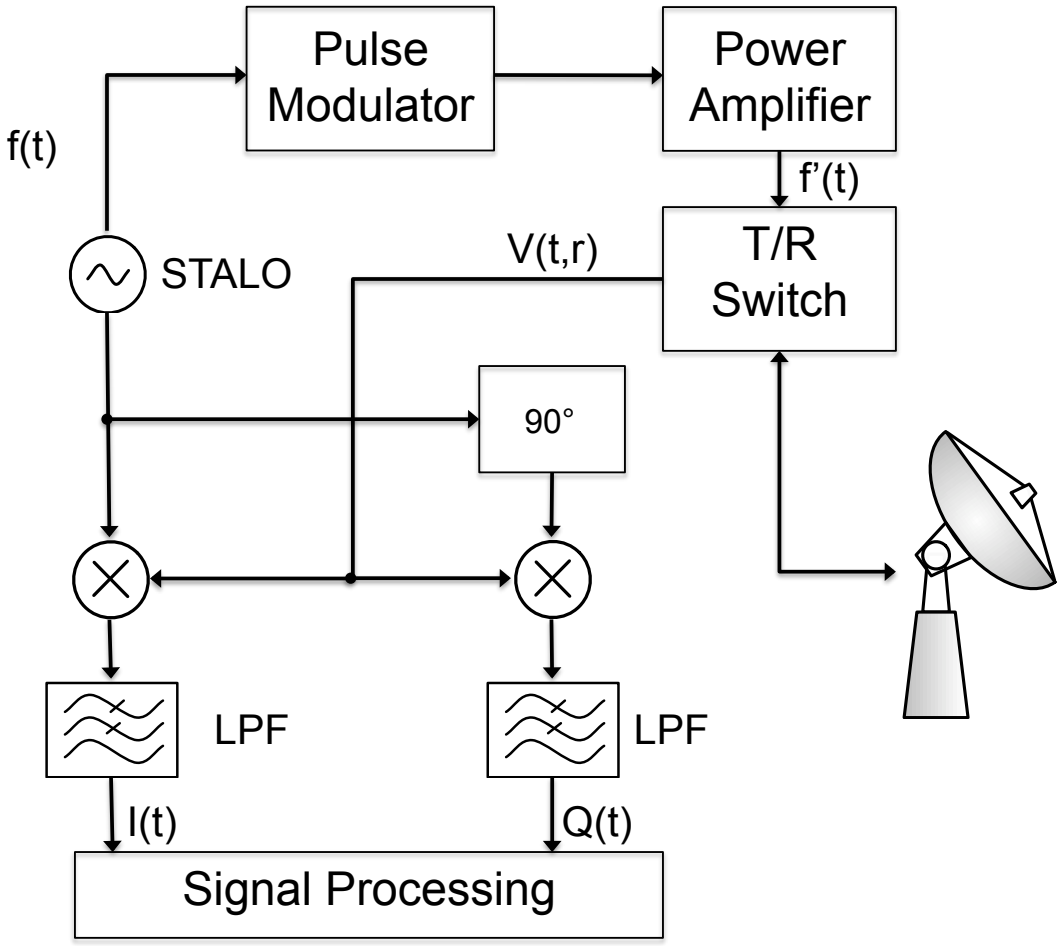

Figure 2.1: Simplified weather radar block diagram. A continuous wave at the desired frequency is generated by the STALO. It is then modulated and amplified before being radiated into the atmosphere. The received signal is demodulated and filtered into in-phase and quadrature components for processing (adapted from Doviak and Zrnić 1993).

where τ is the pulse width. The pulse width is an important factor in determining several key features of a radar. First of all, the pulse width is related to the sensitivity of the radar, which describes the weakest backscattered signal that a radar can detect and extract useful information from. For weather radars, high sensitivity is especially important because it allows the radar to observe phenomena such as gust fronts and clear-air scattering. Secondly, the pulse width also determines the range resolution of the radar when it is transmitting single-frequency waveforms. The range resolution for point target radars, which is the minimum distance separating two targets that allows the radar to distinguish the two targets, is given by

$$\Delta r = \frac{c\tau}{2} \tag{2.3}$$

where Δr is the range resolution, and c is the speed of light. The range resolution for weather radars are determined by the 6-dB width of the range weighting function described in later sections. Finally, for a monostatic radar (i.e., the same antenna is used for both transmit and receive), the pulse width also determines the blind range since the radar cannot typically receive while transmitting. The blind range is given by

$$r_b = \frac{c\tau}{2} = \Delta r \tag{2.4}$$

Trade-offs between sensitivity, range resolution, and blind range must be considered when selecting a pulse width. To improve the sensitivity, a longer

pulse is desirable since more energy would be radiated by the radar. However, a long pulse also lengthens the blind range and worsens the range resolution. One possible way to address this dilemma is to use pulse compression, which transmits a long pulse with frequency or phase modulated waveforms. For such advanced waveforms, the range resolution is no longer proportional to the pulse width. Instead, it is determined by the bandwidth of the modulated waveform (Skolnik 2001). This allows for good sensitivity and range resolution to be achieved simultaneously. The increased blind range can be mitigated using a short fill pulse (Cheong et al. 2013).

The pulse modulated signal must be amplified to the desired power level before being radiated into the atmosphere through the antenna. There are many types of power amplifiers, and Table 2.1 lists the advantages and disadvantages of some common types. Klystron amplifiers with a large peak power are used by the WSR-88D to generate pulses with good spectral purity (i.e., power is not spread to frequencies other than the intended frequency band) (Doviak and Zrnić 1993). Another type of transmitter is the magnetron, which has a smaller size and operates at lower voltages compared to the Klystron amplifier. However, the transmit phase from a magnetron is not constant between transmitted pulses, and spectral leakage can occur (Skolnik 2001). Both Klystrons and magnetrons can generate peak powers in the megawatt range, which is ideal for a pulsed radar. Solid-state power amplifiers (SSPA) usually produce

much lower power and, multiple devices are typically needed to generate the required power for weather radars. Due to their small size and lower cost, SSPA are ideal for active phased-array systems that require transmitters for each individual radiating element. Both Klystron amplifiers and SSPAs provide a stable transmit phase (ψ_t) from pulse to pulse, which is necessary for Doppler processing (Skolnik 2001). After power amplification, the signal is radiated into space through the antenna, which is discussed next.

Table 2.1: Comparison of common power amplifiers used in radar systems.

Transmitter Type	**Advantages**	**Disadvantages**
Klystron	High power Steady phase	Large size High cost
Magnetron	High power Inexpensive	Spectral leakage Random phase
Solid-state power amplifier (SSPA)	Small size Steady phase Low distortion Inexpensive	Low power

2.1.2 Antenna

The antenna of a radar system focuses the radiated power into a certain direction (or beam) on transmit and allows the radar to accurately determine the location of a target in azimuthal and elevation direction. Furthermore,

concentrating the radiated power into a beam also allows the radar to detect targets that are farther away from the radar compared to when the power is radiated isotropically. On receive, the antenna can act as a spatial filter to attenuate backscattered signals from directions other than the direction of interest. The function that describes the distribution of radiated power is known as the radiation pattern (also referred to as the beam pattern). Some common types of antenna include dipole, patch, reflector, phased-array, and many more. Figure 2.2 shows a parabolic reflector (dish) antenna used by WSR-88D, Figure 2.3 shows a fan beam reflector antenna used by airport surveillance radar (ASR), and Figure 2.4 shows a phased-array antenna. The phased-array antenna is based on the concept of using many discrete radiating elements to simulate a continuous distribution of currents. The ability to control the amplitude and phase of each radiating element gives the phased-array antenna greater flexibility to synthesize a desired beam pattern to help the radar fulfill its missions.

There are some important parameters that are used to descibe an antenna beam pattern, as shown in Figure 2.5. The main lobe refers to the peak of the pattern pointed toward the direction of interest, and sidelobes refer to any peaks in the pattern other than the main lobe. In Figure 2.5, the peak of the main lobe is pointed at 0° and is normalized to have unit gain (0 dB). The 3-dB beamwidth refers to the angular spread between the points where the radiated

Figure 2.2: S-band parabolic reflector antenna used by the WSR-88D (Ice et al. 2015). This dish antenna has a diameter of 8.53 m and produces a beam with 0.93° 3-dB beamwidth with low sidelobes. The antenna is to be rotated in azimuth and tilted in elevation to allow the narrow beam, also referred to as a "pencil" beam, to scan an entire volume.

power is 3 dB below the peak of the main lobe (indicated by the red dashed line). For point target radars, the 3-dB beamwidth determines the minimum separation that is required between two targets with the same backscattering cross section that the radar can successfully distinguish. For distributed targets of interest to a weather radar, the 3-dB beamwidth of the two-way radiation pattern determines the angular dimension of the resolution volume. The range dimension of the resolution volume is determined by the 6-dB width of the range weighting function that will be described in the next section.

Antenna sidelobes determine how much power is being radiated towards directions other than the direction of interest. Since any received signal is assumed to be backscattered from targets in the direction of the main lobe,

Figure 2.3: S-band ASR antenna (courtesy of Wiley/Wilson). This antenna produces a beam that is narrow in the azimuth dimension and wide in elevation dimension, which is commonly referred to as a “fan” beam. By having a wide beamwidth in elevation, the radar can complete a volume scan by only rotate in azimuth. This allows for faster updates but the position of the target in elevation cannot be accurately estimated.

Figure 2.4: Phased-array antenna for the National Weather Radar Testbed in Norman, OK. This antenna is composed of 4352 radiating elements, and it can electronically steer the beam to $\pm 45^{\circ}$. The 3-dB beamwidth is 1.5° at broadside (the direction that is normal to the plane of the array) and widens to 2.1° when steered to 45°. The ability to electronically steer the beams allows for adaptive scanning strategies that focus on regions of interest to provide faster updates (Zrnić et al. 2007).

the ideal beam pattern would have no sidelobes, but such a pattern cannot be achieved in a real antenna. To prevent targets located in the directions of the sidelobes from contaminating signals from targets in the direction of the main lobe, the sidelobe levels should be as low as possible, especially for weather radars that deal with storms that cover a large volume of space and have a large dynamic range. It is possible for a weather radar to encounter cases where volumes of space with little to no hydrometeors are adjacent to volumes with large hail and raindrops. When the main lobe is pointed at the volume with no hydrometeors, the backscattered signal from adjacent volumes can "leak" through the sidelobes of the pattern and appear to be from the main lobe, which could introduce biases in the radar variables.

2.1.3 Receive Chain

After transmitting the electromagnetic energy, the radar begins to receive backscattered signals. For a single scatterer at range r, the received signal has the form

$$V(t,r) = |A| \cos\left[2\pi f_o\left(t - \frac{2r}{c}\right) + \psi_t + \psi_s\right] u\left(t - \frac{2r}{c}\right), \qquad (2.5)$$

where $|A|$ is the amplitude of the received signal, and ψ_s is the phase introduced by the scatterer. The received signal can be considered as the real part of a complex phasor signal, which is written as

$$V(t,r) = |A| \exp\left[j2\pi f_o\left(t - \frac{2r}{c}\right) + j\psi_t + j\psi_s\right] u\left(t - \frac{2r}{c}\right), \qquad (2.6)$$

$$V(t,r) = I(t,r) + jQ(t,r), \qquad (2.7)$$

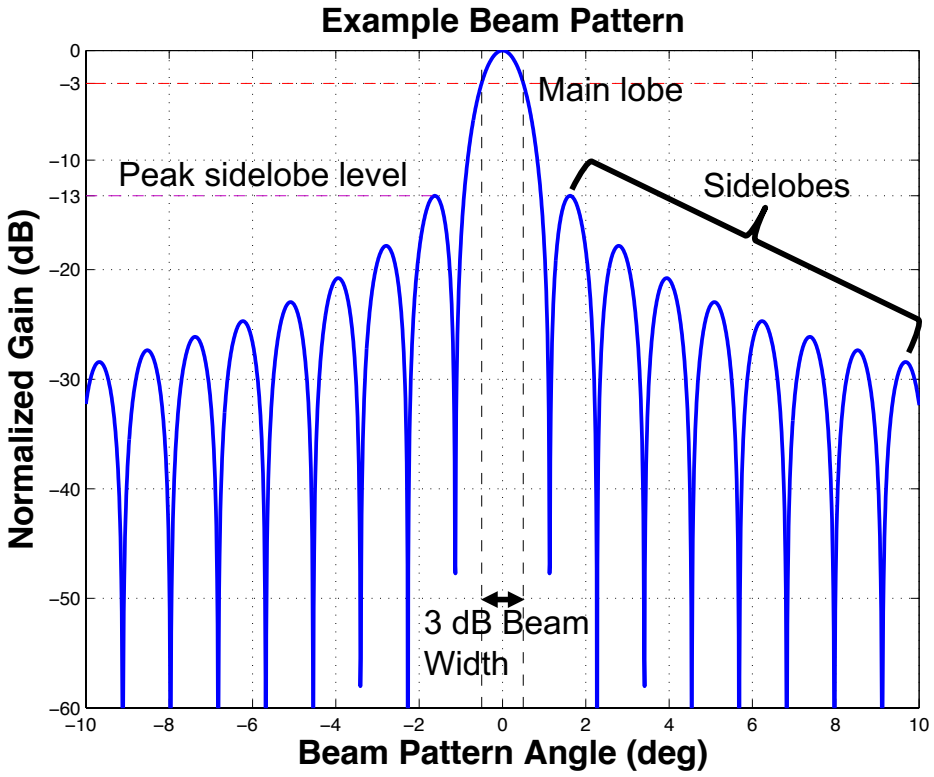

Figure 2.5: Example beam pattern showing parameters used to describe it. The main lobe is the peak of the pattern that is pointed in the direction of interest (0° in this example), and sidelobes are the other peaks in the pattern. The 3-dB beamwidth is the angular separation between the point where the radiated power is 3 dB (red dashed line) below the peak of the mainlobe, and it determines the angular resolution of the radar. By having low sidelobes, the antenna can spatially filter out signals arriving from directions other than the direction of interest.

where j is $\sqrt{-1}$, $I(t,r)$ is the in-phase component, and $Q(t,r)$ is the quadrature component. The block diagram in Figure 2.1 shows that $I(t,r)$ is generated by mixing the received signal with a reference signal generated by the STALO followed by a low-pass filter. $Q(t,r)$ is generated in the same way as $I(t,r)$ except that the second input to the mixer is a 90° phase-shifted STALO reference signal. The low-pass filters (LPF) following the mixers remove the high-frequency components generated during the mixing process and keep the baseband signals. Mathematically, $I(t,r)$ and $Q(t,r)$ are expressed as

$$I(t,r) = \frac{|A|}{\sqrt{2}} \cos\left(\frac{4\pi r}{\lambda} - \psi_t - \psi_s\right) u\left(t - \frac{2r}{c}\right) \tag{2.8}$$

and

$$Q(t,r) = \frac{-|A|}{\sqrt{2}} \sin\left(\frac{4\pi r}{\lambda} - \psi_t - \psi_s\right) u\left(t - \frac{2r}{c}\right), \tag{2.9}$$

where λ is the wavelength of the carrier. The $\frac{1}{\sqrt{2}}$ term is a scaling factor so that the sum of average signal powers in $I(t,r)$ and $Q(t,r)$ is equal to the average signal power of $V(t,r)$ over a cycle of the microwave signal. The phase of the complex received signal is

$$\psi_e(t) = -\frac{4\pi r}{\lambda} + \psi_t + \psi_s \tag{2.10}$$

and its time derivative is

$$\omega_d = \frac{\mathrm{d}\psi_e}{\mathrm{d}t} = -\frac{4\pi}{\lambda}\frac{\mathrm{d}r}{\mathrm{d}t} = -\frac{4\pi}{\lambda} v_r, \tag{2.11}$$

where ω_d is the Doppler shift measured in radians per second and v_r is the Doppler velocity, also referred to as the radial velocity of the scatterer. The

accepted convention in the weather radar community is that a scatterer moving towards the radar will have a positive Doppler shift and a negative radial velocity.

The previous discussions assumed an ideal system; in any real system, there is always noise in addition to the signal of interest. A matched filter is usually used to enhance detection of the signal in noise (Skolnik 2001). To process the match filtered signal, the $I(t,r)$ and $Q(t,r)$ signals are sampled in range and sample time. Each sample in range time represents the combined backscattering of particles in a volume of space called the "resolution volume". The location of each resolution volume is determined by

$$r_0 = \frac{c\tau_s}{2}, \tag{2.12}$$

where r_0 is the range to the resolution volume, and τ_s is the range-time sampling delay after transmitting a pulse. The range depth of each resolution volume is controlled by the range weighting function $|W(r)|$, which is the response of the matched filter to a transmitted pulse (Doviak and Zrnić 1993). The backscattered signal from scatterers located near the peak of the range weighting function are weighted more than the backscattered signals from scatterers located at the edge of the range weighting function. The 3-dB point of the range weighting function determines the range extent of a resolution volume, and, for a rectangular transmitted pulse, it is approximately given by Equation (2.3).

The angular width of the resolution volume depends on the 3-dB beamwidth of the antenna and the range of the resolution volume. Each sample along range time corresponds to a different resolution volume, which is also referred to as a range gate. Weather radars are not only capable of measuring the range to the scatterers, they can also measure their radial velocity.

The radial velocity of the scatterers is directly proportional to the frequency of the baseband $I(t,r)$ and $Q(t,r)$ signals as shown in Equation (2.11). Since $I(t)$ and $Q(t)$ (the r dependence is dropped when considering a single resolution volume) have much longer period than the pulse width, the change in $I(t)$ and $Q(t)$ during a single pulse is extremely small and cannot be used to determine the frequency of the baseband signal. A solution is to transmit multiple equally spaced pulses to sample the baseband signal (in sample time) and to use the samples to measure the radial velocity of the scatterers. The pulse repetition time (PRT), T_s, controls the time between transmitted pulses. To successfully recover the baseband signal from the sampled signal, the Nyquist sampling theorem requires that the sampling frequency, $f_s = 1/T_s$, is at least twice the highest frequency of the signal being sampled; otherwise, aliasing is likely to occur. Aliasing occurs when a continuous-time signal with higher frequency is reconstructed as a lower-frequency signal from its samples. In weather radar applications, aliasing implies that the radial velocity measured by the radar is different from the true radial velocity by integer multiples of

$2v_a$, where v_a is the maximum unambiguous velocity, or aliasing velocity. The maximum unambiguous velocity can be derived from Equation (2.11) as follows:

$$\omega_{max} = \frac{4\pi}{\lambda} v_a \tag{2.13}$$

$$\omega_{max} = 2\pi f_{max} \tag{2.14}$$

$$f_{max} = \frac{f_s}{2} \tag{2.15}$$

$$\frac{4\pi}{\lambda} v_a = 2\pi \frac{f_s}{2} \tag{2.16}$$

$$v_a = \pm \frac{\lambda}{4T_s}. \tag{2.17}$$

Transmitting multiple pulses to sample the baseband signal enables the radar to measure the radial velocity of scatterers, but it also introduces the potential for range folding. Range folding occurs when the return signal from scatterers far away from a pulse does not reach the radar until after another pulse is transmitted, resulting in a measured time delay τ_s that is different from the true time delay by integer multiples of T_s. The maximum range the radar can measure without range ambiguity is referred to as the maximum unambiguous range, r_a, and is given by

$$r_a = \frac{cT_s}{2}. \tag{2.18}$$

From Equations (2.17) and (2.18), it is easy to see that a long PRT allows for a longer r_a but a smaller v_a and vice versa. This problem is known as the "Doppler dilemma". WSR-88D radars combine a long PRT to measure range

and a short PRT to measure radial velocities of weather phenomena wherever range folding or velocity aliasing are likely to occur.

After describing the basic operations of a radar and some of its basic components, the radar equation is introduced next to describe the basic relationship between the radar and a point target.

2.1.4 Radar Equation

Assume a radar transmits a pulse with peak power P_t and a target with backscattering cross section σ_b is located at range r with azimuth and elevation angles ϕ and θ, respectively. The received power is given by (Doviak and Zrnić 1993)

$$P_r = \frac{P_t g_t g_r \lambda^2 \sigma_b f_t^2(\theta,\phi) f_r^2(\theta,\phi)}{(4\pi)^3 r^4 l^2}, \tag{2.19}$$

where g_t and g_r are the directive gains of the transmit and receive antenna, f_t and f_r are the normalized beam patterns of the transmit and receive antenna, and l is the total loss. For a monostatic radar, usually $g_t = g_r$ and $f_t = f_r$. However, for a phased-array radar, it is possible to have different transmit and receive beam patterns that could result in different gains and beam patterns. Equation (2.19) is referred to as the radar equation, and it can be rearranged to calculate the minimum detectable signal or maximum detectable range for a particular radar and target. However, for weather radars that deal with distributed targets, the radar equation must be modified as explained next.

2.2 Radar Signal Processing

The key difference between weather radars and other types of radars that detect and track targets such as aircrafts is the target of interest. The target of interest for weather radars consists of large number of hydrometeors filling a volume much larger than the resolution volume. Each hydrometeor can be considered as a point target, and the backscattered signals from different drops add up coherently to form the received signal at the radar. It is impossible for a weather radar to detect and estimate the signal for each individual drop, and, as a result, the weather radar operates on the sum of the backscattered signals to provide a statistical estimate of the properties of the drops within a resolution volume. The properties of the drops are related to the received signal through the weather radar equation derived next.

2.2.1 Weather Radar Equation

Since the received signal is the sum of backscattered signals from scatterers in a resolution volume centered at range r_0, the weather radar equation can be written as (Doviak and Zrnić 1993)

$$\overline{P}(r_0) = \int_0^{r_2} \int_0^{\pi} \int_0^{2\pi} \eta(r) G(r_0, r) \mathrm{d}V \,, \tag{2.20}$$

where $\overline{P}$ is the expected received power, and η is the reflectivity or the backscattering cross section per unit volume. Reflectivity is defined as

$$\eta(r) = \int_0^\infty \sigma_b(D) N(D,r) \mathrm{d}D, \tag{2.21}$$

where $\sigma_b(D)$ is the expected backscattering cross section for a hydrometeor with diameter D, and $N(D,r)$ is the drop size distribution (DSD) that describes the number of drops expected for different diameters. G in Equation (2.20) is related to the characteristics of the radar and is given by

$$G(r_0,r) = \frac{C f_t^2(\theta_0-\theta,\phi_0-\phi) f_r^2(\theta_0-\theta,\phi_0-\phi)|W(r_0,r)|^2}{r^4 l^2}, \tag{2.22}$$

$$C = \frac{P_t g_t g_r \lambda^2}{(4\pi)^3} \tag{2.23}$$

where θ_0 and ϕ_0 represent the steering direction. The key difference between the weather radar equation and the point-target radar equation is that the received power is related to the reflectivity through a convolution with the beam pattern, and the received power decreases with r^2 rather than r^4, which is the result of the volume integral in Equation (2.20). Reflectivity is the variable of interest to meteorologist and the process to estimate reflectivity from received signal power is described next.

2.2.2 Calibration

From Equation (2.20), it is clear that the reflectivity and the received signal power are not linearly related. The process to estimate reflectivity from the

received signal power is referred to as weather radar calibration. Two key assumptions that allow the estimation of reflectivity from the received signal power are: 1) the product $\eta(\mathbf{r})f^4(\theta,\phi)$ is significantly larger only inside the resolution volume defined by the beam pattern and the range weighting function; in other words, it can be neglected outside the resolution volume, and 2) the reflectivity is constant within the resolution volume. If these assumptions are satisfied, then $\eta(\mathbf{r})$ can be factored out of the integral in Equation (2.20) resulting in the approximation

$$\overline{P}(r_0) \approx \frac{C\eta(r_0)}{r_0^2 l^2(r_0)} F \int_0^{r_2} |W(r)|^2 \, \mathrm{d}r \,, \tag{2.24}$$

where F is the integral of the two-way beam pattern given by

$$F = \int_0^{2\pi}\int_0^{\pi} f_t^2(\theta,\phi) f_r^2(\theta,\phi) \sin\theta \, \mathrm{d}\theta \, \mathrm{d}\phi \,. \tag{2.25}$$

Using this approximation, reflectivity and the received signal power become linearly related, and reflectivity can be estimated from the received signal power by applying a constant calibration factor. For a dish antenna, the beam pattern is designed such that it is significant only in the narrow main lobe, and as a result, the assumption of constant reflectivity within this small volume is more likely to be satisfied. The sidelobe levels of a dish antenna are designed to be at least -50 dB near the main lobe and drop to at least -80 dB farther away from the main lobe. With such low sidelobe levels, requirement (1) is also met in most cases. With proper calibration, the radar variables defined in the next sections can be estimated accurately.

2.2.3 Radar Variables and Estimators

After range- and sample-time sampling, the complex received signal is a discrete signal for each resolution volume, defined as

$$V(mT_s) = I(mT_s) + jQ(mT_s) \tag{2.26}$$

where m is the sample-time index. This discrete signal is also known as the "time series". The number of samples in each time series, usually denoted by M, combined with the PRT determines the time the radar spends observing each resolution volume, which is referred to as the dwell time, T_d. The dwell time is calculated as

$$T_d = MT_s\,. \tag{2.27}$$

For operational weather radars, the dwell time must not be too long in order to have a reasonable update time for the whole coverage space and must not be too short in order to estimate the spectral moments with the required precision. The dwell time also constrains the rotation rate of a mechanically steered antenna.

For each resolution volume, the time series can be used to estimate the Doppler spectrum, which is a power-weighted distribution of velocities that describes the motions of all the scatterers in the resolution volume. Mathematically, the Doppler spectrum is the discrete-time Fourier transform (DTFT) of

the autocorrelation function (ACF) of the time series. Assuming the underlying random process for the time series corresponding to a resolution volume is ergodic, the ACF can be estimated as

$$R(l) = \lim_{M\to\infty} \frac{1}{M} \sum_{m=0}^{M-|l|-1} V^*(m)V(m+l)\,, \tag{2.28}$$

where * is the complex conjugate operator, $V(m)$ is the mth sample of the time series, l is the time lag between samples for which the autocorrelation is being calculated, and T_s is dropped since it is understood that samples are taken T_s seconds apart (Doviak and Zrnić 1993).

The Doppler spectrum is then defined as

$$S(f) \equiv \lim_{M\to\infty} T_s \sum_{l=-(M-1)}^{M-1} R(l)\mathrm{e}^{-j2\pi f T_s l}\,. \tag{2.29}$$

Since each time series only has a finite number of samples due to the limited dwell time, robust estimators must be used to estimate the ACF and Doppler spectrum. The biased estimator of the ACF is

$$\hat{R}(l) = \begin{cases} \frac{1}{M}\sum_{m=0}^{M-|l|-1} V^*(m)V(m+l) & |l| \le M-1 \\ 0 & \text{otherwise} \end{cases}\,. \tag{2.30}$$

A common estimator of the Doppler spectrum is the periodogram, which is expressed as (Doviak and Zrnić 1993)

$$\hat{S}(f) = \frac{T_s}{M} \sum_{m=0}^{M-1}\sum_{n=0}^{M-1} V^*(m)V(n)\mathrm{e}^{-j2\pi f T_s(n-m)}\,. \tag{2.31}$$

In the case where reflectivity and shear fields are uniform, the shape of the Doppler spectrum follows the shape of the weighting function given by Equation (2.22) (Doviak and Zrnić 1993). Since the antenna pattern and the range weighting function for weather radars can be approximated by Gaussian functions in most cases, the Doppler spectrum will have a Gaussian shape as well. Moreover, the motion of each hydrometeor within the resolution volume is the sum of contributions from several different types of motion (i.e., uniform wind, shear, and turbulence), and each type of motion produces a Doppler spectrum associated with it. Since the overall Doppler spectrum is the convolution of these independent spectra, its shape will approach that of a Gaussian regardless of the shape of the individual spectra (Doviak and Zrnić 1993). Observed Doppler spectra confirms the Gaussian shape assumption under many conditions. However, non-Gaussian spectra with features such as dual peaks, wide flat tops, or a single Gaussian with strong tails have been observed and studied (Yu et al. 2009). Once the spectrum is assumed to have a Gaussian shape, three parameters can completely describe its shape: the signal power, the mean radial velocity, and the spectrum width. The signal power is the zeroth moment of the spectrum and is defined as

$$S \equiv \int_{-\infty}^{\infty} S(v)\,\mathrm{d}v\,, \tag{2.32}$$

where S is the signal power and $S(v)$ is the Doppler spectrum. The frequency dependence of the spectrum is converted to a velocity dependence, related by

Equation (2.11), for convenience of interpretation. The signal power can be converted to reflectivity, by adding a range correction and the radar calibration constant, determined using Equation (2.24). As shown in Equation (2.21), reflectivity is related to the backscattering cross section of the hydrometeors in the resolution volume. For spherical raindrops with diameters that are small compared to the wavelength (i.e. the Rayleigh approximation), the backscattering cross section can be approximated by

$$\sigma_b(D) \approx \frac{\pi^5}{\lambda^4} |K_w|^2 D^6 , \tag{2.33}$$

where K_w is the complex refractive index of water. Substituting Equation (2.33) into (2.21) to obtain

$$\eta = \frac{\pi^5}{\lambda^4} |K_w|^2 Z , \tag{2.34}$$

where Z is the reflectivity factor and is given by

$$Z = \int_0^\infty D^6 N(D,r) \mathrm{d}D . \tag{2.35}$$

In situations where the Rayleigh approximation does not apply, the reflectivity can be converted to an equivalent reflectivity factor (Z_e) by (Doviak and Zrnić 1993)

$$\eta = \frac{\pi^5}{\lambda^4} |K_w|^2 Z_e , \tag{2.36}$$

Since Z (Z_e) is directly related to the number, type and size distribution of the hydrometeors in the resolution volume, it can be used by automatic algorithms to generate products such as quantitative precipitation estimation.

The mean radial velocity is the first moment of the spectrum and is defined as

$$v_r \equiv \frac{1}{S}\int_{-\infty}^{\infty} vS(v)\,\mathrm{d}v\,, \tag{2.37}$$

where v_r describes the mean motion of the hydrometeors inside the resolution volume. The spectrum width, σ_v, is the second central moment of the spectrum and is defined as

$$\sigma_v^2 \equiv \frac{1}{S}\int_{-\infty}^{\infty} [v-\bar{v}_r]^2 S(v)\,\mathrm{d}v\,. \tag{2.38}$$

The spectrum width measures the shear and turbulence inside the resolution volume. The antenna rotation also contributes to increase the measured spectrum width for operational weather radars.

In practice, the integral definitions of the three moments cannot be used to calculate the spectral moments. Instead, time-domain and frequency-domain estimators are used to estimate the spectral moments. In the time domain, the signal power is estimated as

$$\hat{S} = \frac{1}{M}\sum_{m=0}^{M-1} |V(m)|^2\,. \tag{2.39}$$

The radial velocity can be estimated from the ACF. According to Doviak and Zrnić (1993), the ACF for a Gaussian spectrum is

$$R(lT_s) = S\exp[-8(\pi w l T_s/\lambda)^2]\mathrm{e}^{-j4\pi\bar{v}_r lT_s/\lambda} + N_o\delta_l\,, \tag{2.40}$$

where l is an integer index of the time-lag of the ACF function, N_o is the mean noise power, and δ_l is the Kronecker delta function that is equal to 1 when

$l = 0$ and 0 when $l \neq 0$. The mean radial velocity can be estimated using the phase of the ACF at lag T_s:

$$\hat{v}_r = -\frac{\lambda}{4\pi T_s} \arg \hat{R}_1 \,, \tag{2.41}$$

where

$$\hat{R}_1 = \frac{1}{M-1} \sum_{m=0}^{M-2} V^*(m) V(m+1) \,, \tag{2.42}$$

and the arg function returns the argument of a complex number. In Equation (2.41), the true ACF at lag T_s was replaced with an estimate $\hat{R}_1$, and $\hat{R}_1$ is calculated using Equation (2.42). Similarly, the spectrum width for a Gaussian spectrum can be estimated using the magnitude of the ACF. The spectrum width estimator using $\hat{S}$ and $\hat{R}_1$ is given by

$$\hat{\sigma}_v = \frac{\lambda}{2\pi T_s \sqrt{2}} \left| \ln \left(\frac{\hat{S}}{|\hat{R}_1|} \right) \right|^{1/2} . \tag{2.43}$$

The bias, variance, and limitations of the estimators given above along with the spectral processing estimators are discussed in detail in Doviak and Zrnić (1993). A Doppler spectrum for weather signals is shown in Figure 2.6. In this example, the red triangle is the estimated mean radial velocity and the horizontal bar centered on the estimated mean radial velocity indicates the estimated spectrum width.

Through recent upgrades, the WSR-88Ds have the capability to transmit both horizontal and vertical polarized waves simultaneously, this enables the

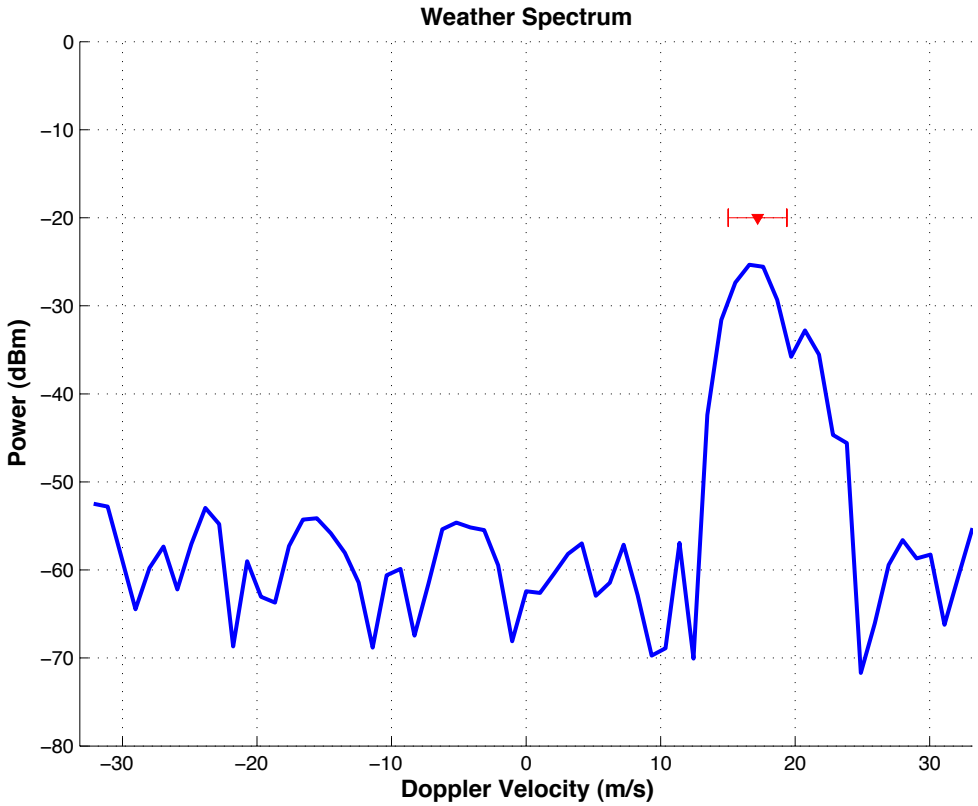

Figure 2.6: Typical Doppler spectrum for a resolution volume containing hydrometeors. The red triangle indicates the estimated mean radial velocity and the horizontal bar centered on the triangle indicates the estimated spectrum width.

estimation of three more polarimetric variables of interest: differential reflectivity, correlation coefficient, and differential phase. Differential reflectivity is the ratio of received powers in the horizontal and vertical polarizations, and it is estimated by (Doviak and Zrnić 1993)

$$\hat{Z}_{DR} = 10\log\left(\frac{\hat{S}_h}{\hat{S}_v}\right), \tag{2.44}$$

where $\hat{S}_h$ and $\hat{S}_v$ are the signal power, estimated using Equation (2.39) for the horizontal and vertical polarizations respectively. It is expected that drops with horizontally aligned major axis will produce positive Z_{DR} while drops with vertically aligned major axis will produce negative Z_{DR}. This ability to differentiate the shape of the drops can help to improve the accuracy of rainfall rate estimation and to detect the presence of hail (Kumjian 2013).

The correlation coefficient, ρ_{hv}, between the received voltages of the two polarizations is given by

$$\rho_{hv}(0) = \frac{E\left\{V_h V_v^*\right\}}{\sqrt{S_h S_v}}, \tag{2.45}$$

where V_h and V_v are the received signal voltages for the horizontal and vertical polarizations, respectively. The correlation coefficient is a measure of the diversity of the scatterers in the resolution volume, where a large variety in the types, shapes, and orientations of the scatterers leads to decreased correlation coefficient. The presence of non-meteorological scatterers can also lead to a low ρ_{hv} (< 0.8) (Kumjian 2013).

The specific differential phase (K_{DP}) is the range derivative of the differential phase (Φ_{DP}), which is given by

$$\Phi_{DP} = \arg E\left\{V_h^* V_v\right\} . \tag{2.46}$$

Φ_{DP} is the difference in phase shift as the horizontal and vertical polarized waves propagate through scatterers, and it is not affected by attenuation, which makes it an attractive option for attenuation correction (Kumjian 2013). K_{DP} can be used to detect regions of heavy rain, and can be used with Z_h to improve rainfall estimations. Since the goal of this work is to analyze the first-order trade-offs of applying adaptive beamspace algorithm to weather radar, the spectral moments will be used as the radar variables to track the performance of the algorithm for simplicity. For estimating the polarimetric variables, the same adaptive algorithm can be applied to received signals from the horizontal and vertical polarizations independently to generate the received voltage signals, and the estimators described in this section can be applied. Analyzing the impacts of potentially having different adaptive weights for the different polarizations on the estimation of the polarimetric variables is left as future work.

2.2.4 Clutter Filtering

A significant source of error in estimating the radar variables is the presence of returns from non-meteorological targets, commonly referred to as clutter.

Common sources of clutter are insects, birds, trees, buildings, aircraft, or wind turbines. Unwanted clutter signals cause biases to the spectral moment estimates, and therefore must be removed to ensure the quality of the radar products. The most common occurring clutter is from ground returns or ground clutter. In a resolution volume where hydrometeors and ground clutter are both present, the spectral moment estimates are significantly biased by the ground clutter as shown in Figure 2.7 (blue line). Ground clutter can be easily recognized in the Doppler spectrum because it has zero radial velocity and a narrow spectrum width. Time domain regression filters (Torres and Zrnić 1999) and spectral domain methods, such as Gaussian Model Adaptive Processing (GMAP) (Siggia and Passarelli 2004) and Clutter Environment Analysis using Adaptive Processing (CLEAN-AP) (Warde and Torres 2009), are all possible solutions to mitigate the biases in spectral estimates caused by ground clutter. The result after passing the spectrum through a ground clutter filter (GCF) is shown in Figure 2.7 (red dashed line). The spectral estimates for the weather only, ground clutter contaminated, and ground clutter filtered spectra are listed in Table 2.2. In the example shown, the ground clutter filter reduced the power bias from 12.30 dB to 0.0056 dB, the velocity bias from -15.99 $\mathrm{m\,s^{-1}}$ to -0.022 $\mathrm{m\,s^{-1}}$, and the spectrum width bias from 1.51 $\mathrm{m\,s^{-1}}$ to 0.069 $\mathrm{m\,s^{-1}}$. GCF are effective at mitigating contaminations due to stationary targets, but they have limited effectiveness at mitigating contamination

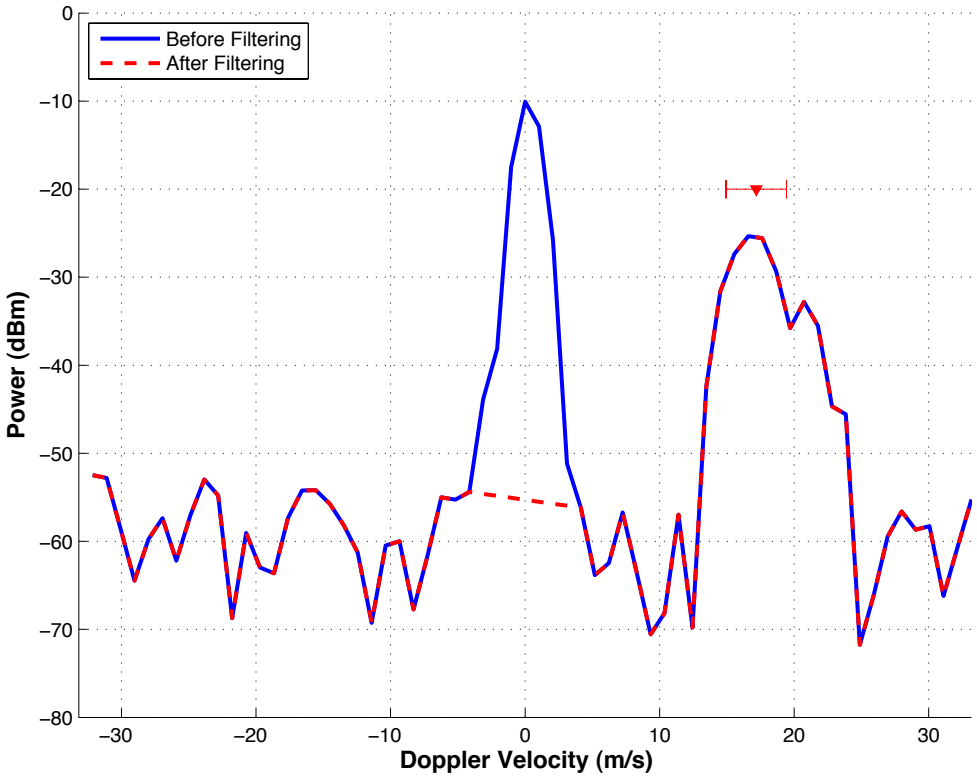

Figure 2.7: Typical Doppler spectrum for a resolution volume containing hydrometeors and ground clutter (blue line). The ground clutter filter removed the majority of the clutter power located near 0 m s^{-1}(red dashed line). The spectral moment estimates after filtering are closer to the estimates shown in Figure 2.6.

Table 2.2: Comparison of the spectral estimates before and after ground clutter filtering for ground clutter contamination.

	Power (dBm)	**Radial Velocity (m s^{-1})**	**Spectrum Width (m s^{-1})**
Weather Only	-19.719	17.207	2.174
Before Filtering	-7.415	1.220	3.684
After Filtering	-19.714	17.185	2.243

from non-stationary clutter, such as wind turbine clutter (WTC). The change of WTC spectrum with respect to time is shown in Figure 2.8, where the x-axis is Doppler velocity, the y-axis is time, and the color represents the power in dB in each frequency bin (Isom et al. 2009). In Figure 2.8, there are three compo-

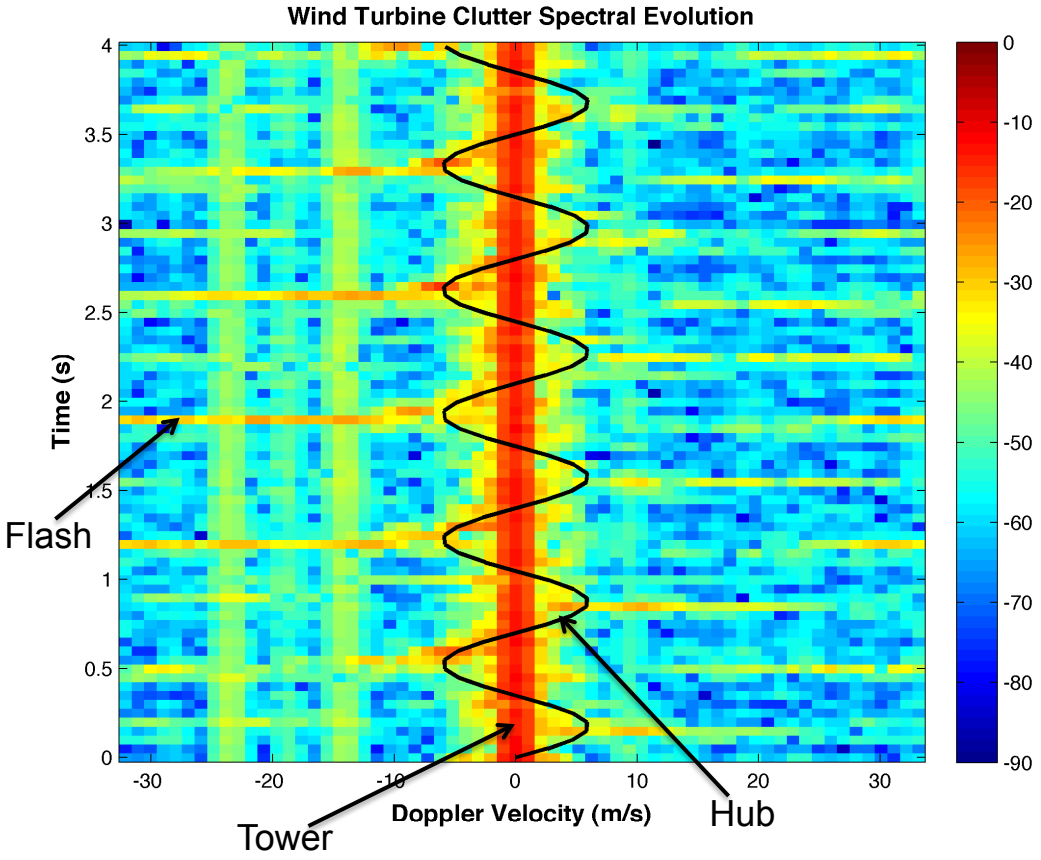

Figure 2.8: Spectral evolution of the WTC signal. Each row is a Doppler spectrum for a 64-sample time-series from a resolution volume containing a wind turbine. The three components of WTC signal are the tower, hub, and flash as indicated on the figure extracted from Isom et al. (2009).

nents in the WTC spectral evolution: the stationary ground clutter, the slowly oscillating hub, and the flash. Figure 2.9 shows the result after applying a

GCF to an example flash contamination. The estimated spectral moments are compared in Table 2.3, where it is clear that a conventional GCF is ineffective at mitigating WTC contamination.

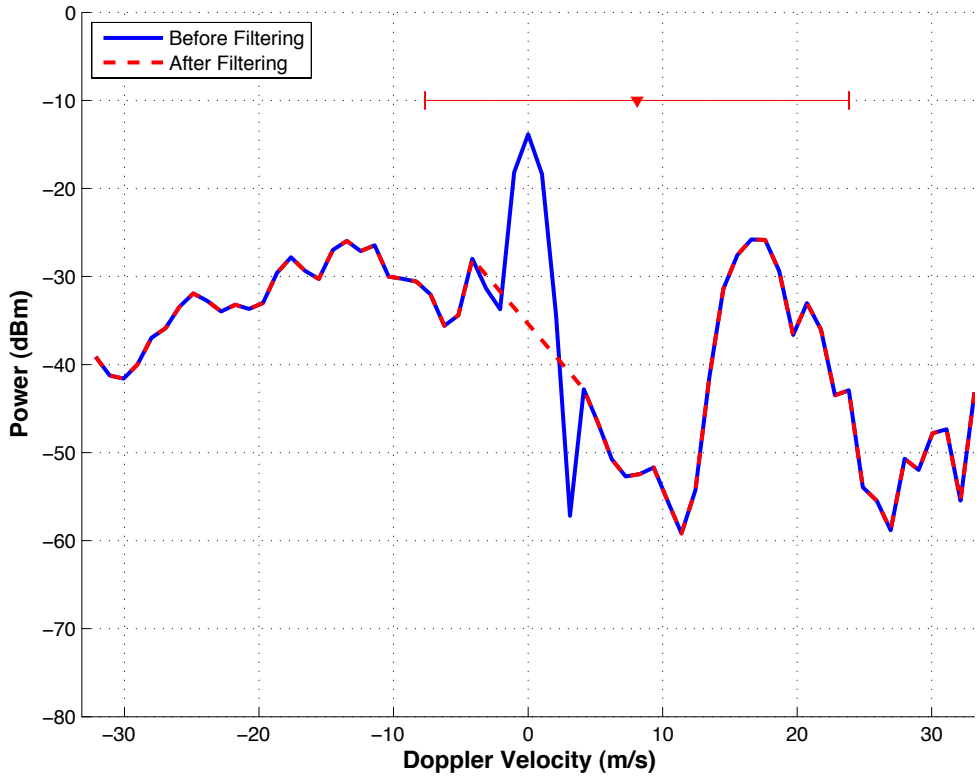

Figure 2.9: Dopper spectrum of a flash contamination. The GCF removed the tower signal but is ineffective at removing the flash contamination. The flash contamination away from zero Doppler is mostly unaffected by the filter and the spectral moment biases remain large.

Table 2.3: Comparison of the spectral moment estimates before and after ground clutter filtering for WTC contamination.

	Power (dBm)	**Radial Velocity ($\mathrm{m\,s^{-1}}$)**	**Spectrum Width ($\mathrm{m\,s^{-1}}$)**
Weather Only	-19.719	17.201	2.174
Flash; Before Filtering	-9.740	-1.603	8.501
Flash; After Filtering	-14.372	8.110	15.759

An algorithm using range-Doppler spectra to mitigate WTC contamination was proposed in Nai et al. (2013b). However, with wind turbines being discretely located in space, it is possible to utilize spatial filtering instead of time/frequency filtering to mitigate WTC contamination. Advantages spatial filtering compared to the method proposed in Nai et al. (2013b) are that spatial filtering can be applied on a gate by gate basis and it does not require *a priori* knowledge of the locations of the wind turbines.

2.3 Scanning Strategies

Weather radars not only must produce accurate estimates of the radar variables discussed in the previous section, they must also provide updated information at a reasonable rate. Some rapidly evolving phenomena such as tornado genesis and microbursts can be missed by the radar if the update time is too long. The current update time and scanning strategies of the WSR-88D and the desired update time for the next generation of weather radars are discussed next.

2.3.1 Current VCP and Update Time

The current volume coverage patterns (VCP) used by WSR-88D are described in the Federal Meteorological Handbook No. 11 Part C (FMH Apr. 2006). When the radar is operating in precipitation mode, it can achieve an update time between four minutes (VCP 12) to five minutes (VCP 11) when observing

convective storms. For example, VCP 12 scans the lowest elevations (0.5° and 1.5°) using the split cut scan, which consists of two scans with different PRTs to obtain reflectivity and spectrum width (first scan) and mean radial velocity and polarimetric variables estimates (second scan). The middle elevations (2.4° to 6.2°) are scanned in batch mode where a group of long PRT pulses are followed by a group of short PRT pulses. The higher elevations (7.5° to 19.5°) are scanned once with short PRTs. Recently, the SAILS has been proposed to improve the update time for the lowest elevations of a volume scan (ROC 2013). However, providing faster updates only for the lowest elevation is not a satisfactory solution because there are phenomena that develop in the upper atmosphere that could be missed by SAILS. Also, by inserting additional scans for the lowest elevations, the update time for the entire volume is increased in some cases.

2.3.2 Desired Update time

It is understood that high-temporal-resolution observations can lead to improved understanding and warning of hazardous weather phenomena (Miller and Kropfli 1980; Carbone et al. 1985). A survey of National Weather Service forecasters and television weather forecasters showed that the current update time of four to five minutes for the WSR-88D could miss significant storm evolution and transition. Tornadic storms, squall lines, and downbursts were

pointed out as especially problematic due to the temporal resolution of the WSR-88D (LaDue et al. 2010). Improving update times for lower-level coverage as discussed in the previous section could mitigate some of the concerns, but the best solution is to improve the volumetric update time to the order of one minute. The PARISE experiments in 2010 and 2012 showed that high-temporal-resolution data resulted in increased tornado warning lead times for weak tornados, severe hail, and wind events, and increased confidence levels of the warnings (Heinselman et al. 2012, 2015; Bowden et al. 2015; Bowden and Heinselman 2016).

With a dish antenna, the inertia of mechanical rotation severely limits the possible scanning strategies. The dish antenna cannot be stopped and arbitrarily directed to scan directions of most interest without damaging the radar. However, for phased-array radars, it is much easier to execute adaptive scanning strategies due to its electronic steering capabilities (Zrnić et al. 2007). The NWRT PAR can achieve 60-second volumetric update times by utilizing the electronic steering ability and adaptive scanning strategies (Heinselman et al. 2008; Heinselman and Torres 2011; Torres et al. 2016). Despite the excellent performance shown by the NWRT PAR, phased-array radars also pose significant challenges as weather radars, especially in a multifunctional setting. Next chapter will discuss the concept of phased-array radar in detail and explain the challenges of using a phased-array radar to observe weather.

Chapter 3

Phased-Array Radars

A major difference between a phased-array radar and a conventional radar is the type of antenna used. Conventional radar usually uses a single antenna to radiate power into space and to receive backscattered signals. The radiation pattern is determined by the size of the antenna and the excitation distribution on the the aperture of the antenna (Skolnik 2001). A phased-array radar, on the other hand, uses discrete radiating elements to emulate a continuous distribution. This chapter will introduce the different architectures of phased-array radar and discuss the advantages and disadvantages of each type. Further, several methods of nonadaptive and adaptive beamforming will be discussed. Finally the challenges of a multifunction phased-array radar (MPAR) will be described.

3.1 Introduction to Phased-Array Radar

Traditional weather radars, such as the WSR-88D, use a parabolic reflector antenna to transmit a pencil beam with a fixed radiation pattern. In contrast, phased-array radars use discrete radiating elements to emulate the continuous

excitation produced by a parabolic reflector antenna. Each radiating element is excited by signals that have a carefully determined amplitude and phase (also referred to as a complex weight) such that the sum of radiations from all the radiating elements produces a desired radiation pattern. Being able to adjust the complex weight for each radiating element, a phased-array radar has significant more control over the final radiation pattern. For example, nulls in the radiation pattern can be produced and steered to the desired direction so that backscattered signals from those directions are severely attenuated. Another strength of a phased-array radar is electronic steering. Since the radiation pattern is determined by the complex weights, which can be modified quickly, the radiation pattern of the radar can be steered to different directions for successive transmit pulses to reduce the scanning time (Zrnić et al. 2015). Unlike a traditional dish-antenna radar where the scanning must be done in a continuous manner due to the mechanical inertia of the antenna, a phased-array radar can switch between beams pointed at significantly different directions quickly and efficiently. Beam smearing due to rotation of the antenna is also absent in a phased-array radar. Furthermore, phased-array radar also potentially allows for different waveforms being used on different radiating elements, which can help the radar to achieve multiple functions simultaneously. However, for planar arrays, as the beam is steered off broadside, the beam widens. This beam

broadening effect must be taken into consideration during the design a phased-array system and in the signal processor.

Currently, the United States operates multiple radar networks that perform terminal and long-range aircraft and weather surveillance. As these radars get near their lifetime, a new radar network composed of MPARs is being proposed to replace the aging networks (Weber et al. 2007; Zrnić et al. 2007; Weadon et al. 2009). By replacing multiple networks with a single network, the number of radars required would be reduced by more than 30%, which can significantly reduce the operation and maintenance cost over the lifetime of the network. Figure 3.1 is a conceptual illustration of an MPAR that can track aircraft (coorperating and non-coorperating) and multiple severe storms. With electronic steering, an MPAR can also focus on regions of space of significant interest, such as severe storms. Discussions in Chapter 2 have shown that fast update times can lead to increased warning lead times and warning confidence for hazardous weather, and phased-array radars are uniquely positioned to achieve that desired update time. Research done using the NWRT PAR has demonstrated that phased-array weather radars can achieve faster update times while maintaining data quality (Curtis and Torres 2011; Yu et al. 2007; Reinoso-Rondinel et al. 2010).

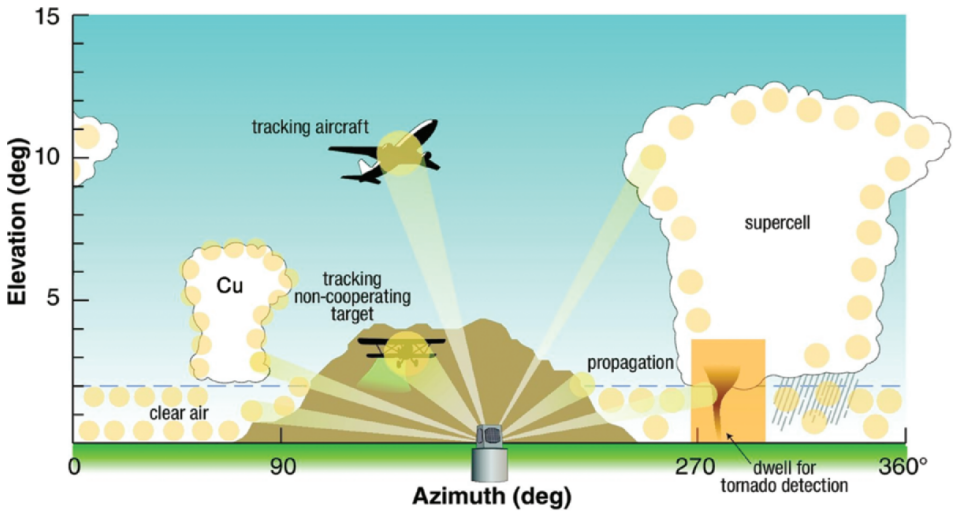

Figure 3.1: Conceptual illustration of MPAR from Zrnić et al. (2007). The radar can track aircraft and perform weather surveillance with acceptable update time for both missions. With electronic steering capability, the radar can focus on regions of interest (e.g., a tornado) to provide faster updates.

Phased-array radars can significantly improve the update time for weather surveillance, but they also introduce some challenges. One significant challenge is the accurate estimation of polarimetric variables. For a planar array, the horizontal and vertical polarizations are not always orthogonal when the beam is steered off broadside, and the biases must be corrected for the polarimetric variables to be useful (Zhang et al. 2009). Another possibility to improve the polarimetric estimates is to use a cylindrical array instead of planar arrays (Zhang et al. 2011). Moreover, in a simultaneous transmit and receive operation mode, the phased-array antenna must provide sufficient cross-polar isolation to minimize the cross-polarization contamination to the co-polar measurements. Any mismatch between the beam patterns of the two polarizations

can also lead to large biases in the estimates of the polarimetric variables. The polarimetric issues are important, but since this work is proposing a new adaptive beamspace algorithm for phased-array weather radars, the main focus should be on the fundamental trade-offs, which can be tackled in a simpler manner using the spectral moments. Only if these initial results are promising, should the analysis of the impact of adaptive beamforming on estimation of polarimetric variables be done. The rest of this chapter will discuss the different architectures of phased-array radar, and introduce the different beamforming methods.

3.2 Archetypes of Phased-Array Radar

The development of phased-array radars started after World War II and continues through the present day (Skolnik 2001). Due to the limitations of the electronic components and computing power, the earliest phased-array systems relied on analog beamformers to generate the desired beams. As technologies advanced, a new architecture based on subarrays was developed to allow more control over the beam pattern. The future of phased-array radars is an all-digital architecture, in which each radiating element has its own transmit/receive (T/R) module and digital synthesizer (DDS) that controls the amplitude, phase, and waveform of the transmitted signal (Fulton et al. 2016). Further, by digitizing the received signal from each receiving element, any

beamforming algorithm can be used to extract the useful information. These basic architectures will be discussed in detail next.

3.2.1 Passive Arrays

The earliest phased-array systems are passive arrays. A passive array uses a feed network to split the transmit signal from a single high-power source to provide the transmit signal for each radiating element (Skolnik 2001). As shown in Figure 3.2, each radiating element has a phase-shifter and an attenuator to adjust the phase and amplitude of its transmitted signal, but there are no active components. During receive, the feed network also sums all received signals from the radiating elements into a single output that can be digitized and processed. The feed network, phase-shifters, and attenuators combined are referred to as an analog beamformer. By adjusting the phase-shifters, the radar can electronically steer the beam, but the flexibility to adaptively form beams is lost since the received signals at the element level are combined into the final output. Another disadvantage of passive arrays is that the components in the analog beamformer usually have associated losses, and to overcome these losses, a higher transmit power is needed (Skolnik 2001). However, compared to active array architectures, passive arrays usually have lower cost since they require fewer components and processing power. An example passive array is the NWRT PAR (Zrnić et al. 2007).

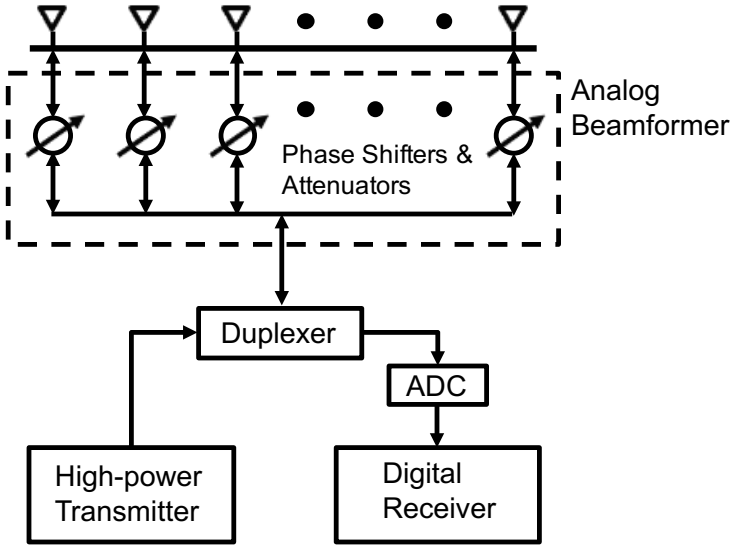

Figure 3.2: Illustration of a passive array system with an analog beamformer, adapted from Skolnik (2001). A single transmitter drives the array, and high-power phase shifters at each radiating element are used to steer the beams. The analog system has fewer components compared to an active-aperture system and is likely to have a lower cost.

3.2.2 Digitized Subarrays

To alleviate some of the limitations of passive arrays, architectures utilizing subarrays were developed. In a subarray architecture, such as the example shown in Figure 3.3, many radiating elements are grouped together to form a subarray, and each subarray has its own analog beamformer to provide the transmit and to produce the receive signal. In some cases, the subarrays can also have overlapping elements to reduce the distance between the phase centers of the subarrays, which can spread out the grating lobes to reduce their impacts on the radar performance. Each subarray has its own transmit waveform generated by the DDS, and its output is digitized and fed into a digital

signal processor. The transceivers (Xcvr) are responsible for upconverting and downconverting the transmit and receive signals. By having received signals from different subarrays, adaptive beamforming is possible. Also, by relying on multiple T/R modules to generate power, the array is less susceptible to catastrophic failures compared to a passive array. However, this architecture requires more components and is likely to be more expensive compared to the passive array.

3.2.3 All-Digital Arrays

The most flexible architecture is the all-digital array. In this architecture, shown in Figure 3.4, each radiating element has a T/R module, a transceiver, a DDS, and an analog-to-digital converter. With this set up, each radiating element can operate as an individual radar with its own waveform, amplitude-and-phase control, and digitized received signal. Since the transmit signal for each element is synthesized locally, phase shifter and attenuator are not needed. Having the received signals from all radiating elements provides the greatest degrees of freedom for adaptively modifying the beam pattern to reject clutter and interference signals. The all-digital architecture also enjoys graceful degradation in performance when components malfunction since it is not critically dependent on any single radiating element. However, the heat generated by the extra components must be dissipated carefully since some

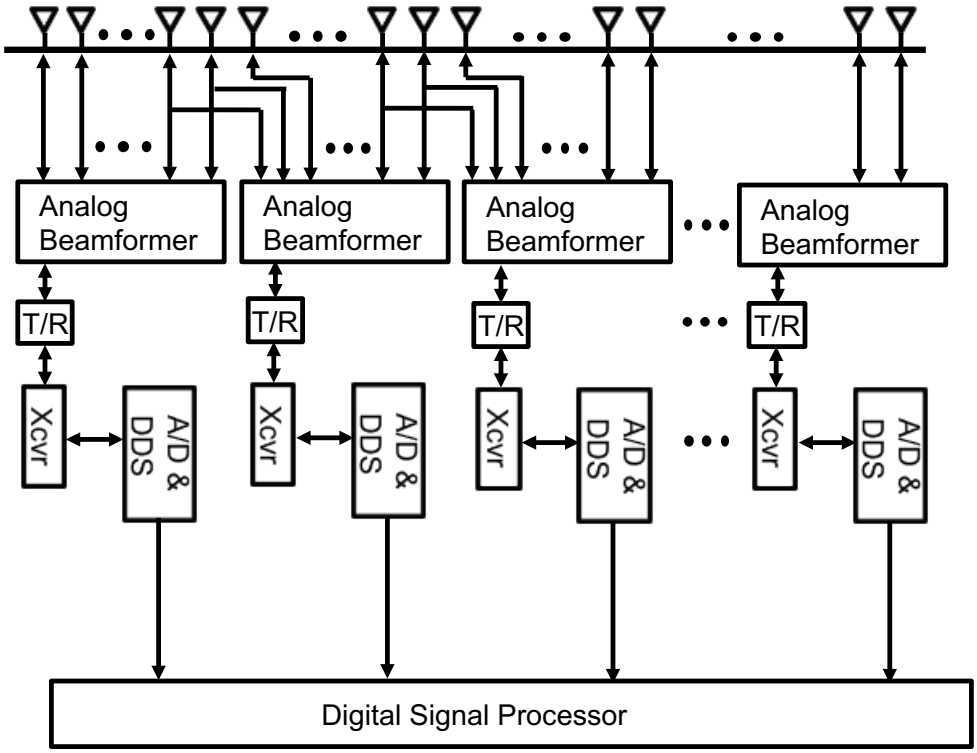

Figure 3.3: Illustration of subarray-based active-aperture phased-array system, adapted from Fulton et al. (2016). Radiating elements are grouped into subarrays that utilize an analog beamformer to steer the elements within the subarray. Each subarray has its own T/R module, transceiver, digital synthesizer, and analog-to-digital converter. By processing received data from multiple subarrays, adaptive beamforming can be performed albeit with a limited number of degrees of freedom.

of the components have temperature dependencies, and the processing power must keep up with the increased data rate. The higher level of power consumption of an all-digital system is a disadvantage compared to other architectures. For the rest of this dissertation, in order to enjoy the full flexibility offered by a phased-array radar, an all-digital system is assumed.

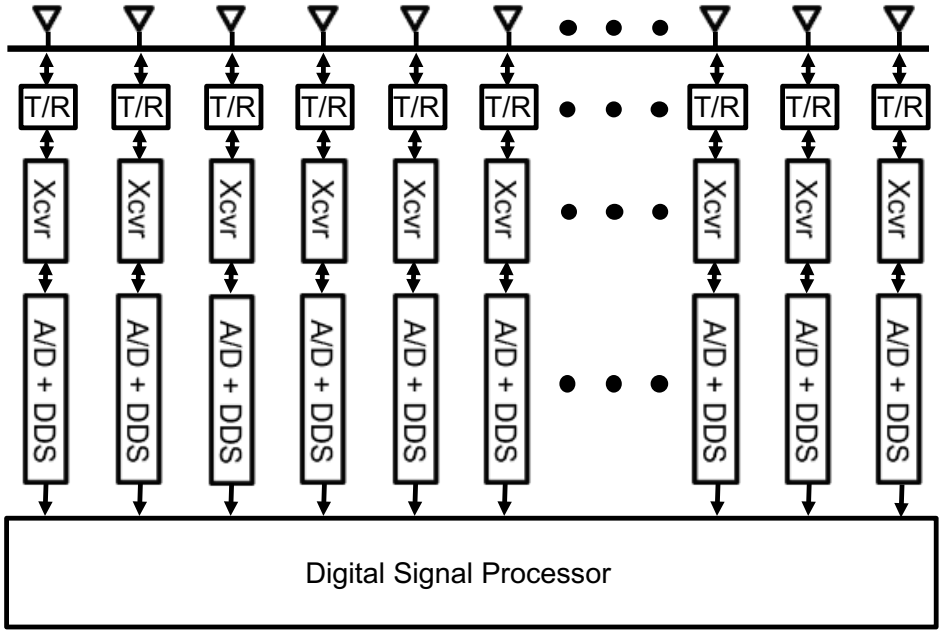

Figure 3.4: Illustration of an all-digital active-aperture phased-array system, adapted from Fulton et al. (2016). Each radiating element has its own T/R module, transceiver, digital synthesizer, and analog-to-digital converter (A/D). This type of system has maximum flexibility for on-the-fly adaptive beamforming that matches the mission of the radar. However, the all-digital architecture consumes more power compared to other architypes.

3.3 Digital Beamforming

As shown in Figure 3.4, for an all-digital architecture, after the received signals are digitized, they are fed into a digital signal processor that utilizes digital

beamforming to generate the final outputs. Without loss of generality, a linear array with N identical and isotropic radiating elements that are uniformly spaced is used in the rest of the chapter to explain the beamforming methods. The separation between adjacent elements is assumed to be d. The received signals are put into a vector $\mathbf{x}$ where the nth element of $\mathbf{x}$ corresponds to the received signal from the nth radiating element. The general equation describing digital beamforming is

$$y(t) = \mathbf{w}^H \mathbf{x}(t)\,, \tag{3.1}$$

where $y(t)$ is the output of the beamformer and $\mathbf{w}$ is the complex weight vector that determines the pattern of the receive beam. Different beamforming methods can be used to determine $\mathbf{w}$, and some common methods are described next.

3.3.1 Nonadaptive Beamforming

Nonadaptive beamforming methods determine the complex weights based on the geometry of the array and other criteria independent of the received signal, as shown in the flowchart in Figure 3.5. By being independent from the received data, the computational complexity for nonadaptive methods is usually less than that of adaptive methods, and the weights can be calculated off-line and stored to further reduce processing time.

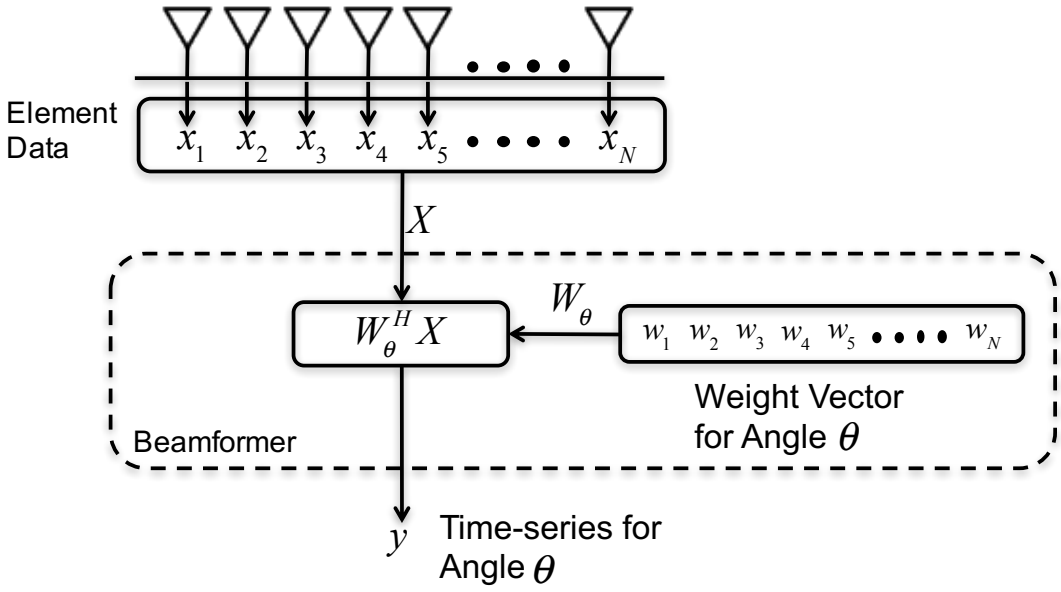

Figure 3.5: Flow chart showing a general nonadaptive beamforming process. The received signals are weighted and summed to form the final output. The weight vector is independent of the received data. The beam pattern can be adjusted to match a known desired pattern, and nulls can be placed in certain fixed directions to attenuate interference and clutter.

The standard nonadaptive beamforming method is Fourier beamforming, which determines **w** based on the geometry of the array. Figure 3.6 is an illustration of a plane wave (black lines) arriving at the array from angle θ (measured from broadside of the array). Without loss of generality, the plane wave is assumed to have unit amplitude, and the equation describing the received signal for the first element is

$$s(t) = e^{j2\pi f_o t}. \tag{3.2}$$

where f_o is the carrier frequency of the plane wave. The peak of the wave (at $t = 0$) arriving at the first element is indicated by the green dashed lines. Since the separation between adjacent elements is d, that same peak will arrive at the nth element after traveling an extra distance of $(n-1)d\sin(\theta)$, and the equation for the received signal at the nth element is

$$\begin{aligned} s_n(t) &= e^{j2\pi f_o\left[t-\frac{(n-1)d\sin(\theta)}{c}\right]} && (3.3)\\ &= e^{j2\pi f_o t - j\frac{2\pi}{\lambda}(n-1)d\sin(\theta)}. && (3.4) \end{aligned}$$

If the received signal of the first element is defined as the reference signal, the received signal for the entire array can be written as

$$\mathbf{x}(t) = \begin{bmatrix} x_1 & x_2 & \cdots & x_N \end{bmatrix}^T, \tag{3.5}$$

$$\mathbf{x}(t) = \mathbf{a}(\theta)s(t), \tag{3.6}$$

where x_n is the received signal at the nth element, and $\mathbf{a}(\theta)$ is referred to as the steering vector and is given by

$$\mathbf{a}(\theta) = \begin{bmatrix} 1 & e^{-j\frac{2\pi}{\lambda}d\sin\theta} & \dots & e^{-j\frac{2\pi}{\lambda}(N-1)d\sin\theta} \end{bmatrix}^T . \tag{3.7}$$

The superscript T denotes the matrix transpose operation. The elements of $\mathbf{a}(\theta)$ describe the expected phase of the received signal arriving from angle θ due to the genometry of the array. The basic function of beamforming is to compensate for these phase differences so that when the received signals are summed, the signal arriving from a direction of interest is summed in-phase while signals from other directions are summed out-of-phase.

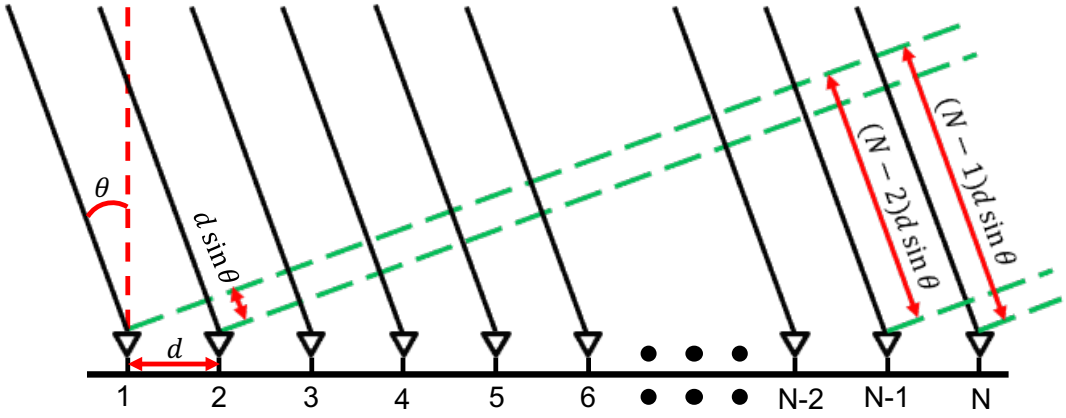

Figure 3.6: Illustration of a linear array receiving signals from direction θ. When the received signals are sampled at a fixed time, there is a inherent phase difference between the received signals at different elements due to the different distances traveled by the wave. By compensating for these phase differences, a beam can be formed to point in any desired direction.

The weight for Fourier beamforming is

$$\mathbf{w}(\theta) = \frac{1}{N}\mathbf{a}(\theta) . \tag{3.8}$$

Substituting (3.6) and (3.8) into (3.1) gives

$$\begin{aligned} y(t) &= \mathbf{w}^H \mathbf{x} \\ &= \frac{1}{N}\mathbf{a}^H(\theta)\mathbf{a}(\theta)s(t) \\ &= s(t)\,, \end{aligned} \tag{3.9}$$

where $\mathbf{a}^H(\theta)\mathbf{a}(\theta) = N$ by design. Equation (3.9) shows that the output of the Fourier beamformer is equal to the signal arriving at the array, as expected. It can also be shown that Fourier beamforming has the minimum white-noise gain (Stoica and Moses 2005), but it is unsatisfactory for weather surveillance due to its high sidelobe levels that could produce significantly biased estimates in situations where the hydrometeors are nonuniformly distributed in space. A commonly used technique to reduce the sidelobe levels is amplitude tapering. An example of tapering is shown in Figure 3.7, where the top panel shows the amplitude of the weights with (red line) and without taper (blue line) and the bottom panel shows the resulting beam patterns. It is clear that tapering can significantly reduce the sidelobe levels, but the 3-dB beamwidth is increased. Furthermore, the amplitude of the received signals from elements located at the edge of the array are reduced by the taper, which would lead to a loss of sensitivity of the radar. Many different types of taper and their properties are described in Harris (1978) and Nuttall (1981). The effectiveness of tapering on reducing the biases in signal power estimates is shown in Figure 3.8. In this example, the signal power (blue line) has a uniform distribution of and

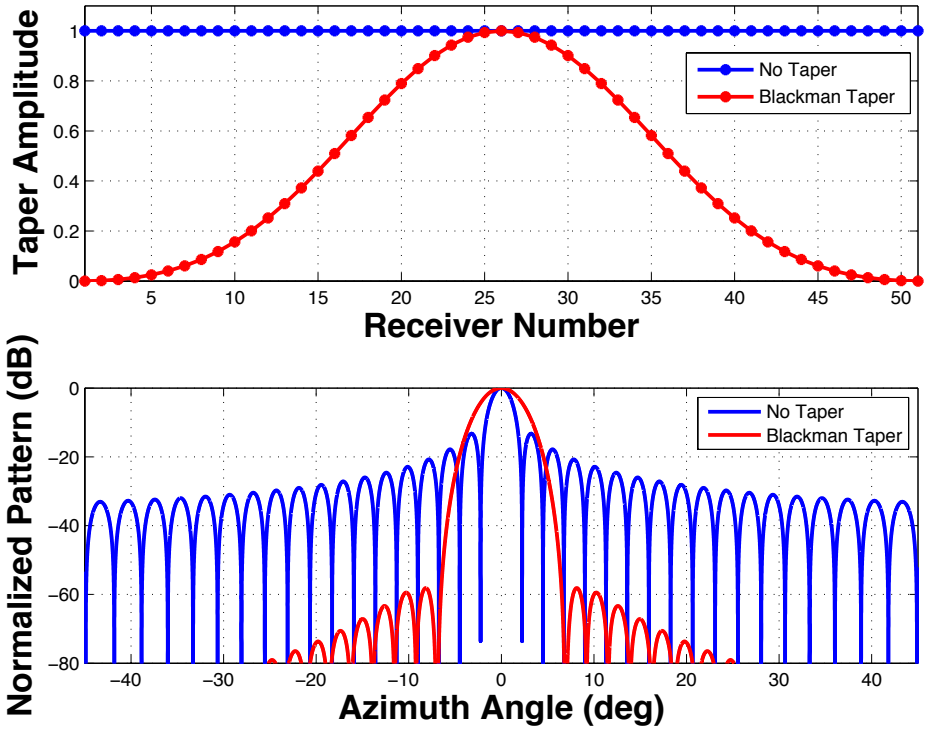

Figure 3.7: Example beam patterns with (red line) and without (blue line) amplitude taper. In this example, Blackman tapering increases the 3-dB beamwidth but lowers sidelobe levels. Moreover, tapering attenuates the received signals from the elements located at the edge of the array, resulting in a loss of sensitivity for the radar.

a strong interference signal is located at 0°. The signal power estimates of Fourier beamforming with (green line) and without (red line) amplitude taper are plotted, and the leakage of signal power from the high sidelobes in the no-taper case can be clearly seen. Only by applying a taper, the signal power estimates approach the simulated signal power for the majority of azimuth angles except for angles near 0°.

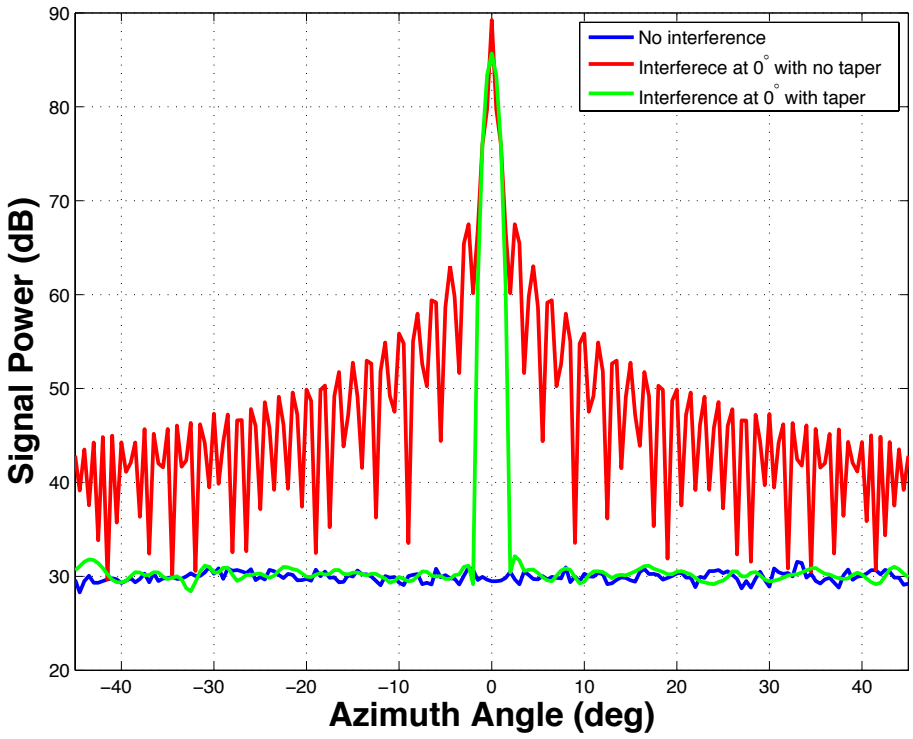

Figure 3.8: Signal power estimates with (green line) and without (red line) tapering. Without tapering, the strong interference signal located at 0° causes significant biases in estimates of signal power at other angles. By using a taper, the leakage of power to other angles is significantly reduced, and the estimates are in agreement with the true signal power for those angles (blue line).

Another approach to nonadaptive beamforming is referred to as pattern synthesis where the weights are determined by minimizing the difference between the actual pattern and a desired beam pattern. Let $H_d(\theta)$ be a desired beam pattern, the squared error, ε, between the desired pattern and a beam pattern generated by $\mathbf{w}$ is

$$\varepsilon = \int_{-\pi}^{\pi} \left| H_d(\theta) - \mathbf{w}^H \mathbf{a}(\theta) \right|^2 \mathrm{d}\theta \,. \tag{3.10}$$

Expanding the integrand in Equation (3.10) and setting the derivative to 0 provides a solution of $\mathbf{w}$ given by (Van Trees 2002)

$$\mathbf{w} = \mathbf{A}^{-1} \int_{-\pi}^{\pi} \mathbf{a}(\theta) H_d^* \theta \, \mathrm{d}\theta \,, \tag{3.11}$$

$$\mathbf{A} = \int_{-\pi}^{\pi} \mathbf{a}(\theta) \mathbf{a}^H(\theta) \, \mathrm{d}\theta \,, \tag{3.12}$$

where $\mathbf{A}$ is an N-by-N matrix. Since pattern synthesis minimizes the total error between the patterns, there is no constraint on the gain of the beam at any particular direction. If the desired pattern has discontinuities, then the synthesized pattern can have oscillatory overshoots at these discontinuities, which is known as Gibbs phenomenon (Van Trees 2002). A taper can be applied to the synthesized weight vector to alleviate the oscillation problem, but the price is a wider beam.

If *a priori* information about the environment is available, it can be used to place constraints on the beam pattern as well. One example of such an approach is called null steering, where nulls in the pattern can be placed in

directions of known interference or clutter signals. The mathematical formulation for null steering is

$$\min \|\mathbf{w}_d - \mathbf{w}\|^2 \quad \text{subject to} \quad \mathbf{C}^H \mathbf{w} = 0\,, \tag{3.13}$$

where $\mathbf{w}_d$ is the weight vector that generates a desired beam pattern without nulls, and $\mathbf{C}$ is the constraint matrix that describes which directions the nulls should be placed at. If nulls are desired at $\theta_1, \theta_2, \cdots, \theta_L$, the constraint matrix is given by

$$\mathbf{C} = \begin{bmatrix} \mathbf{a}(\theta_1) & \mathbf{a}(\theta_2) & \cdots & \mathbf{a}(\theta_L) \end{bmatrix}, \tag{3.14}$$

where the ith column of $\mathbf{C}$ is the steering vector for angle θ_i. More advanced constraint matrices can be constructed to force the first derivative or the second derivative of the beam pattern at a specific angle to be zero. These types of constraints can be used to broaden the null (Van Trees 2002). Care must be used to select the columns of $\mathbf{C}$ to ensure that they are independent so that the optimization problem in Equation (3.13) can be solved. If the columns of $\mathbf{C}$ are independent, then the solution is given by

$$\mathbf{w}^H = \mathbf{w}_d^H - \left(\mathbf{w}_d^H \mathbf{C} \left[\mathbf{C}^H \mathbf{C} \right]^{-1} \mathbf{C}^H \right). \tag{3.15}$$

The optimum weight vector can be interpreted as the desired weight vector after subtracting a weighted sum of the constraint vectors in $\mathbf{C}$. Null steering is useful in scenarios where the directions of interference or clutter signals are known and stable. Examples of such signals would include returns from

radio towers, water towers, tall buildings, and other fixed structures. To handle interference sources that move in space, such as backscattered signals from an aircraft when performing weather surveillance, adaptive methods that depend on the received data must be used.

3.3.2 Adaptive Beamforming

The key idea of adaptive beamforming is to use the received data to derive information about the environment that can be used to adjust the beam pattern to minimize the impact of undesired signals. A possible example is when the radar is performing weather surveillance and the main beam is steered to scan a storm while an aircraft is flying at a different direction, as shown in Figure 3.9. Since the aircraft has a large backscattering cross-section, its backscattered signal in a direction of a sidelobe can contaminate the backscattered signal from the main beam. Since the aircraft is moving, the direction of this interference signal is not known or fixed, and nonadaptive beamforming described in the previous section cannot be used to null out this signal unless the sidelobes are significantly reduced everywhere. Such an approach usually would need an aggressive taper and would suffer from having a much wider beamwidth and significant loss in sensitivity. With adaptive beamforming, it is possible to use the received data to automatically determine the direction of interference signals and adjust the beam pattern to reduce their impacts. In the

example shown in Figure 3.9, adaptive beamforming can place a null in the direction of the aircraft, which will minimize out its backscattered signal.

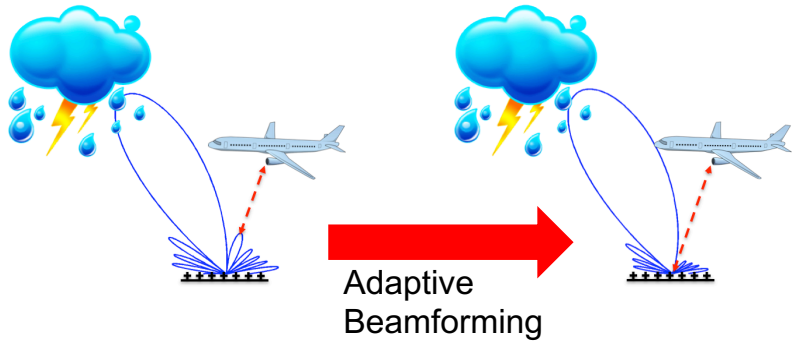

Figure 3.9: Illustration of adaptive beamforming. Since the main lobe is pointed at the storm, the backscattered signal from the aircraft is considered clutter. Adaptive beamforming can automatically adjust the sidelobe levels so that a null is located in the direction of the aircraft to minimize its impact on the signal of interest.

The general flow chart for adaptive beamforming is shown in Figure 3.10. Compared to Figure 3.5, the key difference is the utilization of the received signals in an adaptive algorithm to determine the weight vector. The adaptive algorithm can have different complexity ranging from inverting the spatial covariance matrix to iterations of solving an optimization problem. One of the earlier adaptive beamforming methods was developed by Capon (1969) to study seismic waves. The Capon method is also known as the minimum-variance distortionless response (MVDR) beamformer because it minimizes the total output power (the variance of the output if it has zero mean) while constrains the gain of the beam pattern in the direction of interest to be unity

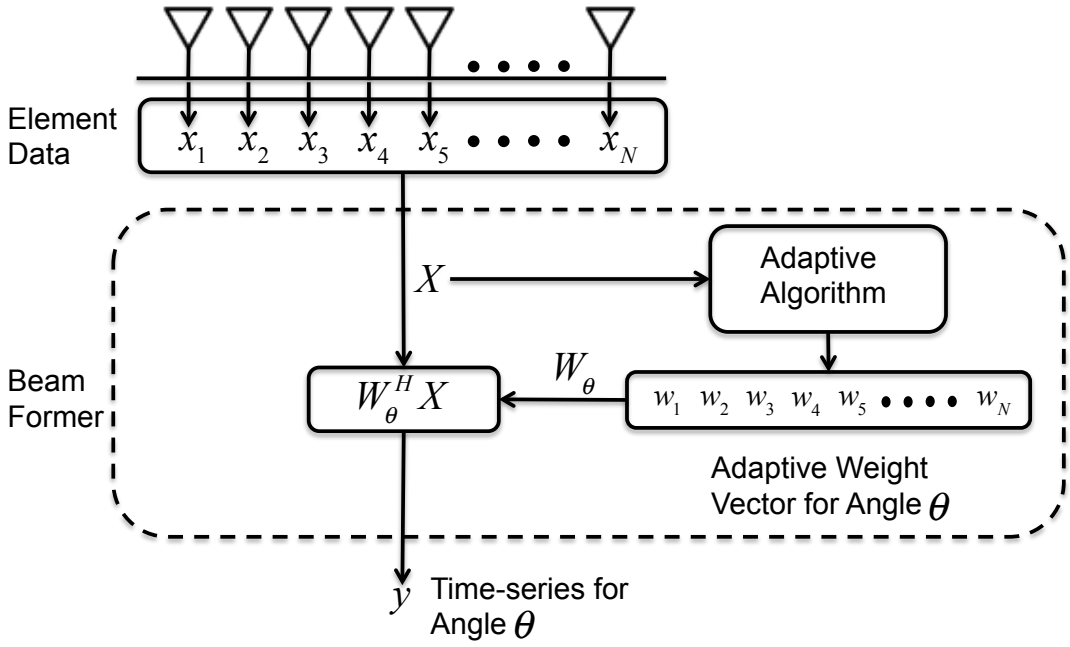

Figure 3.10: Flow chart showing a general adaptive beamforming process. The received signals are weighted and summed to form the final output. The weight vector is determined by an adaptive algorithm that uses the received data as input.

(i.e., it minimizes distortion of the signal of interest). The optimization problem can be written as

$$\min \mathbf{w}^H(\theta)\mathbf{R}\mathbf{w}(\theta) \text{ subject to } \mathbf{w}^H(\theta)\mathbf{a}(\theta) = 0, \tag{3.16}$$

where θ is the direction of interest and $\mathbf{R}$ is the spatial covariance matrix given by

$$\mathbf{R} = \mathrm{E}\left\{\mathbf{x}\mathbf{x}^H\right\}. \tag{3.17}$$

The element in row m and column n of $\mathbf{R}$ is the covariance between the received signals from the mth element and the nth element of the array, and its amplitude and phase contains information about the power and direction of a wave arriving at the array. Using the example from Figure 3.6, the received signals at the mth and nth elements are given by

$$v_m(t) = e^{-j\frac{2\pi}{\lambda}(m-1)d\sin(\theta)}s(t), \tag{3.18}$$

$$v_n(t) = e^{-\frac{2\pi}{\lambda}(n-1)d\sin(\theta)}s(t), \tag{3.19}$$

respectively. The covariance is given by

$$\begin{aligned} r_{m,n} &= \mathrm{E}\{v_m(t)v_n^*(t)\} \\ &= e^{-j\frac{2\pi}{\lambda}(m-n)d\sin(\theta)}\mathrm{E}\{s(t)s^*(t)\} \\ &= \sigma_s^2 e^{-j\frac{2\pi}{\lambda}(m-n)d\sin(\theta)} \end{aligned} \tag{3.20}$$

where σ_s^2 is the power of $s(t)$. It is clear from Equation (3.20) that the amplitude of the covariance term is related to the power of the signal of interest and

the phase of the covariance term contains information about the direction of the signal of interest (θ). The solution to the optimization problem in Equation (3.16) is

$$\mathbf{w}(\theta) = \frac{\mathbf{R}^{-1}\mathbf{a}(\theta)}{\mathbf{a}^H(\theta)\mathbf{R}^{-1}\mathbf{a}(\theta)}. \tag{3.21}$$

Simple substitution of Equation (3.21) into (3.1) can confirm that the output of the Capon beamformer is equal to $s(t)$, as desired. In practice, the true spatial covariance matrix is unknown and must be estimated. A common estimator for the spatial covariance matrix is

$$\hat{\mathbf{R}} = \frac{1}{M}\sum_{m=0}^{M-1} \mathbf{x}(mT_s)\mathbf{x}^H(mT_s), \tag{3.22}$$

where it is assumed that M samples spaced T_s seconds apart are available. As long as M is greater than N, the estimated covariance matrix should be invertible. However, for acceptable performance, it is usually recommended to have $M \geq 2N$ (Van Trees 2002). Beyond being able to automatically adjust the beam pattern to the scanning environment, Capon beamforming also has superior point-target angular resolution than Fourier beamforming (Stoica and Moses 2005); however, it is sensitive to errors in the steering vector. Errors in the steering vector could be caused by inexact knowledge of the array geometry or the true angle of the signal of interest. Small errors in the steering vector can cause Capon's method to attenuate the signal of interest and can result in biased signal-power estimates. Also note that the only constraint on the beam pattern is that the gain is unity in the direction of interest. It is possible

to have high gains for other directions with weak signals, and this possibility of high sidelobe levels makes Capon beamforming unattractive for weather surveillance.

In recognition to the sensitivity of Capon beamformer to errors, Diagonal loading became a popular method to generate variations of Capon beamformer that are more robust (Stoica and Moses 2005). The general formulation for an adaptive beamformer with diagonal loading is

$$\mathbf{w}(\theta) = \frac{(\mathbf{R} + \Upsilon\mathbf{I})^{-1}\mathbf{a}(\theta)}{\mathbf{a}^H(\theta)(\mathbf{R} + \Upsilon\mathbf{I})^{-1}\mathbf{a}(\theta)} \tag{3.23}$$

where Υ is the loading factor and $\mathbf{I}$ is the N-by-N identity matrix. Note that when Υ is set to 0, the solution is identical to Capon beamfomer, and when Υ is very large such that $(\mathbf{R} + \Upsilon\mathbf{I}) \approx \Upsilon\mathbf{I}$, the solution is identical to Fourier beamformer. Mathematically, diagonal loading is equivalent to adding white noise to the received signal, and the solution should converge to Fourier beamforming when white noise dominates the received signals since the Fourier beam has the minimal white noise gain (Stoica and Moses 2005). When the noise power is small (Υ is small), the adaptive beam will focus more on minimizing the power of interference signals rather than minimizing the noise power. The optimal choice of loading factor would depend on the application, and there are no hard rules governing the selection.

3.4 Challenges for Phased-Array Weather Radars

Despite the numerous advantages of a phased-array radar such as electronic steering and adaptive beamforming, there are some unique challenges when used for weather surveillance in an multifunction system. The first challenge is to meet the strict timeline requirements. The functional requirements for MPAR state that aircraft and weather surveillance missions need to have update times of 4.8 seconds and 60 seconds, respectively (FAA 2013). Assuming a future MPAR has four planar faces (Weber et al. 2007) where each face only needs to scan a 90° sector instead of a full 360° volume, the four-faced configuration can reduce the volume update time for weather surveillance from the existing four to five minutes to a little longer than one minute since all faces can be operated simultaneously. However, the weather surveillance must be completed in less than 60 seconds (to allow time for aircraft surveillance missions) without compromising data quality or coverage (spatial sampling). Simultaneous receive beams can further reduce the volume update time, and calculations by Zrnić et al. (2015) showed that three simultaneous receive beams per face are needed to achieve the desired timeline. Different approaches to achieve the required simultaneous receive beams and their associated problems were described briefly in Chapter 1. In the approaches where a spoiled transmit beam is used, instead of using aggressive tapering on receive to drive down the two-way sidelobe levels to meet MPAR's requirements, adaptive

beamforming can be used to generate estimates with acceptable quality. For a dish antenna or nonadaptive beams, since the pattern cannot be changed, they must be designed to be provide acceptable data quality in the worst-case scenario. However, the worst-case scenario occurs rarely, and it is possible that estimates with acceptable quality can be generated with beam patterns with higher sidelobe levels than what would be required for the worst-case scenario.

Adaptive beamfoming is a potential solution to the high sidelobe levels of simultaneous receive beams, but it also brings its own challenges for phased-array weather radars. Figure 3.11 shows an example of an adaptive beam pattern generated with Capon method. The blue solid line shows a dish antenna beam pattern as a reference for comparisons. The red solid line shows the Capon beam pattern steered to -25°. The dish antenna pattern can be seen to be significant only in the main lobe region of the beam, while the Capon beam pattern has sidelobes that even exceed the peak of the main lobe. Since Capon beamformer seeks to minimize the power of the output signal, sometimes it could amplify and phase-shift signals from other directions in order to achieve the minimum output power, especially in situations where coherent signals arrives at the array from different directions. This behavior of the sidelobe levels in the Capon pattern poses a significant problem for weather radar calibration discussed in the previous chapter. Recall that the two assumptions

needed to be able to estimate reflectivity from received signal power are: 1) the product $\eta(\mathbf{r})f^4(\theta,\phi)$ is negligible outside the resolution volume defined by the beam pattern and the range weighting functions, and 2) the reflectivity is constant within the resolution volume. The first assumption is unlikely to hold since there are regions with sidelobe levels that are 20 dB higher than the main lobe peak. Even with the assumption that the reflectivities in those high sidelobe regions are very low so that the product $\eta(\mathbf{r})f^4(\theta,\phi)$ is near zero, the second assumption for calibration is still broken. The resolution volume is no longer well defined for the Capon beam pattern. It is impossible to tell scatterers from which region contributed most significantly to the received signal power since there are many lobes with high gains. The dashed line in Figure 3.11 shows the estimated signal power as a function of angle for both receive patterns, which can be converted to reflectivity estimates through calibration. For dish-antenna estimates, since the receive pattern has low sidelobe levels and a narrow main lobe, both assumptions for calibration are likely to be satisfied, and reflectivity estimates differ from the signal power estimates by a constant factor. On the other hand, despite Capon beamforming's attempt to reduce sidelobe levels in the directions with higher signal power (e.g., around -10°), the sidelobe levels are not low enough to ensure signals outside the resolution volume associated with the main lobe are negligible. As a result, Capon signal-power estimates are biased compared to the dish-antenna signal-power

estimates, and Capon estimates cannot be converted to reflectivity estimates in a straightforward manner. To overcome this calibration challenge for adaptive beamforming, an adaptive algorithm that operates in beamspace is proposed next.

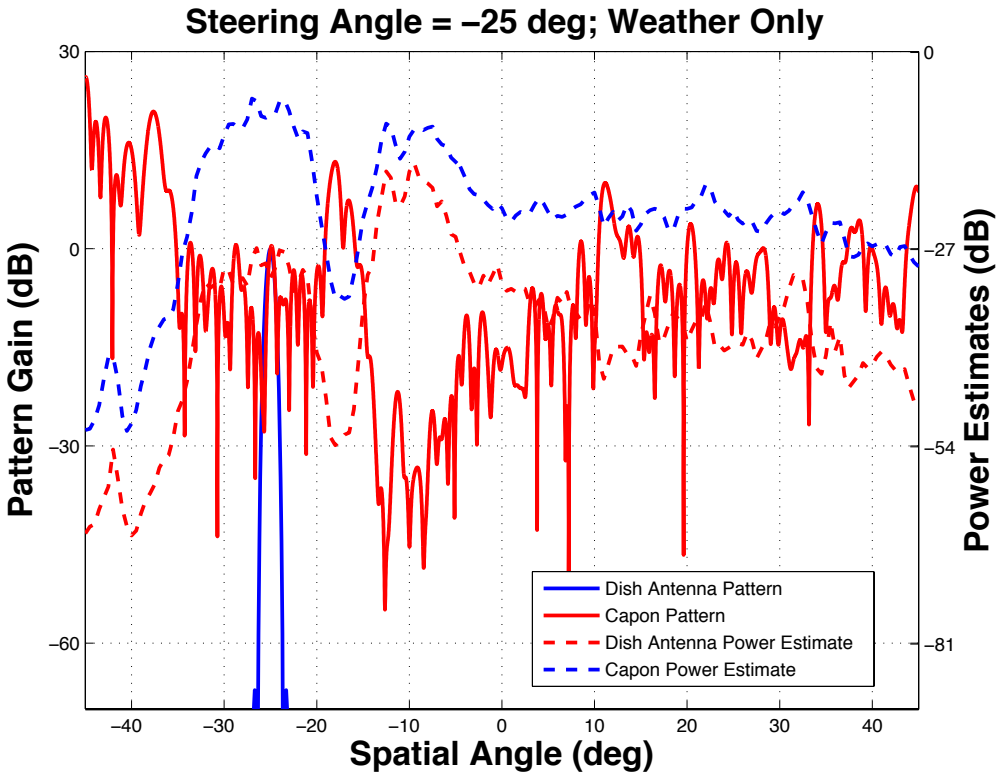

Figure 3.11: Comparison between a dish antenna beam pattern (blue solid line) and an adaptively formed Capon beam pattern (red solid line) and the signal power estimates generated using dish antenna (blue dash line) and Capon beamforming (red dash line). The main lobes of both patterns are pointed at -25°, but the Capon pattern has unacceptable high sidelobe levels for weather radar (Nai et al. 2016) ©2016 IEEE.

Chapter 4

Adaptive Beamspace Processing

In order to meet the demanding timeline requirements, an MPAR system will likely utilize simultaneous receive beams. As discussed in previous chapters, using simultaneous receive beams could result in unacceptable two-way side-lobe levels for non-adaptive beam patterns. Adaptive beamforming can be used to automatically adjust the beam pattern based on signals present in the environment, but the resulting estimates cannot be calibrated in a straight-forward manner. One possible approach to have an adaptive beamforming algorithm that produces accurate and calibrated estimates and automatically rejects interference and clutter signals is to utilize "beamspace" processing. This chapter will introduce the concept of beamspace and describe the proposed adaptive beamspace algorithm. Finally, simulated and real data will be used to demonstrate the advantages and limitations of the proposed algorithm. Sections of the text in this chapter are from Nai et al. (2016).

4.1 Beamspace Processing

As discussed in Chapter 3, phased-array radars offer significantly more flexibility in terms of adaptive scanning, and adaptive beamforming compared to a dish-antenna radar. However, the price is increased computational complexity, especially for the all-digital architecture that processes digitized data from all receiving elements. For some adaptive beamforming algorithms, such as Capon's method, the estimated spatial covariance matrix needs to be inverted for the algorithm to function. In an array with thousands of elements, it would require an unrealistically large number of samples to produce an invertible estimate of the spatial covariance matrix. In an attempt to reduce the number of samples needed for adaptive beamforming, approaches based on the concept of beamspace have been proposed (Chapman 1976; Bienvenu and Kopp 1984; Brookner and Howell 1986; Li and Liu 1994). The term beamspace means that the adaptive algorithm operates on the output of beamformers rather than receiving elements. Algorithms that use the output of receiving elements are said to operate in element space. Figure 4.1 shows a flow chart of a general adaptive beamspace algorithm where fixed initial beams are used to generate the input to the adaptive algorithm. The final time series for a direction of interest is generated by multiplying the adaptive weights with the output of the initial beams and summing. In Figure 4.1, the input to the adaptive algorithm is K dimensional instead of N dimensional. The most important advantage of

operating in beamspace instead of element space is that the dimensionality of the problem is reduced ($K < N$), which means that fewer samples are required to produce an invertible estimate of the covariance matrix. Also, the lower dimensionality reduces the computational complexity of the adaptive algorithm in most cases. Many adaptive algorithms that operate in element space can be used in beamspace with small modifications (Van Trees 2002). Some classical direction-of-arrival estimation methods, such as MUSIC and ESPIRT, have also been adapted to operate in beamspace (Zoltowski et al. 1993; Xu et al. 1994). More recently, adaptive beamspace beamforming also has found application in medical imaging (Rodriguez-Rivera et al. 2006; Nilsen and Hafizovic 2009), sonar (Somasundaram 2011), communications (Vook et al. 2013), and radar (Li and Lu 2006; Hassanien and Vorobyov 2009; Lamare et al. 2010).

4.2 Adaptive Beamspace Algorithm Description

Adaptive beamspace is a two-step processing scheme that first forms a set of deterministic beams and feeds the output of the deterministic beams into an adaptive algorithm to generate the final output time series. Some obvious benefits of reduced data dimensionality are lower computational complexity and improved robustness to array perturbations (Van Trees 2002, Section 6.9). Furthermore, by using low-sidelobe initial beams, the sector covered by the initial beams is emphasized in the adaptive beamformer optimization process. For

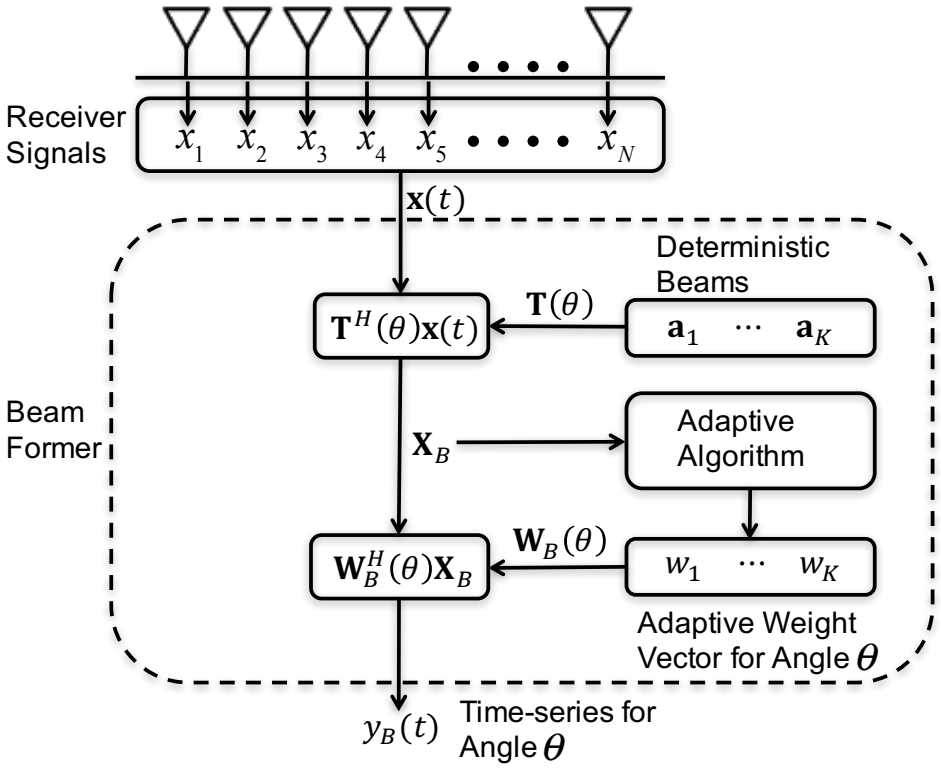

Figure 4.1: Flow chart showing the steps of adaptive beamspace processing. The initial beams are formed by **T** operating on the receiver outputs, and the outputs of the initial beams are fed into an adaptive algorithm to generate the adaptive weights that are used to form the final output. The adaptive algorithm can be determined by application requirements (Nai et al. 2016)

weather radars, the low-sidelobe initial beams also help control the sidelobe levels of the final beam pattern, which would allow for the estimation of reflectivity from the received signal power as discussed in Section 2.2.2. Accurate estimation of reflectivity is critical for weather radars since many algorithms (e.g., quantitative precipitation estimation, hydrometeor classification) use reflectivity as an input. On the other hand, reducing the data dimensionality results in loss of degrees of freedom that can be used to reject interference signals. However, as long as the number of interference signals is smaller than the number of initial beams used in the beamspace adaptive processing, the algorithm can still reject them. The algorithm is described in detail next.

4.2.1 Algorithm Overview

Mathematically, adaptive beamspace processing can be written as

$$y_B(t) = \mathbf{w}_B^H(\theta)\mathbf{T}^H(\theta)\mathbf{x}(t)\,, \tag{4.1}$$

where $y_B(t)$ is the beamspace estimate of the signal from direction θ, $\mathbf{w}_B(\theta)$ is the vector of adaptive weights applied to the output of the initial beams, and $\mathbf{T}(\theta)$ is the beamforming matrix that forms the initial set of deterministic beams. In the rest of the chapter, the θ dependence for $\mathbf{w}_B$ and $\mathbf{T}$ is dropped for simplicity.

4.2.2 Initial Beams

The beamforming matrix $\mathbf{T}$ for the proposed adaptive beamspace processing is constructed as

$$\mathbf{T} = \left[\begin{array}{ccccccc} \mathbf{a}(\theta - K\Delta\theta) & \cdots & \mathbf{a}(\theta) & \cdots & \mathbf{a}(\theta + K\Delta\theta) \end{array} \right], \tag{4.2}$$

where each column of $\mathbf{T}$ is a steering vector for the array, and a total number of $2K+1$ beams are used. The center column, referred to as the center beam, is steered to point in the direction of interest, denoted by θ, and the other columns, referred to as the side beams, are steered to point at the angles immediately around θ with a separation of $\Delta\theta$. $\Delta\theta$ should be set to ensure both that there are no gaps between the half-power points of adjacent beams and that adjacent beams do not overlap too much (rendering the output signals redundant). Due to the beam broadening effect, the beamwidth of the initial beams at edge of the scanning range should be considered when determining the value of $\Delta\theta$. For a fixed $\Delta\theta$, it is better to have a small gap between the half-power points of adjacent beams than to have initial beams overlap significantly at the edge of the scanning range. The adaptive algorithm can still attenuate interference sources located between two initial beams, but it is difficult to prevent signal cancellation if the output of the initial beams are highly correlated. It is possible to have $\Delta\theta$ change as a function of the scanning angle to account for the beam broadening effect. However, such a scheme would result in nonuniform azimuthal sampling and increase the number of initial

beams that would need to be formed. For this work, uniform azimuthal sampling is assumed to match the WSR-88D azimuthal sampling and to simplify the analysis. Figure 4.2 shows an example of five initial beams. The center beam (red line) is steered to 1.5° (black dashed line), and the side beams are steered to -0.5°, 0.5°, 2.5°, and 3.5° respectively. The beam separation in this example is 1°, which is the 3-dB beamwidth of the initial beams without amplitude taper. The number of initial beams determines the degrees of freedom available and the computation complexity of the adaptive stage. If there are more sources of interference or clutter than the number of initial beams, the adaptive algorithm will not be able to successfully cancel all of them due to the limited degrees of freedom. The taper of the initial beams controls the sidelobe behavior of the overall beam pattern outside the volume covered by the initial beams, and a fast roll-off is desirable for weather radars as discussed in previous chapters. Since the taper also controls the 3-dB beamwidth of the initial beams, the choice of taper must carefully balance beamwidth, sidelobe roll-off, and sensitivity loss. Simulations described later are used to determine the number, the separation between, and the tapering of the initial beams.

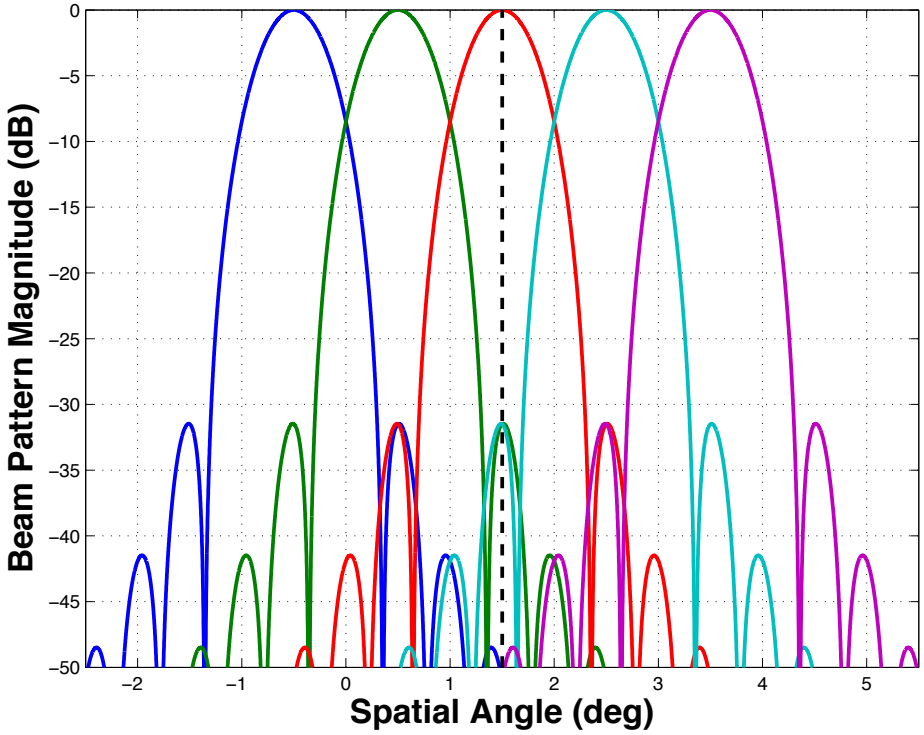

Figure 4.2: Example receive beam patterns of the initial beams. In this example, five initial beams are formed with tapered Fourier weights. The center beam (red line) is steered to 1.5° (black dashed line) and two side beams are formed on each side of the center beam separated by 1°.

4.2.3 Adaptive Algorithm

The adaptive algorithm attempts to solve an optimization problem that can be written as

$$\min_{\mathbf{w}} \mathbf{w}^H \mathbf{T}^H \mathbf{R}_{xx}(0) \mathbf{T} \mathbf{w}$$

$$\text{subject to } \mathbf{w}^H \mathbf{T}^H \mathbf{a}(\theta) = 1 \text{ and } \mathbf{C}|\mathbf{w}| \leq \mathbf{0}, \tag{4.3}$$

where $\mathbf{C}$ is a matrix describing the additional constraints on the magnitude of the adaptive weights, and $\mathbf{0}$ is a column vector with all elements equal to zero. The additional constraints on the magnitude of the adaptive weights are based on the observation that any interference signal present in the center beam should also be present in one or more of the side beams. Since the output of a side beam contains information about the interference signal in the center beam, it can be used adaptively to reduce the overall impact of the interference signal. Moreover, while observing dominant weather phenomena, the initial beams should produce uncorrelated outputs since they are pointed in different directions and the resolution volumes should have only a small amount of overlap. Since we are interested in the resolution volume corresponding to the center beam, it makes little sense to combine signals from other resolution volumes. Therefore, in the case of no interference signal, it is best to constrain

the adaptive weights for the side beams so that the final output is mainly determined by the output of the center beam. The additional constraints can be written mathematically as an inequality constraint of the form

$$\begin{bmatrix} 1 & 0 & -c_1 & 0 & 0 \\ 0 & 1 & -c_2 & 0 & 0 \\ 0 & 0 & 0 & 0 & 0 \\ 0 & 0 & -c_4 & 1 & 0 \\ 0 & 0 & -c_5 & 0 & 1 \end{bmatrix} \begin{bmatrix} |w_1| \\ |w_2| \\ |w_3| \\ |w_4| \\ |w_5| \end{bmatrix} \leq \mathbf{0} \tag{4.4}$$

where c_i is the weight magnitude constraint for the side beams that are set to a small or a large positive number depending on whether the side beam is selected to be constrained or not. If a side beam is selected to have a constrained adaptive weight, the corresponding c_i is set to a positive value much smaller than one, forcing the magnitude of the adaptive weight to be less than the magnitude of the adaptive weight for the center beam; otherwise, c_i is set to a large positive number to force the inequality to be satisfied for any adaptive weight. The value of the constraint should be chosen to help control the peak sidelobe level of the final beam pattern and to allow the optimization problem to have a feasible solution. To determine whether a beam should have a constrained adaptive weight, the magnitude of the correlation coefficient between the output of the side beams and the output of the center beam can be used as a proxy for the presence of interference. When a strong interference signal

is present, the correlation coefficient between the outputs of beams containing the interference signal should be large (i.e., close to one); and when no interference signal is present, the correlation coefficient between the outputs of beams should be small (a function of the amount of overlap between the initial beams). A threshold can be set such that a side beam with correlation coefficient exceeding this threshold is considered to contain the interference signal, and a side beam with correlation coefficient below the threshold is considered not to contain the interference signal. If a side beam is determined not to contain the interference signal, its adaptive weight is constrained. For the side beams that contain the interference signal, their output powers are used as an approximation for their angular distance from the direction of the interference signal, with the beams with higher output power considered to be pointing closer to the interference source. The side beams that are closer to the interference than the center beam will have an unconstrained adaptive weight, while the side beams that are farther away from the interference than the center beam will have a constrained adaptive weight. These angular-distance-based constraints prevent the scenario in which a side beam has an adaptive weight larger than the adaptive weight of the center beam, which could result in the final beam pattern having higher sidelobes than the peak of the main lobe. The optimization problem in Equation (4.3) is solved using the interior-point method implemented in MATLAB's optimization toolbox (Byrd et al. 2000).

An example illustrating the adaptive algorithm for a simulated scenario with an interference source located at 0° and the direction of interest at 1.5° is shown in Figure 4.3. In this example, the initial beams are pointed at -0.5°, 0.5°, 1.5°, 2.5°, and 3.5° respectively, and the simulated interference signal power is much stronger than the attenuation provided by the sidelobe levels of the initial beams at 0°. The top-left panel of Figure 4.3 plots the correlation coefficient of the output of each initial beam with the output of the center beam. As expected, the outputs of the two side beams pointed at -0.5° and 0.5° that are mostly impacted by the interfering signal have the highest correlation coefficient with the output of the center beam. The outputs of the two side beams pointed at 2.5° and 3.5° have correlation coefficients less than an arbitrary threshold of 0.8, and, as a result, will have constrained adaptive weights. Simulations will be used later to empirically determine an optimal threshold value. The top-right panel of Figure 4.3 shows the output signal power for the initial beams. Since the two side beams that have unconstrained adaptive weights also have output signal powers greater than the output signal power of the center beam (indicating they are closer to the interference signal than the center beam), no additional constraint for these two beams is needed. The bottom-left panel of Figure 4.3 shows the adaptive weights for the initial beams after solving the optimization problem, and the red dash line indicates the maximum magnitude that satisfies the inequality constraint in

Equation (4.3). The adaptive weights for the side beams pointed at -0.5° and 0.5° have magnitudes larger than the maximum magnitude that satisfies the inequality constraint (indicating they are unconstrained, as designed), and the magnitude of the adaptive weights for the side beams pointed at 2.5° and 3.5° are at the maximum allowable magnitude under the constraint. The bottom-right panel shows the beam pattern of the initial beams (thin lines) and the resulting adaptive beam pattern (thick black line). As desired, the resulting pattern has a sharp null located at 0° to reject the interference signal while the sidelobe levels are all below the mainlobe peak. This overall pattern is more significantly non-zero in a small volume, similar to that of a dish antenna pattern, implying that it is much more likely to satisfy the calibration assumptions stated in Section 2.2.2, which would allow the traditional estimation of reflectivity from received signal power.

4.3 Simulations and Analysis

To evaluate the adaptive beamspace algorithm described previously, a simple weather time-series simulator for a uniform linear array (ULA) was developed. The simulation set up, the criteria used to evaluate the performance of the different algorithms, simulation parameters and results are presented and discussed next.

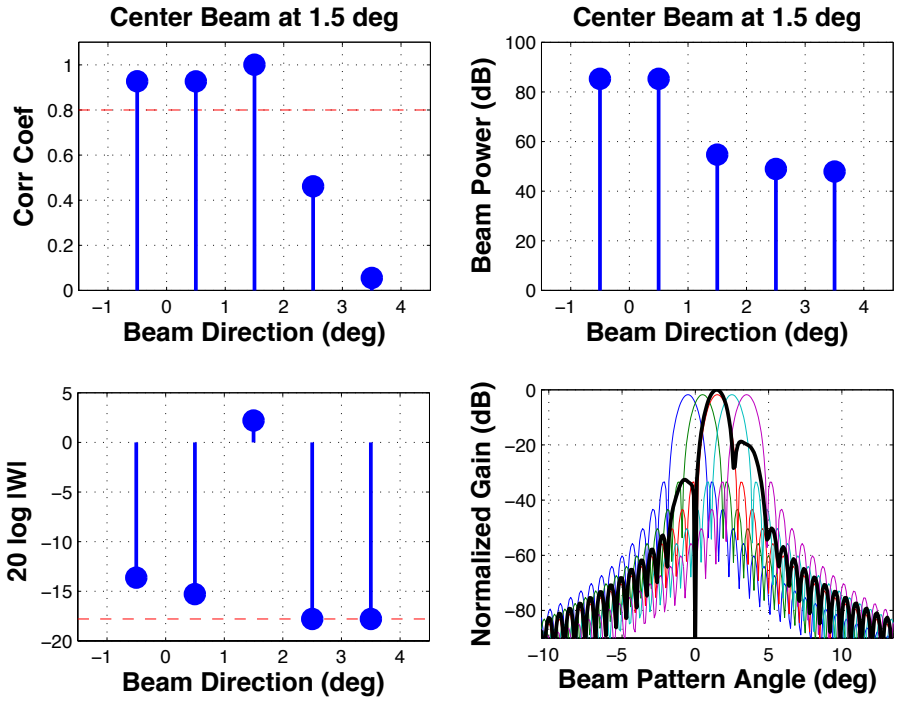

Figure 4.3: Example illustrating adaptive beamspace processing using a five-beam configuration. The top-left panel shows the correlation coefficient of the output of the initial beams with the output of the center beam; the top-right panel shows the output signal power for each of the initial beams; the bottom-left panel shows the adaptive weights for each of the initial beams; and the bottom-right panel shows the beam patterns for the initial beams and the resulting beam pattern. In this example, the two side beams pointed at -0.5° and 0.5° are selected to have unconstrained adaptive weights based on correlation coefficient and signal power considerations. The resulting beam pattern shows that the adaptive step successfully places a null at 0° to reject the interference signal (Nai et al. 2016) ©2016 IEEE.

4.3.1 Simulation Setup

The simple weather time-series simulator generalizes Equation (3.6) to include multiple sources to simulate the received signals. Assuming L sources are

present and M samples are collected, the received signals for an N element array are given by

$$\mathbf{X} = \mathbf{AS} + \mathbf{n}. \tag{4.5}$$

where $\mathbf{X}$ is an $N \times M$ matrix where the ith row is the M samples of the received signal from the ith receiving element, $\mathbf{A}$ is an $N \times L$ matrix whose columns consist of steering vectors $\mathbf{a}(\theta_i)$ $(i = 1, 2, \cdots, L)$ where θ_i is the direction of the ith source signal contained in the ith row of $\mathbf{S}$, and $\mathbf{n}$ is white noise generated by the receivers. $\mathbf{S}$ is an $L \times M$ matrix where the ith row contains the M samples of the time series from the ith source. Since only an ULA is simulated, it is assumed that beamforming is done in the azimuthal direction for a fixed elevation. For simplicity, only signals from a fixed range are simulated and no propagation effects are taken into account. Furthermore, it is assumed that the elements in the ULA are identical and isotropic, and the spacing between the elements is one half of the wavelength so that no grating lobes are present. The simulated array is designed to be scanned from -45° to 45°, and the maximum beamwidth is 1° at the edge of the scanning range to match the spatial resolution of the WSR-88D.

The source signals are simulated by a scattering-center-based approach, where the entire volume of space to be observed is sliced into non-overlapping small volumes separated in azimuth by 0.1°, and each of these small volumes is considered to be filled with hydrometeors with a given reflectivity,

mean radial velocity, and spectrum width. The overall backscattered signal for one volume is represented by an equivalent scattering center that generates a time series with statistical properties that describe the properties of all the hydrometeors filling the volume. The time series are simulated using a well-known time-series simulator used for weather radar (Zrnić 1975). This scattering-center-based approach is intended to capture the distributed nature of weather signals. Profiles of reflectivity, mean radial velocity, and spectrum width needed to generate these time series can have artificial shapes or can be realistic profiles from real data. After simulating the time series for each scattering center, Equation (4.5) is used to generate the received signals, where each row in **S** is the time series of a scattering center. White noise is simulated to have a power of 0 dBm for each receiver. Point-target interference is then simulated and added at fixed angles.

To have a more realistic simulation, operational constraints for a real radar must be considered as well. For an MPAR system using a spoiled transmit beam, the spoiled beamwidth is determined by considering the timeline requirement and sensitivity requirement. Once the transmit beamwidth is fixed, it is reasonable to only form receive beams within the beamwidth of the transmit beam, since volumes outside the transmit beamwidth are not illuminated and should have much smaller basckscatterered signal. As the transmit beam is steered to illuminate different azimuth angles, different groups of receive

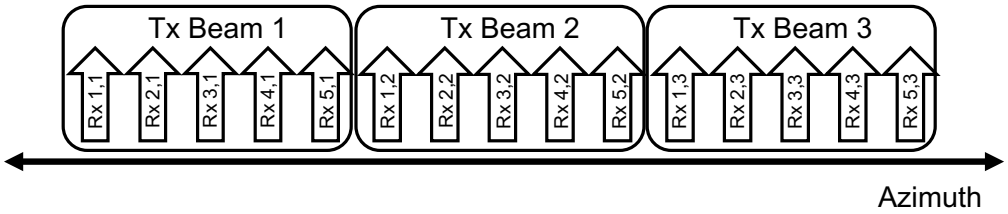

Figure 4.4: Illustration of a concept of operation involving beamspace adaptive processing. A spoiled transmit beam (indicated by a box labeled Tx Beam) is used in conjunction with simultaneous receive beams (indicated by arrows labeled $\mathrm{Rx}_{i,j}$) covering the volume illuminated by the transmit beam. The first subindex of the receive beams indicates the position of the receive beams within a cluster of beams that covers the volume illuminated by a single transmit beam. The second subindex of the receive beams indicates the transmit beam for which this receive beam was formed. For any direction of interest, a contiguous set of receive beams (from different transmit beam is allowed) centered on that direction is used as input to the adaptive beamspace algorithm to generate the final estimate for a particular direction.

beams can be formed and stored to be used as the initial beams for the adaptive beamspace algorithm as shown in Figure 4.4. In the example shown in Figure 4.4, three transmit beams and the associated groups of five receive beams are shown. Assuming the number of initial beams in the adaptive beamspace algorithm is set to five, several different scenarios can occur depending on the direction of interest. If the direction of interest corresponds to the center of a transmit beam (e.g., direction of $\mathrm{Rx}_{3,2}$), the entire group of receive beams (e.g., $\mathrm{Rx}_{1,2}$, $\mathrm{Rx}_{2,2}$, $\mathrm{Rx}_{3,2}$, $\mathrm{Rx}_{4,2}$, and $\mathrm{Rx}_{5,2}$) can be used as the initial beams. If the direction of interest corresponds to other directions (e.g., the direction of $\mathrm{Rx}_{5,1}$), receive beams from different transmit beams must used (e.g., $\mathrm{Rx}_{3,1}$,

$Rx_{4,1}$, $Rx_{5,1}$, $Rx_{1,2}$, and $Rx_{2,2}$) as the initial beams. In these scenarios, there is an additional time-lag between the two sets of received beams, which is equal to the dwell time; this time lag could impact the performance of the algorithm. For weather signals, this additional time-lag reduces the correlation between the initial beams, which should help the algorithm to prevent it from using side beams to cancel signals from the center beam. However, for interference signals, especially a signal with large spectrum width, the reduced correlation due to the additional time-lag could prevent the algorithm from successfully using side beams to cancel the interference signal if those side beams are from different transmit beams. After the received signals are simulated and processed with the adaptive beamspace algorithm, estimates of the spectral moments are produced with standard estimators discussed in Section 2.2.3 and compared to estimates produced by a dish antenna radar.

The motivation behind the development of the adaptive beamspace algorithm is to meet the timeline requirement for MPAR system while producing calibrated and accurate estimates of the meteorological variables. Two situations could significantly impact the accuracy of the estimates: presence of clutter and interference signals and/or presence of reflectivity gradients. Therefore, the evaluation of the adaptive beamspace algorithm is focused on these two scenarios as well. There are two aspects of the performance of adaptive beamspace algorithms regarding mitigating interference signals that need to

be quantified: the ability to produce accurate estimates of the radar variables and the ability to reject interference signals. Delta bias, described in Hood et al. (2010) and Nai et al. (2013b) is used to quantify the ability to accurately estimate the radar variables. The delta biases are calculated by subtracting the dish-antenna estimates for the volume when no interference is present from the estimates produced by the beamforming methods when interference is present. By using delta bias instead of absolute bias, the biases inherent to the estimators are eliminated. Since the goal of weather radars is to accurately estimate the radar variables, the ability to reject interference is measured by the angular spread of the impact of the interference on the estimates of these radar variables. If the interference signal results in a delta bias that is greater than a threshold, it is considered to have impacted a particular radar variable. The angular spread of the interference is then defined as the angular distance between the first angle on each side of the interference signal where it no longer impacts the radar-variable estimates. Figure 4.5 uses signal power estimate produced by a dish-antenna system with an strong interference signal located at 0° to illustrate this measure. The black dashed line is the threshold for acceptable bias (1 dB) in this example, and the directions within the red dashed line are where the signal-power estimates have biases larger than the 1-dB threshold. In this example, the angular spread of the interference would be 4.5° (from -2.2 ° to 2.3°). The angular spread of interference is more meaningful than the

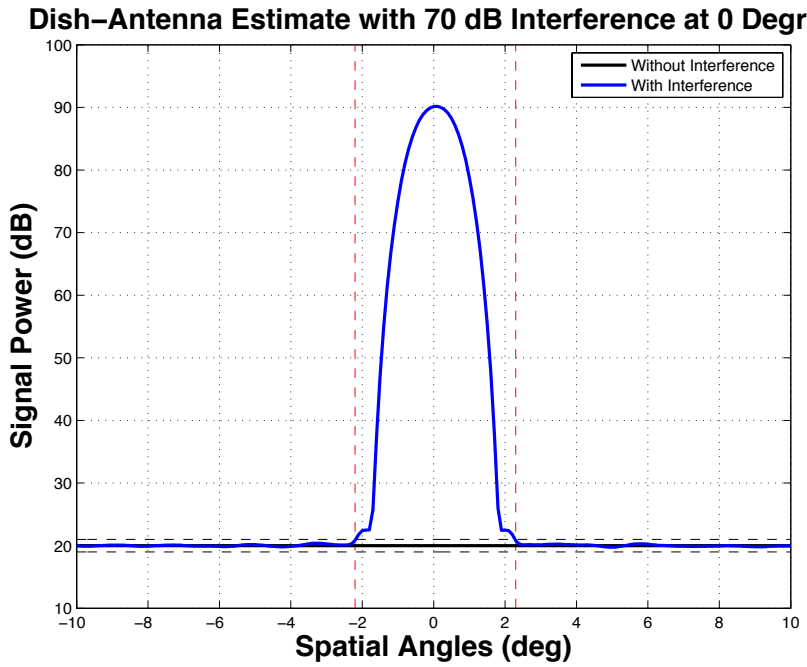

Figure 4.5: Illustration of the spread-of-interference for a dish-antenna system. The simulated profile is a uniform profile with a 20-dB signal-to-noise ratio and an interference signal located at 0° with a 90-dB signal-to-noise ratio. The black dashed line shows the 1-dB bias threshold, and the red dashed lines shows where the estimates contain biases larger than that threshold. In this scenario, the spread of interference is from -2.2° to 2.3° for a total of 4.5°. The goal of adaptive beamspace algorithm is to reduce this spread to as little as possible to preserve as much useful data as possible.

traditional measure of improvement in signal-to-interference-plus-noise ratio to weather radar users since it describes the amount of data that are unusable due to interference. For the results presented later, the delta-bias thresholds are set to 1 dB for signal power, and 1 $\mathrm{m\,s^{-1}}$ for mean radial velocity and spectrum width.

Regarding reflectivity gradients, a delta-bias comparison with dish-antenna estimates makes less sense because it is known that the dish-antenna estimates are biased in the presence of strong gradients. Therefore, in evaluating the ability to handle reflectivity gradients, biases against the model input are used, and dish-antenna biases are provided as a comparison. Similar to the angular spread of interference defined previously, a zone of impact due to the gradient is similarly defined as the collection of directions where the estimates have larger biases than a preselected threshold value. Figure 4.6 shows a gradient model (blue line) and signal-power estimates from a dish-antenna system (red line) and a PAR using the adaptive beamspace algorithm (green line). It is clear that both estimates have biases exceeding the 1 dB threshold (black dashed line) from 23.5° to 25.5°. Despite the estimates from the adaptive beamspace algorithm being closer to the model input, the biases exceeded the threshold; therefore, both dish-antenna and adaptive beamspace have a zone of impact of 2° in this example. For both interference signals and reflectivity gradients, the biases away from the contamination source are calculated to ensure that the algorithm did not introduce additional biases in the attempt to mitigate the impact of the contamination source.

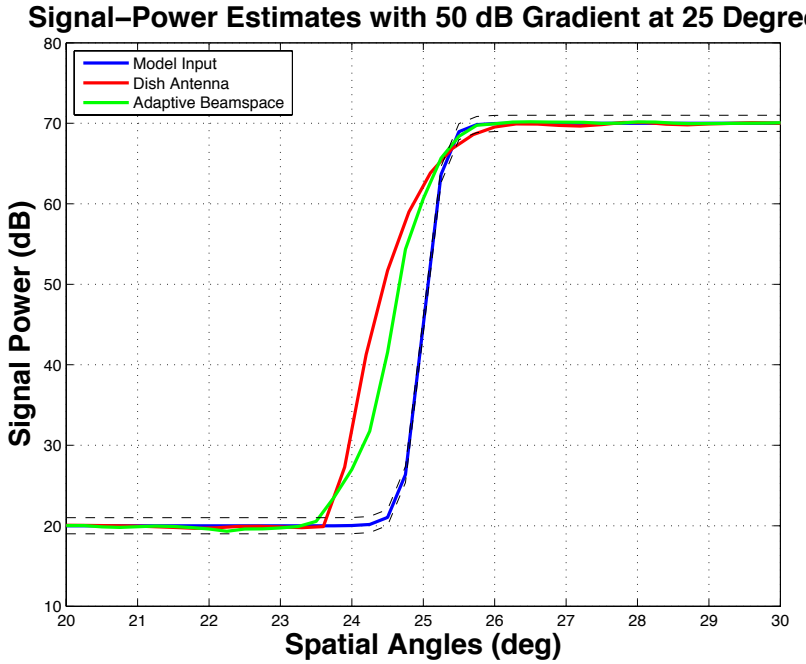

Figure 4.6: Illustration of the zone of impact for a reflectivity gradient. The simulated gradient is at 25° and has a 50-dB change in signal power. The blue line shows the signal-power profile used as input to the time-series simulator, the red and green lines are the signal-power estimates of the dish-antenna system and a PAR system using the adaptive beamspace algorithm. Estimates from both systems show biases exceeding a 1-dB threshold (black dashed line) from 23.5° to 25.5°, and, therefore, have a 2° zone of impact. The goal of adaptive beamspace algorithm is to match the dish-antenna performance in most situations despite having higher two-way sidelobe levels.

4.3.2 Simulation Parameters

Simulations with different signal characteristics were done to determine the optimum parameters of the algorithm and to evaluate its performance. Table 4.1 lists some key characteristics (and their respective range) of the simulated signals, and Table 4.2 lists the algorithm parameters that need to be

determined. Two categories of simulations were used to evaluate different aspects of the algorithm: 1) uniform power distribution with added interference to evaluate the algorithm's capability in mitigating interference and clutter, and 2) power distribution with gradients to evaluate the impact of adaptive sidelobe levels on estimation of the spectral moments.

The interference rejection simulations have four important characteristics (first four rows in Table 4.1) that should be varied. The signal-to-noise ratio (SNR) controls the power level of the uniform distribution, which impacts whether the adaptive algorithm focuses on rejecting interference signals or on reducing the noise power. The clutter-to-signal ratio (CSR) controls the power level of the interference signals, which need to be varied to ensure the algorithm can mitigate strong interference signals as well as maintain the quality of estimates when little or no interference is present. The location of the interference signal with respect to the transmit beam could also impact the performance, especially when the interference is located near the edge of the transmit signal. In such a scenario, the time delay between successive transmit beams could reduce the correlation coefficient between the initial beams to be lower than the threshold and thus prevent the algorithm from using the correct side beams for interference cancellation. Two types of interference signal (coherent and white noise) are used to showcase the best- and worst-case scenarios. A coherent signal should have high correlation coefficients regardless

of time delay (best case) while white noise has zero correlation at any nonzero time delay (worst case).

The reflectivity gradient simulations also have four important parameters that should be varied (the last four rows in Table 4.1). The step size of the gradient describes the amount of change between the low and high level of the gradient, and the extent controls the distance over which the power distribution rises from the low level to the high level. The equation used to generate the profile is

$$P = \frac{H}{1 + e^{[k(\theta - \theta_0)]}} \tag{4.6}$$

where H is the step size, θ_0 is the direction where the power is half way between the two extreme power levels, and k controls the steepness of the curve. Figure 4.7 shows an example profile where θ_0 is -2°, the step size is 70 dB, and the extent of the variation is 2°. The sigmoid curve described by Equation (4.6) was chosen over a trapezoid profile because it provides a smooth transition between the levels, which is more realistic compared to the sharp corners in a trapezoid profile. The location of maximum gradient (θ_0) with respect to the center of the transmit beam should be varied to evaluate the potential impact of having the gradient span two consecutive transmit beams. In addition to the location of the maximum gradient within the transmit beam, its location with respect to the broadside of the array also needs to be varied to account for the impact of the beam broadening effect that is inherent to phased-array radars.

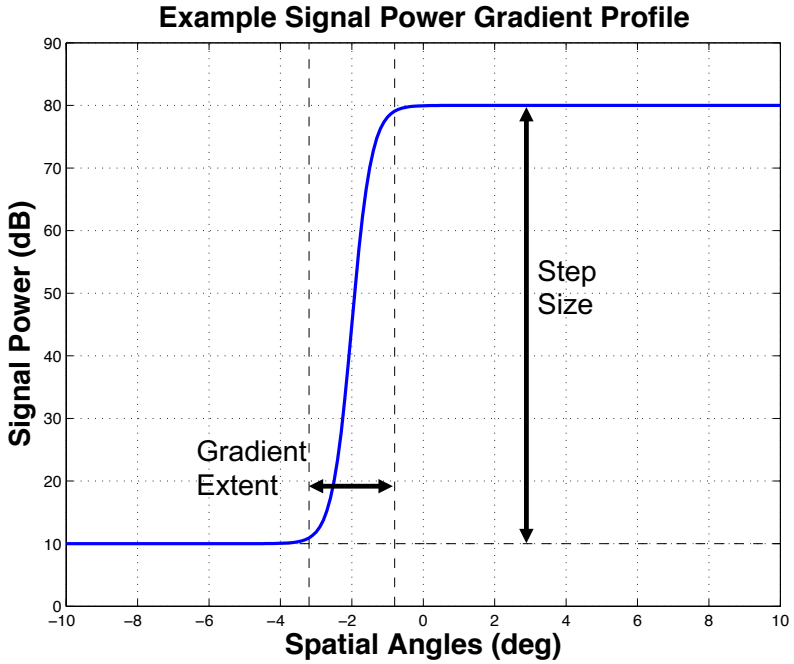

Figure 4.7: Example gradient profile generated by Equation (4.6) with $\theta_0 = -2$, $H = 70$, and $k = 3.6$. With this k value, the spatial extent of the gradient is 2°. This profile represents a worst-case scenario where the large change in the profile occurs over a short distance.

Some signal characteristics were not varied because their impact on the algorithm are minimal. The mean Doppler velocity of the weather signal and the interference signal were fixed in the simulation because they only impact the phase of the sample-time correlation at non-zero lags, which is not used by the algorithm. Another fixed variable is the spectrum width of the weather signal. Spectrum width impacts the magnitude of the sample-time correlation of the weather signals at non-zero lags, which could have an effect on the algorithm when receive beams from different transmit beams are used. However, wider spectrum widths would only make the signals decorrelate faster resulting in

even lower correlation coefficients between the initial beams. This is ideal for the algorithm because it should not use side beams to cancel weather signals.

Table 4.1: Variations of the simulated weather and interference signals.

Parameter Name	**Parameter Value**
SNR (dB)	0, 5 $\cdots$ 30
CSR (dB)	-10, 0, 10 $\cdots$ 70
Interference location wrt center of transmit beam	left edge, center, right edge
Interference type	coherent and noise
Step size (dB)	10, 20, $\cdots$, 70
Gradient extent (deg)	1, 2, 3, 4, 5
Maximum gradient location wrt center of transmit beam	left edge, center, right edge
Maximum gradient location wrt broadside (deg)	0, 20, 40

Beyond changing the parameters of the simulated signals, there are parameters of the algorithm that need to be determined. As listed in Table 4.2 , three of the five parameters of the adaptive beamspace algorithm relate to the amplitude taper, and the separation and number of initial beams. The separation between the initial beams could impact the ability of the algorithm to mitigate interference and clutter signals. If the initial beams are separated by a large amount, there could be gaps (on the order of the 3-dB beamwidth of the initial beams) between two adjacent beams. If an interference source is located in

this gap, the signal from a side beam must be amplified to correctly cancel the interference signal. This amplification is highly undesirable since it will also amplify the signals coming through the mainlobe of this side beam. On the other hand, if the initial beams are spaced close together, the resolution volume of the beams will have significant overlap, which will result in the outputs of the initial beams being correlated. As a result of increased correlation between the outputs, it is possible that the algorithm will consider weather signals present in all beams to be interference and will attempt to cancel them. The number of initial beams controls the degrees of freedom of the adaptive step, and increasing the number of initial beams will allow the algorithm to cancel multiple interference signals coming from different directions. However increasing the number of initial beams also increases the computational complexity of the algorithm and could result in behaviors similar to those exhibited by Capon beamforming. Lastly, the tapering of the initial beams affects the behavior of the sidelobes of the overall pattern far away from the main lobe. By adjusting the weights for the side beams, the sidelobe level of the overall pattern in the directions of the main lobe of the side beams can be adjusted, but the sidelobes far away from the main lobe of the overall pattern are determined by the roll-off rate of the initial beams.

The last two parameters of the algorithm play significant role in the adaptive step. The correlation threshold affects which side beam is used in the

cancellation of the interference signal. Due to beam overlap, even without an interference signal, the output of the initial beams will have some correlation. A correlation threshold below this naturally occuring correlation would result in the algorithm adaptively (and incorrectly) canceling weather signals. On the other hand, if the correlation threshold is too high, the algorithm can miss interference signals, especially when receive beams from different transmit beams are used together. The weight constraint sets an upper limit on the sidelobe levels of the final beam pattern in the directions of the the side beams. If the maximum weight ratio is too small, the adaptive algorithm could fail to find a feasible solution, which would result in no interference mitigation; if the maximum weight ratio is too large, the final beam pattern would have high sidelobe levels that could result in biased estimates.

Table 4.2: Variations of the parameters of the adaptive beamspace algorithm.

Parameter Name	**Parameter Value**
Initial beam separation (deg)	0.1, 0.2, $\cdots$, 2.0
Number of initial beams	3, 5,$\cdots$,21
Initial beam taper	Hann, Taylor
Correlation threshold	0.4, 0.45, $\cdots$, 0.95
Weight magnitude constraint	0.01, 0.02, $\cdots$, 2.0

4.3.3 Simulation Results and Analysis

After identifying the key parameters of the algorithm and the simulated signals, simulations for different scenarios were completed where one hundred realizations of the signals from each scattering center were used to find the mean biases. The mean Doppler velocities for weather signals were set to -10 $\mathrm{m\,s^{-1}}$, and the spectrum widths for weather signals were set to 2 $\mathrm{m\,s^{-1}}$. The mean Doppler velocities for the interference signals were set to 10 $\mathrm{m\,s^{-1}}$. The simulation results used to determine the algorithm parameters are presented first; results for interference rejection and reflectivity gradients are presented next to illustrate the advantages and limitations of the proposed adaptive beamspace algorithm.

4.3.3.1 Algorithm Parameter Optimization

The first step in evaluating the beamspace adaptive algorithm is to determine the algorithm parameters listed in Table 4.2. An exhaustive search within the five dimensional space for the optimal parameters is not feasible. As a result, the parameters were determined in two independent groups: the initial beam parameters and the adaptive step parameters.

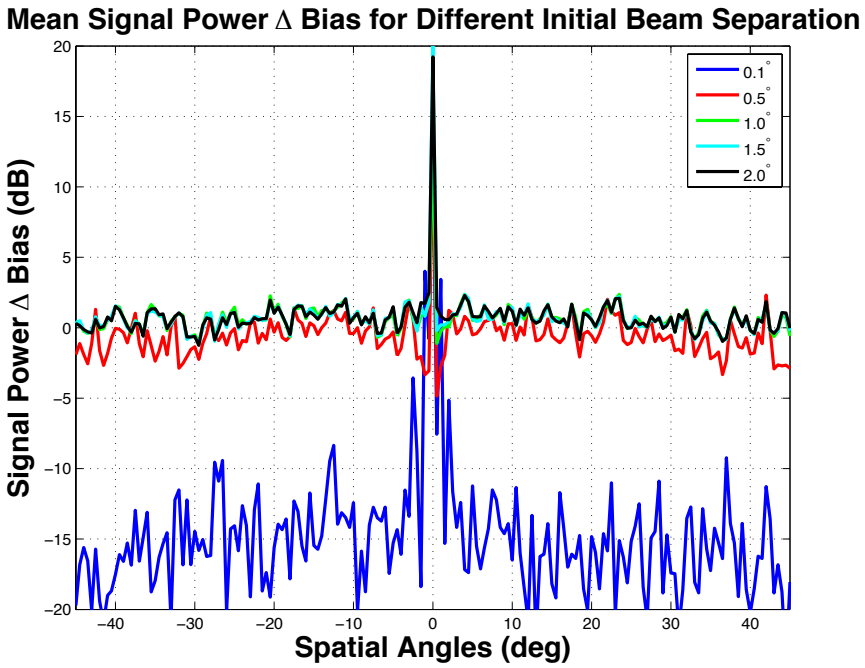

Figure 4.8: Signal-power delta bias for different amounts of initial beam separation with five initial beams. If the initial beams are too close (0.1° separation, blue line), the algorithm significantly underestimates the signal power. The performance is similar for separations greater or equal to 1°.

The parameters related to the initial beams are the separation of the beams, the number of beams, and the tapering of the beams. In the simulated scenario, the weather signals have a uniform power distribution, and an interference source is located at 0°. The interference signal has a SNR of 80 dB and the weather signal has a SNR of 10 dB. Five initial beams with a von Hann taper were used, and the separation was varied from 0.1° to 2.0° in 0.1° increments. Figure 4.8 shows the mean signal-power delta-bias for different beam separations. It can be clearly seen that initial beams with 0.1° separation (blue line) resulted in signal-power estimates with large negative biases. This is the

result of having initial beams with significant overlap, which produced outputs that are highly correlated. The adaptive algorithm will treat the situation similar to when an interference signal is present and will attempt to cancel the weather signals using the side beams, which results in negative biases in signal-power estimates. The negative biases are reduced as the beam separation is increased. The biases in signal-power estimates for 1.0°, 1.5°, and 2.0° separation are very similar.

The next set of simulations used the same weather and interference setup with a fixed initial beam separation and variable number of initial beams. In Figure 4.9, the initial beam separation was set to 1.0°, and the number of initial beams was varied from 3 to 11 in 2-beam increments. The results show that as the number of initial beams increased, negative delta-biases developed in the signal-power estimates. In Figure 4.10, the initial beam separation was set to 0.5° and the number of initial beams was varied from 3 to 21 in 2-beam increments. The results show a similar pattern as Figure 4.9, where delta biases became more negative as the number of beams increased, and the magnitude of the delta bias is larger for a 0.5° separation than that for a 1.0° separation as expected. This behavior is consistent with results from Capon beamforming, which significantly underestimates the signal power, as shown in Figure 3.11. As the number of initial beams increases, the degrees of freedom in the adaptive step approaches that of Capon beamformer, and it

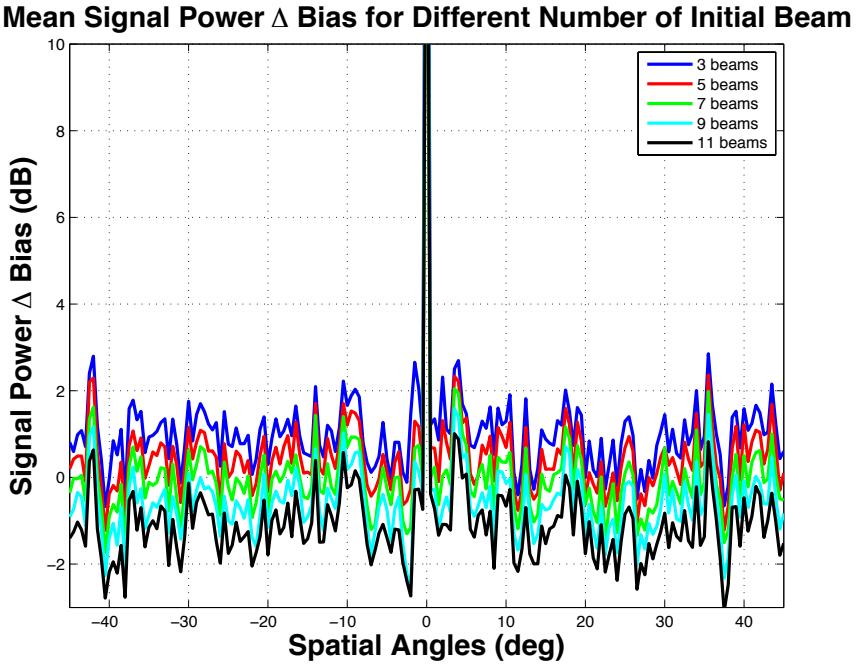

Figure 4.9: Signal-power delta bias for different numbers of initial beams with a beam separation of 1.0°. For all simulations, the adaptive algorithm successfully limited the spread of the interference signal. With a large number of initial beams (9 or 11), there are negative biases in the signal power estimates.

can be expected that the final output of the beamformer will converge to that of Capon beamformer as well.

In Figures 4.8 and 4.9, the initial beam separation and the number of initial beams were treated as independent variables. However, it is possible to vary both at the same time but have a constant coverage area. For example, if the initial beam separation was 0.5°, it would take 13 beams to cover 6°, while it would only take seven beams if the initial beam separation was set to 1.0°. The constant coverage ensures that the presence or absence of the interference signal in a group of initial beams is the same for the different configurations.

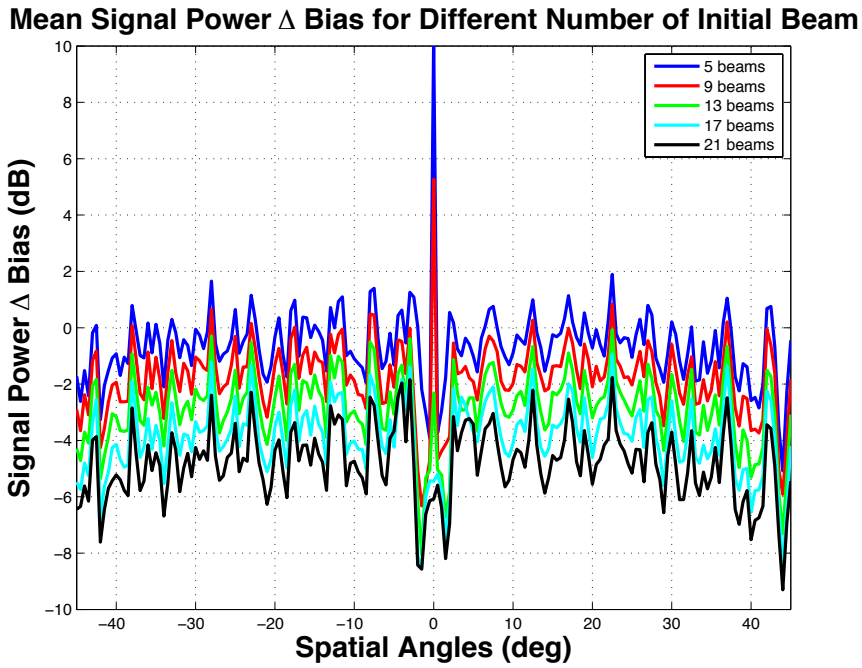

Figure 4.10: Signal-power delta bias for different numbers of initial beams with a beam separation of 0.5°. For all simulations, the adaptive algorithm successfully limited the spread of the interference signal. However, there are negative biases in the signal power estimates, and the biases increase as the number of beams increases.

Figure 4.11 shows the performance for three different initial beam configurations with the same coverage area. Despite having the same coverage area, the 0.5° separation configuration still has a negative delta bias. The other two configurations have no noticeable biases in signal-power estimates. This shows that for a fixed volume, there is no benefit in using more beams closely spaced to mitigate interference.

The last parameter impacting the initial beams is the amplitude tapering. The trade-off in choosing a taper is between having a narrow main lobe to preserve spatial resolution and having sidelobe levels of the initial beams roll off

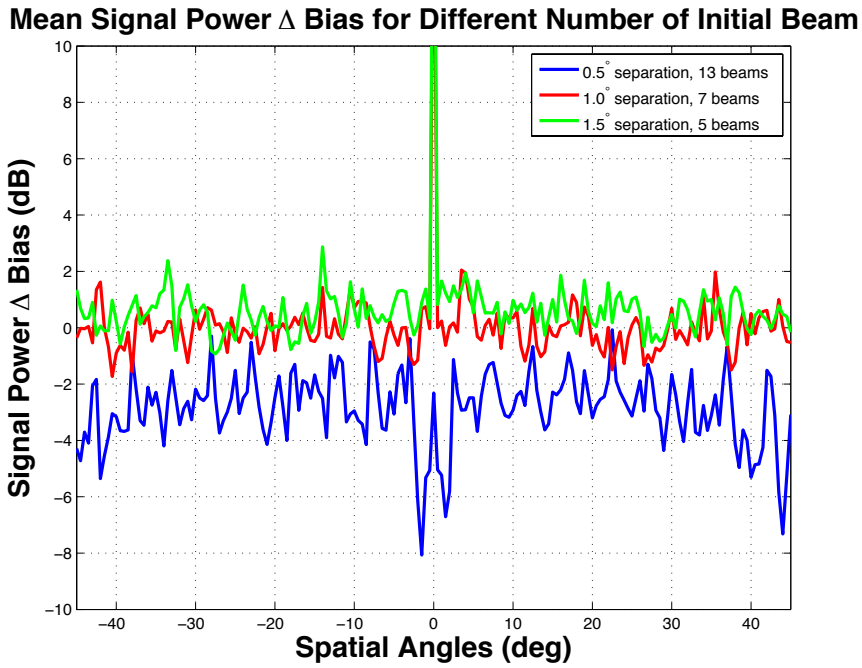

Figure 4.11: Signal-power delta bias for different numbers of initial beams with different separation such that 6° are covered by the group of initial beams. Despite covering the same volume, the estimates for 0.5° separation have a noticeable negative bias. The 1.0° and 1.5° separation have similar performances, matching the results in Figure 4.8.

as a function of angle from the steering direction. The sidelobe roll-off rate does not impact the algorithm's performance in mitigating interference signals from discrete directions, but it could impact the performance of the algorithm when steep reflectivity gradients are present. Figure 4.12 shows initial beams using the von Hann and Taylor tapers. It is clear that the von Hann taper has a wider main beamwidth and a faster sidelobe roll-off compared to the Taylor taper. At 5° away from the steering direction, there is a 30-dB difference between the sidelobe levels of these two tapers, which could significantly impact the estimates when reflectivity gradients are present. Figure 4.13 shows

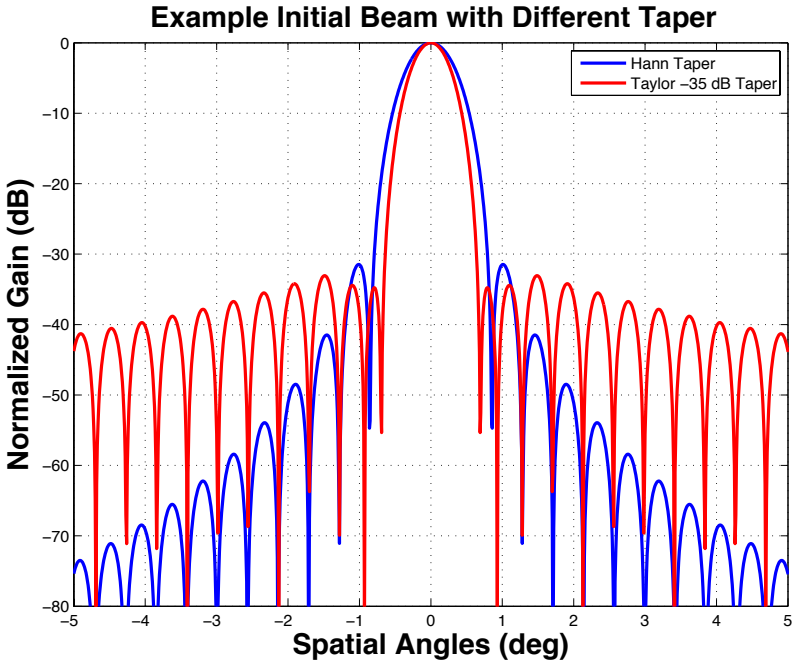

Figure 4.12: Initial beams with von Hann (blue line) and Taylor (red line) tapers. The von Hann taper produces a beam with a wider main lobe with faster sidelobe roll off, while the Taylor taper produces a narrower main lobe with a much smaller sidelobe roll-off rate. The Taylor tapered beam has a -40 dB sidelobe level 5° away from the steering direction compared to that of -73 dB for the von Hann tapered beam. This large difference in sidelobe levels far away from the steering direction can result in significant biases when large gradients are present.

the signal-power delta biases when estimating the profile shown in Figure 4.7 using the tapers shown in Figure 4.12. The slower roll off of the Taylor taper resulted in large biases from -8° to -4° that are far away from the location of the gradient (centered at -2°). Mathematically, the final beam pattern is a sum of the initial beam patterns with each beam weighted by the adaptive weight. As a result, the sidelobes that are closest to the steering direction can

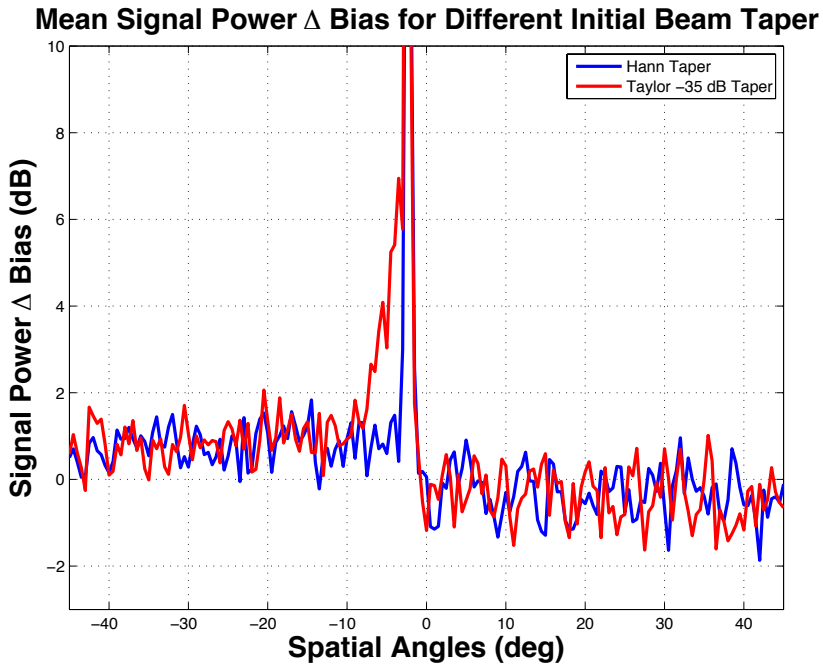

Figure 4.13: Impact of initial beam taper on gradients. The large biases from -8° to -4° in the Taylor taper estimates are the result of high sidelobe levels away from the steering direction. Since the gradient is located at -2°, the high side of the gradient is not sufficiently attenuated by the sidelobes and caused biases in the estimates of the low side of the gradient.

be adjusted automatically depending on the adaptive weight given to the side beams that are pointed near those sidelobes. This implies that the initial beams can have higher peak sidelobe levels close to the steering beam in exchange for fast roll-off away from the steering direction. Based on considerations for main lobe width, peak sidelobe level, and sidelobe roll off, a von Hann taper is chosen for the remainder of the simulations.

Once the parameters governing the initial beams are set, the next step is to determine the parameters for the adaptive step. The correlation threshold is used to determine which side beams have constrained adaptive weights, which

is intended to prevent the algorithm from using side beams to cancel weather signals from the direction of interest. If a strong interference signal (CSR greater than $\sim$20 dB) is present, the correlation coefficient between the output of the initial beams should be close to one because the interference signal overpowers the weather signal in the side beams. Figure 4.14 shows the signal-power delta biases for several different correlation coefficient thresholds. The simulated weather signals have uniform SNR of 20 dB and an interference signal with a CSR of 20 dB was added at 0°. The biases in signal-power estimates are close to -2 dB for a threshold value of 0.4 and are consistent over the spatial angles away from the interference. As shown in Figure 4.15, the biases in signal power estimates decrease as the correlation threshold increases from 0.4 to 0.8 and plateau for threshold values greater than 0.8. A threshold value of 0.75 results in estimates with a mean bias of zero. Varying the CSR of the interference signal between 10 and 30 dB produces similar results. The negative biases for the small correlation threshold values are due to weather signals in the initial beams having correlation above the threshold and mistakenly being canceled in the adaptive step. Since the initial beams overlap, their outputs are not completely uncorrelated despite being steered to different directions. The inherent correlation between the output of the initial beams due to weather puts a lower limit on valid choices for correlation threshold.

For mean Doppler velocity, the mean delta-biases are near zero for all threshold values. For spectrum width, the mean delta-biases decrease from close to 0.5 $\mathrm{m\,s^{-1}}$ to 0.1$\mathrm{m\,s^{-1}}$ as the threshold values increase from 0.4 to 0.9. Since the delta biases are small for velocity and spectrum width for all threshold values, the delta biases for signal power are the dominant factor in determining the value of the correlation threshold. The upper limit on correlation threshold is determined by considering the impact of the interference signal. Ideally, the interference signal should only impact the estimate of the weather signal in the same direction as the interference signal. However, due to beams having non-zero beamwidth, weather signal estimates from directions near the interference signal are usually impacted by it as well. The goal of the algorithm is to limit the angles that are impacted by the interference signal to be as narrow as possible. Figure 4.16 plots the angular spread of the interference signal (with a CSR of 20 dB) for different threshold values. As expected, if the threshold value is too high (≥ 0.8), weaker interference signals could fail to exceed the threshold, which could lead to the side beams having constrained weights and not being used to cancel the interference signal completely. Another set of simulations with uniform weather signals with SNR of 20 dB and an interference signal with a CSR of 10 dB was run, and the results match the results shown here. Based on Figures 4.15 and 4.16, the correlation threshold value is set to 0.75 for the remainder of the simulations.

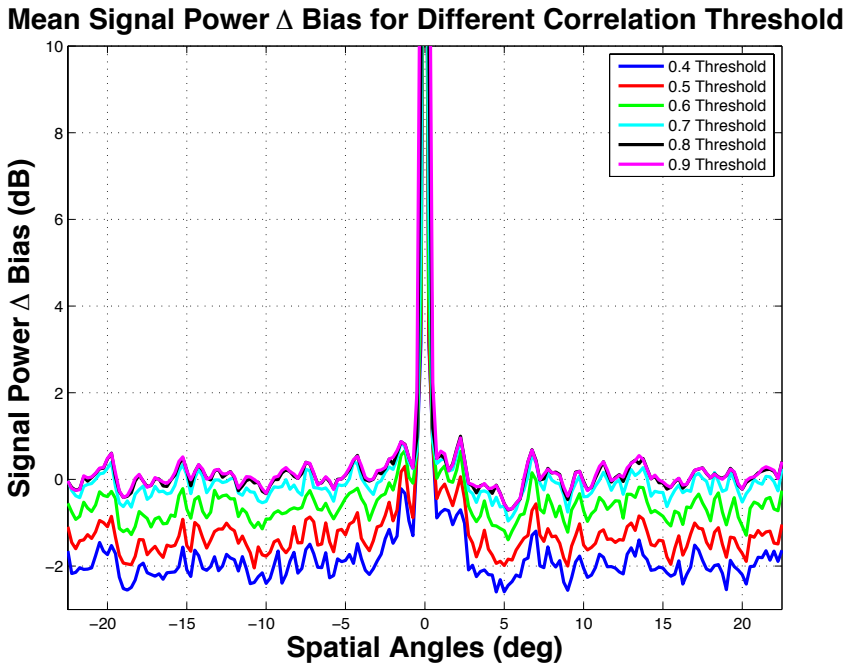

Figure 4.14: Signal-power delta biases for different correlation threshold values. The negative biases for small correlation threshold values are due to weather signals having correlation coefficient above the threshold and being canceled in the adaptive step.

The last parameter of the algorithm is the weight magnitude constraint for the side beams. Since the final beam pattern is a summation of the initial beam patterns multiplied by their respective weights, the weight magnitude constraint sets an upper limit on the sidelobe level of the overall beam pattern in the direction of the side beams. For example, a weight magnitude constraint of 0.1 for the side beam 1° away from the steering direction means that the maximum one-way sidelobe level in that direction for the final beam pattern is -20 dB. Figure 4.17 shows the signal-power delta bias for different weight magnitude constraints. As the weight magnitude constraint increases from 0 to 0.2 in 0.01 steps, the signal-power delta biases are constant at 0.25 dB for

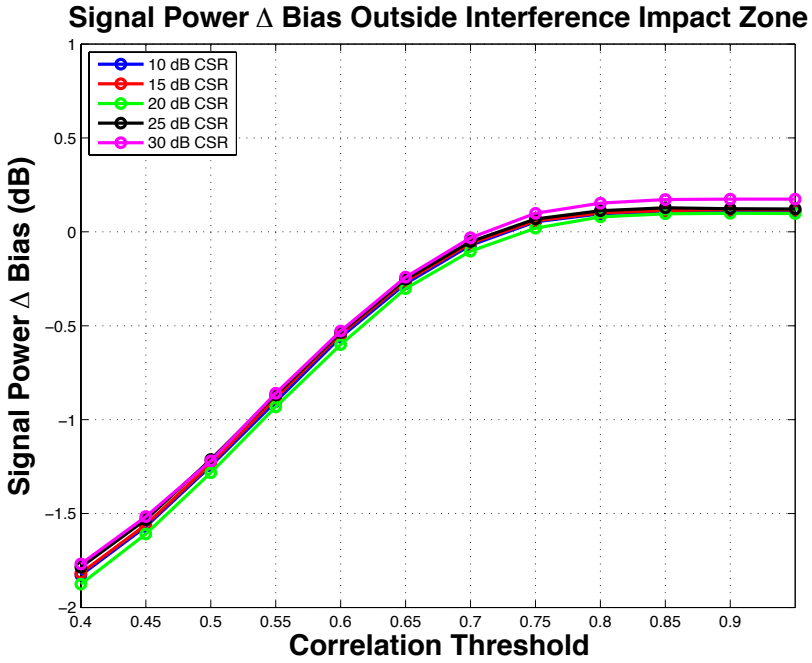

Figure 4.15: Signal-power delta biases for angles outside the interference impact zone for different CSRs. As the correlation threshold increases, the biases decrease at first then stay constant. The strength of the interference signal has no significant impact in terms of determining the optimal correlation threshold. Based on these results, a correlation threshold value of 0.75 results in estimates with zero mean delta-biases.

small weight magnitude constraints (0.01 to 0.08) and linearly decrease for larger weight magnitude constraints (0.09 to 0.2). For the small weight magnitude constraints, sometimes the adaptive step could not find a feasible solution within the allotted iterations, and the interference signal is not canceled successfully, which results in the small positive biases. Note that for a constraint value of zero, the only solution is to use the center beam only and no adaptivity is allowed. This non-adaptive solution does produce a small delta bias as expected. For large weight constraints, the negative biases are the result of

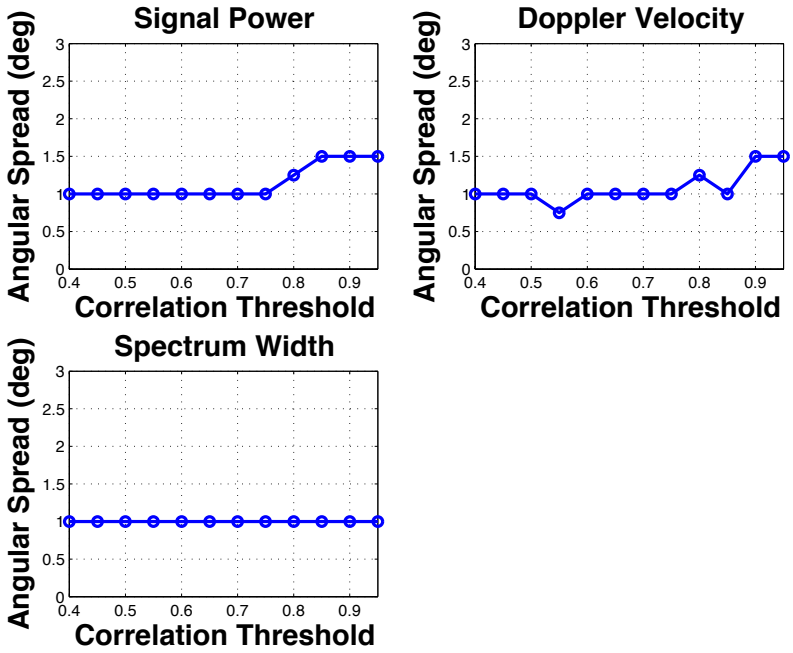

Figure 4.16: Spread of interference signal for different correlation thresholds. When the interference is not strong, it is possible for the correlation between the initial beams containing the interference signal to be smaller than one, and a high threshold value could lead to constrained weights for the side beams, which leads to failed cancelation of the interference signal and more angles with estimates biased by it. For mean Doppler velocity, the spread is constant except for the largest correlation thresholds. For spectrum width, the performance is independent of the correlation threshold.

cancellation of the weather signal. This is consistent with the expectation that with totally unconstrained side beams, the results would be negatively biased similar to that from Capon beamforming. The results for mean Doppler velocity and spectrum width are near zero for all weight constraints. Based on Figure 4.17, the weight magnitude constraint is set to 0.1 for the remainder of the simulations. Table 4.3 shows the parameters value used for the rest of the simulations.

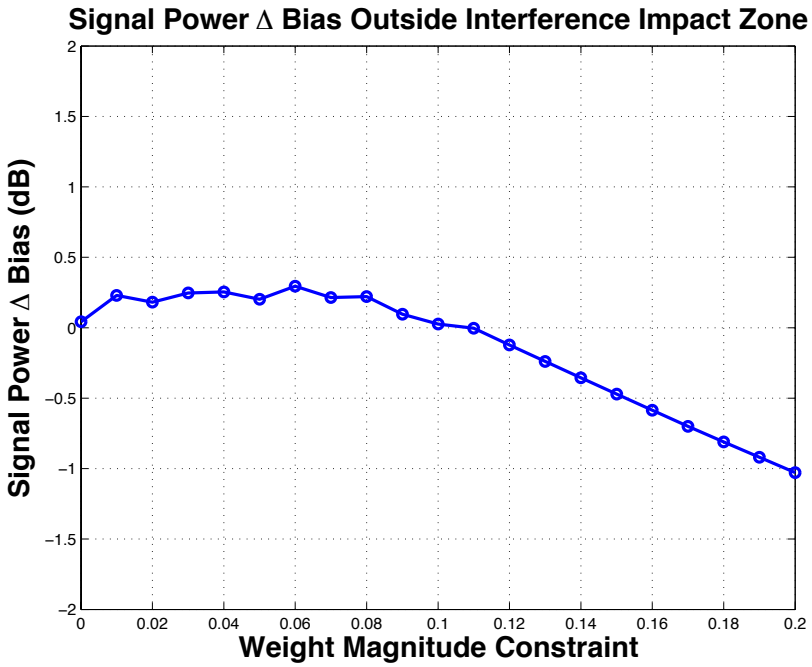

Figure 4.17: Signal-power delta biases for different weight constraints. The positive biases for small weight constraints are due to the algorithm failing to find a solution to the optimization problem, which leads to uncanceled interference signal. The negative biases for large weight constraints are the results of cancellation of weather signals.

Table 4.3: Parameters of Adaptive Beamspace Algorithm

Parameter Name	**Parameter Value**
Initial beam separation	1.0°
Number of initial beams	5
Initial beam taper	von Hann
Correlation threshold	0.75
Maximum weight magnitude	0.1

4.3.3.2 Interference Mitigation

One of the primary goals of utilizing adaptive beamforming is to automatically reject clutter and interference signals from unknown directions. The most important parameters that must be varied to evaluate the ability of the adaptive beamspace algorithm to mitigate interference are the CSR, the SNR, the interference location with respect to the transmit beam, and the interference type as listed in Table 4.1. The first set of simulations evaluated the performance of the algorithm for different CSRs by varying it from -10 to 70 dB in 10-dB increments. The weather profile was a uniform profile with a 20-dB SNR, and the interference source was added at 0°. Figure 4.18 shows the angular spread of the interference signal for these different CSRs for a PAR using the adaptive beamspace algorithm (blue line) and a dish-antenna system (red line). For interference signals with very low CSRs ($\leq$ 0 dB), the impact of the interference signal is minimal due to its low power, and the performance of a PAR using the adaptive beamspace algorithm matches a dish-antenna system. For high-CSR scenarios, the adaptive beamspace algorithm successfully mitigated interference, and the angular spread of the interference signal is much smaller for a PAR using the adaptive beamspace algorithm compared to a dish-antenna system as shown in Figure 4.18. This matches expectations since interference sources with strong power can easily contaminate multiple beams that are steered close to the direction of the interference source, which allows

the adaptive algorithm to use side beams with high correlation with the center beam to successfully mitigate the interference signals. The slight increase in the angular spread of interference in signal-power estimates for the largest CSRs could be caused by statistical fluctuations in the estimation of the angular spread since it is not matched by corresponding increases in Doppler velocity and spectrum width. The most difficult cases are the medium CSRs (10-20 dB) cases where the interference signal does not overpower the weather signal in the initial beams to produce a high correlation between them. In such cases, it is possible that the algorithm fails to determine the appropriate side beams to use to mitigate the interference signal in the center beam. These difficulties are captured by the increased angular spread of interference signal in all three spectral moments for CSRs from 0 to 20 dB in Figure 4.18. However, in these more difficult cases, a PAR using the adaptive beamspace algorithm still outperforms a dish-antenna system. In terms of the estimates away from the interference signal, the algorithm performs well for all CSRs as shown in Figures 4.19, 4.20, and 4.21. For all CSRs, the delta biases are close to zero for all three spectral moments, as desired. This indicates that the algorithm successfully limited the impact of the interference to the nearest directions and the algorithm did not introduce additional biases to the estimates for weather-only directions.

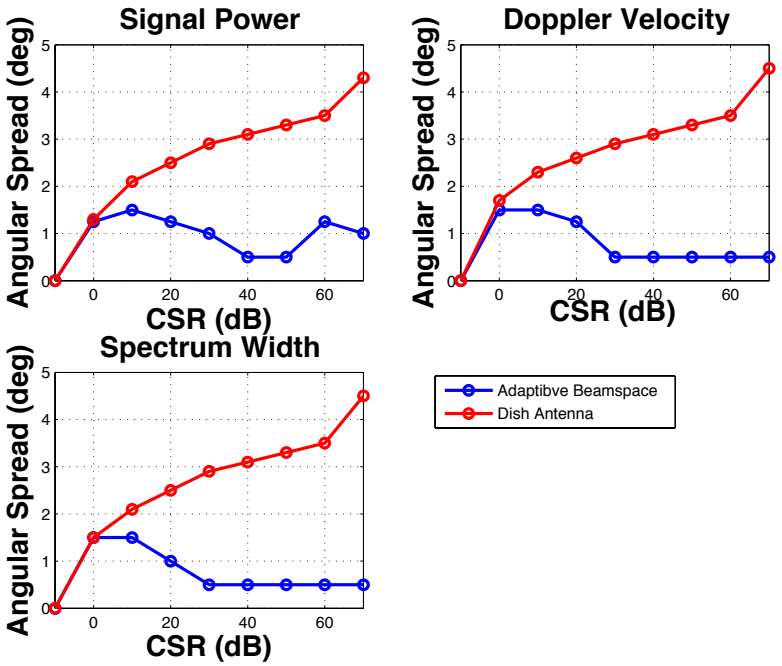

Figure 4.18: Angular spread of interference signal for a PAR using the adaptive beamspace (blue line) and a dish-antenna (red) system with different CSRs. For the lowest CSRs, the weak interference signal does not significantly impact the estimates for angles near the interference direction. For the high CSRs, the algorithm can successfully mitigate the impact of the interference signal. The medium CSRs (10 to 20 dB) are the most challenging cases for the algorithm since the interference signal does not overpower the weather signal in the initial beams to produce a clear determination of which side beams should be used to mitigate the interference signal.

The second set of simulations evaluated the performance of the algorithm for different SNRs by varying SNR from 0 to 30 dB in 5-dB increments. Based on previous discussions on challenging cases for the algorithm, an interference source with a 20-dB CSR was added at 0° to the uniform weather profile. Figure 4.22 shows the angular spread of interference signal for the different SNRs. As expected, the angular spread of interference signal is relatively

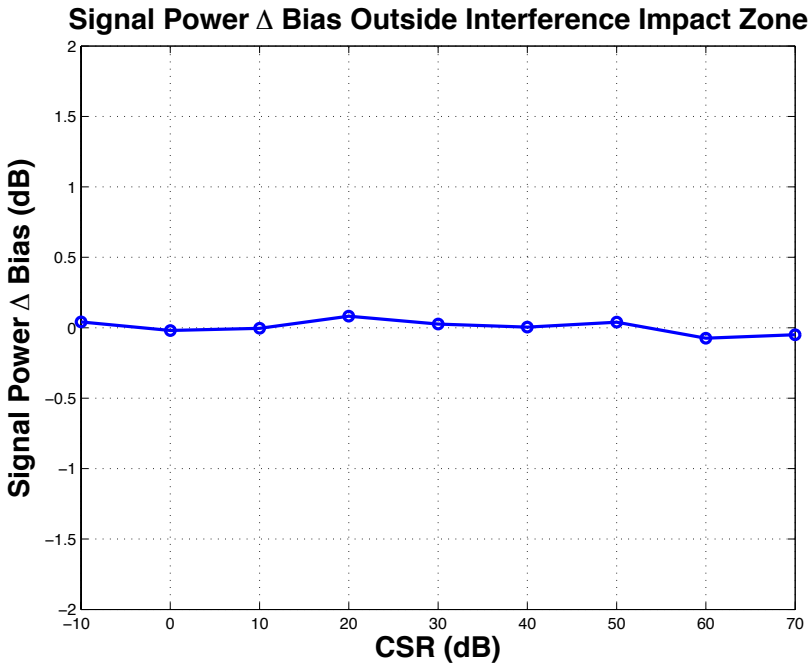

Figure 4.19: Signal-power delta biases away from the interference source for different CSRs. The small biases indicate that the algorithm successfully limited the impact of the interference signal to those directions closest to it, and the algorithm does not introduce additional biases in weather-only situations.

constant across the SNRs except for an SNR of 0 dB. For the 0-dB SNR case, the mean Doppler velocity and the spectrum width show a large increase in the spread of the interference, which is due to the estimation errors caused by the low SNR. Signal-power estimates after subtracting the noise power show no such sharp increase. Figure 4.23 shows the signal-power delta bias away from the interference source. The small biases indicate that the adaptive algorithm is not sensitive to the SNR of the weather signals and can perform well in weak weather scenarios. The results for mean Doppler velocity and spectrum width are similar to that of signal-power and are not shown. Based on these

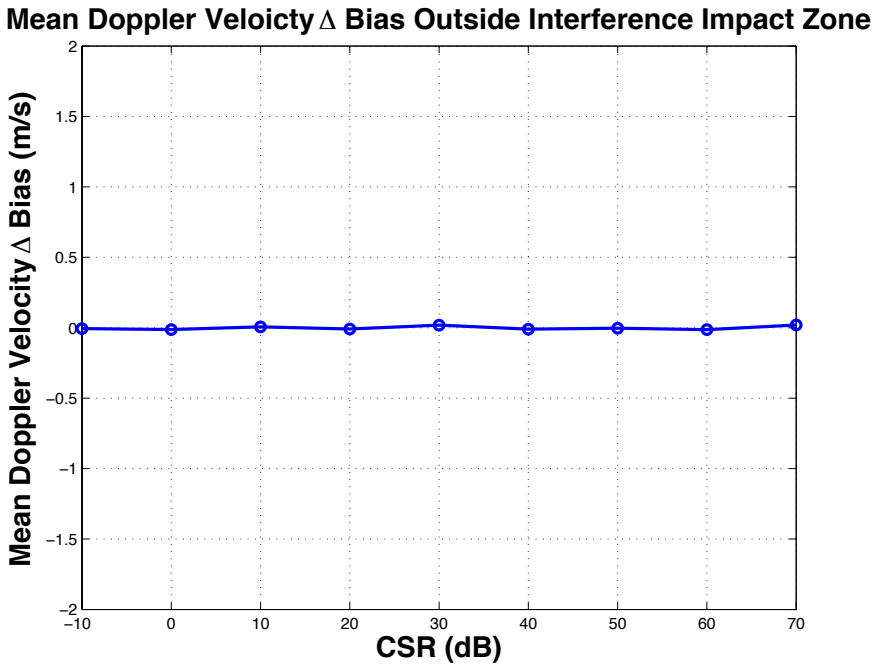

Figure 4.20: Same as Figure 4.19, except for Doppler velocity.

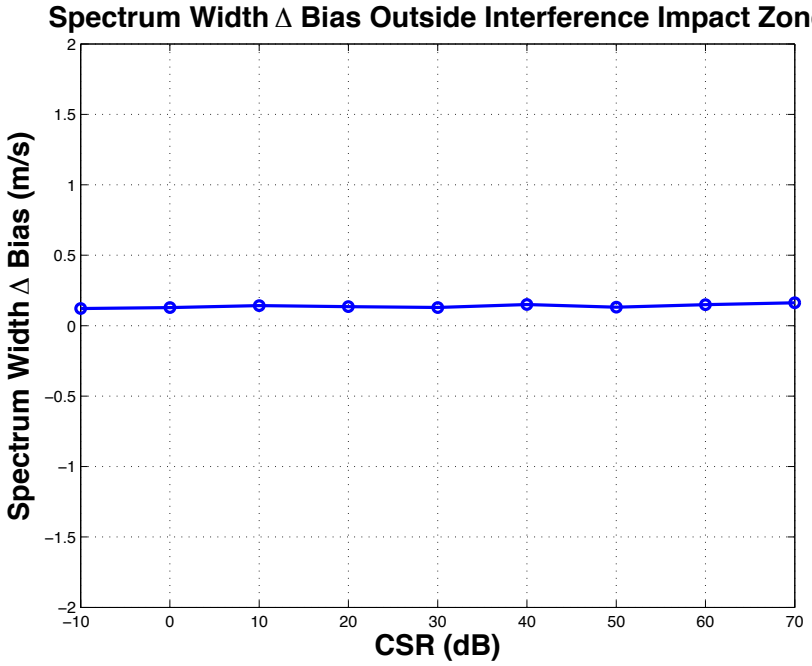

Figure 4.21: Same as Figure 4.19, except for spectrum width.

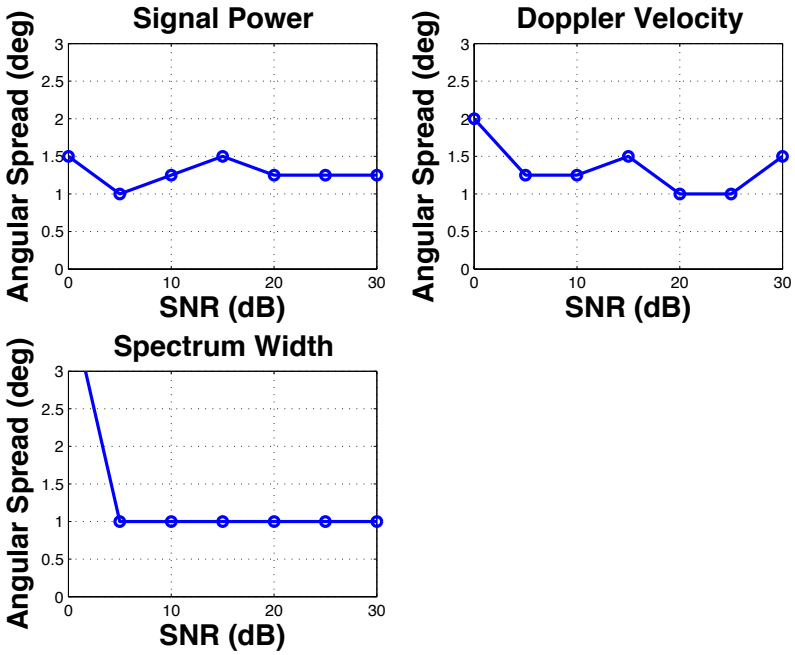

Figure 4.22: Angular spread of interference signal for different SNRs. As expected, the performance of the algorithm is stable across the range of SNRs tested and shows no significant deterioration except at 0-dB SNR. The large increase in the spread of interference is likely due to estimation errors that are caused by the low SNR in the directions near the interference signals.

results, the remainder of the simulations are conducted with an SNR of 20 dB unless otherwise noted.

In the ideal scenario, where a single transmit beam can illuminate the entire volume of interest, the location of the interference with respect to the center of the transmit beam would not impact the performance of the algorithm significantly. However, with the constraints of a real system where the volumes of interest are illuminated sequentially with successive spoiled transmit beams, the location of the interference signal within a transmit beam could impact the

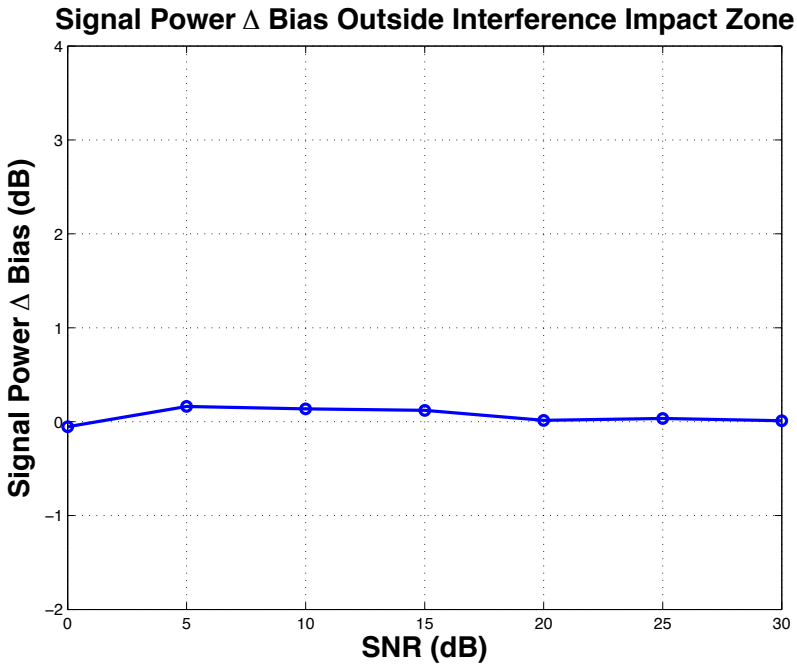

Figure 4.23: Signal-power delta biases away from the interference source for different SNRs. The small biases indicate that the adaptive algorithm is not sensitive to the SNR of the weather signals, and the algorithm does not introduce additional biases in weather-only situation. The results for mean Doppler velocity and spectrum width show similar independence on SNR.

performance of the algorithm. Using Figure 4.4 as an example, it is possible for an interference signal located in the direction of $Rx_{1,2}$ to contaminate the estimates of beams $Rx_{3,1}$, $Rx_{4,1}$, and $Rx_{5,1}$ through the sidelobes. When the algorithm tries to estimate the signal power in the direction of $Rx_{5,1}$, it will use $Rx_{3,1}$, $Rx_{4,1}$, $Rx_{5,1}$, $Rx_{1,2}$, and $Rx_{2,2}$ as the set of initial beams. Within this set of initial beams, the optimal side beam to use to cancel the interference signal should be beam $Rx_{1,2}$ because it is directly pointed at the interference source. However, due to the time delay between successive transmit beams, it is possible that the output of $Rx_{1,2}$ is uncorrelated with the output of $Rx_{5,1}$,

especially if the spectrum width of the interference signal is wide. In such a scenario, beams $Rx_{1,2}$ and $Rx_{2,2}$ will not pass the correlation threshold test and will not be selected as the appropriate side beams for interference cancellation, and only $Rx_{3,1}$ and $Rx_{4,1}$ will be used. Since the interference signal can only contaminate $Rx_{3,1}$, $Rx_{4,1}$, and $Rx_{5,1}$ through the sidelobes, that places an upper and lower bound on the CSRs that would impact the algorithm the most. If the interference is weak, the sidelobes of the initial beams can provide enough rejection to mitigate the contamination, and if the interference is extremely strong, it will contaminate $Rx_{3,1}$ and $Rx_{4,1}$ enough such that those two side beams can be used successfully to cancel the interference in $Rx_{5,1}$. The most challenging case is when the interference is strong enough to contaminate $Rx_{5,1}$ but not strong enough to overcome the sidelobe attenuation for $Rx_{4,1}$. Based on Figure 4.12, the sidelobe levels of the initial beams 1° and 2° away from the pointing direction are -31 dB and -48 dB, respectively. Based on these discussions, a white-noise signal with a CSR of -40 dB was chosen to test the adaptive algorithm, and the location of the interference source was shifted from -5° to 5° in 1° increments. The transmit beam locations are fixed and centered at -5°, 0°, and 5°. Therefore, the interference source located at -3°, -2°, 2°, and 3° would be at the edge of a transmit beam. Figure 4.24 shows the angular spread of interference as a function of its location, and it is clear

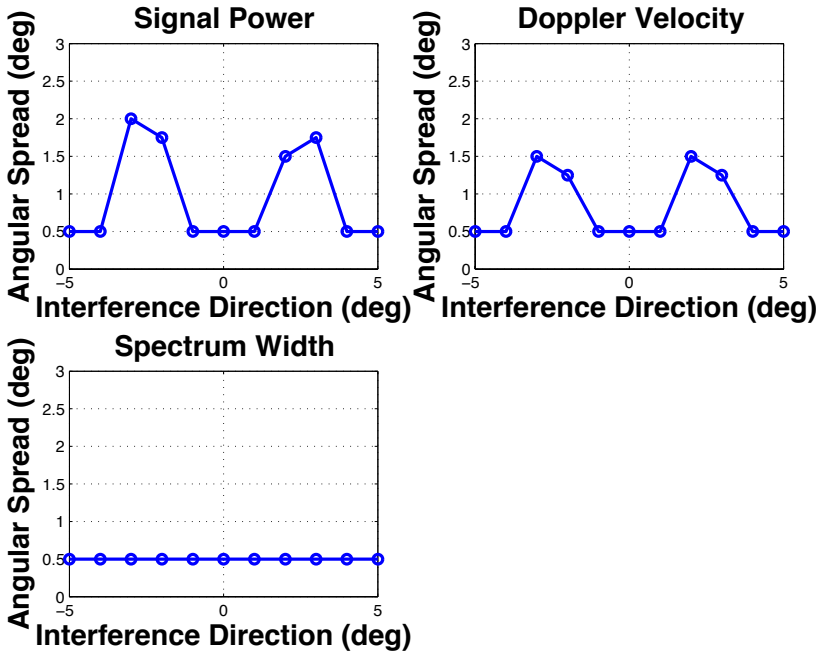

Figure 4.24: Angular spread of a white-noise interference signal with a 40-dB CSR as its location is shifted from -5° to 5°. The performance of the adaptive algorithm clearly degrades when the interference is located near the edge of a transmit beam (-3°, -2°, 2°, and 3°). This is due to the time-lag between the successive transmit beams causing the interference signal in the initial beams to be uncorrelated. Despite the degradation in performance, a PAR using the adaptive beamspace algorithm still produced an angular spread smaller than that of a dish-antenna system (3°, as shown in Figure 4.18).

that the interference signal being on the edge of the transmit beam has a significant effect on the performance of the algorithm. The angular spread increased from 0.5° when the interference is located near the center of the transmit beam to greater than 1.5° when it is located at the edge of the transmit beam. However, even in this worst-case scenario, a PAR using the adaptive beamspace algorithm still produced an angular spread smaller than that of a dish-antenna system (3°, as shown in Figure 4.18). Figure 4.25 shows the performance of

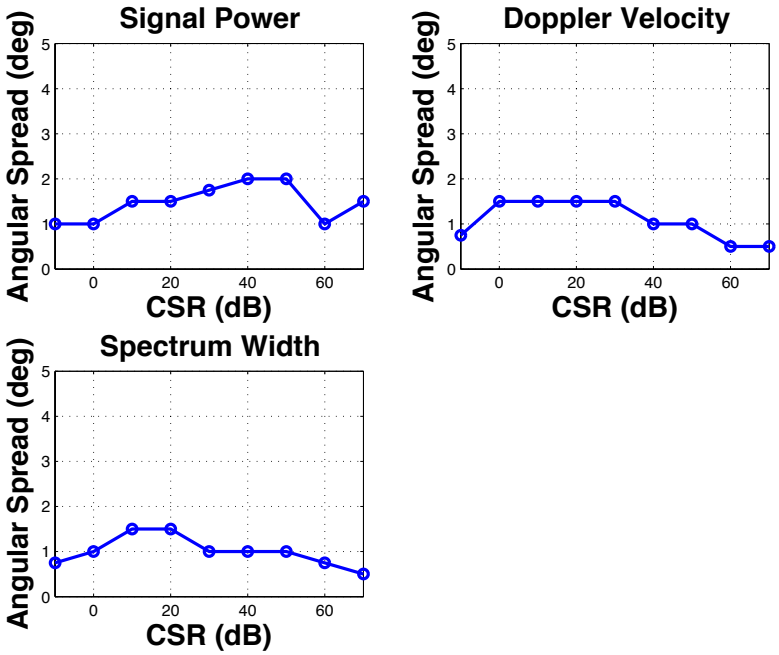

Figure 4.25: Same as Figure 4.18, except the interference signal is located at the edge of the transmit beam to test the worst-case scenario for the adaptive beamspace algorithm.

the adaptive algorithm when the CSR of the white-noise signal located at the edge of a transmit beam is varied from -10 to 70 dB in 10-dB increments. The worst performance is for CSRs between 30 to 50 dB as expected, and the angular spread of the interference signal never exceeded 2° for all CSRs tested in the worst-case scenario. These results support the conclusion that, in terms of reducing the angular spread of point interference signals, a PAR using the adaptive beamspace algorithm is superior to a low-sidelobe dish-antenna system.

4.3.3.3 Reflectivity Gradients

Beyond mitigating interference and clutter signals, a PAR using the adaptive beamspace algorithm must also be able to match a dish-antenna system in terms of handling reflectivity gradients despite having higher two-way side-lobe levels. The important parameters that must be varied to evaluate the ability of the adaptive beamspace algorithm to handle reflectivity gradients are the step size of the reflectivity profile, the spatial extent of the gradient, and the location of the maximum gradient with respect to the transmit beam and with respect to broadside of the array. The first set of simulations seeks to evaluate the performance of the algorithm for profiles with maximum gradients located at 0°, 20°and 40° with respect to broadside of the array. The location of the maximum gradient with respect to broadside of the array was chosen such that the maximum gradient is located at broadside, at the center of the scanning range, and at the edge of the scanning range to provide a full evaluation of the algorithm. The simulated profiles have a change in SNR that ranged from 10 to 70 dB in 20-dB increments, and the spatial extent of the gradient is 2°. Figure 4.26 shows examples of profiles with 50-dB step size used in these simulations. Figure 4.27 shows the mean biases in signal-power estimates from directions that are at least 5° away from the center of the gradients. A 5° buffer was chosen to eliminate the directions with biases that are due to the gradient,

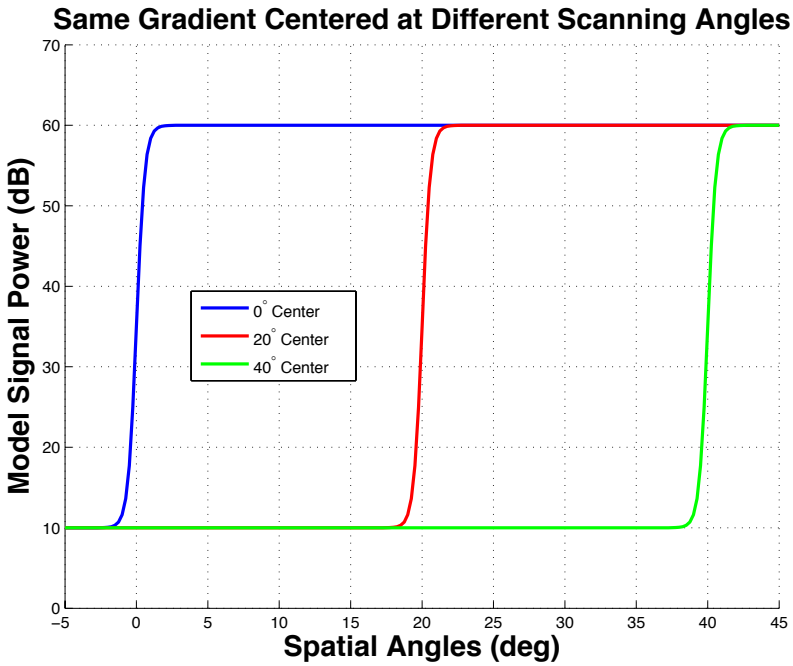

Figure 4.26: Simulated reflectivity profiles with maximum gradient located at 0°, 20°, and 40° with respect to broadside of the array. These profiles have a 50-dB change in SNR spread over 2°. Due to the beam broadening effect of phased-array systems, the same gradient appearing at different locations could result in different performance for the adaptive algorithm. The three maximum gradient locations were chosen to evaluate the algorithm's performance when the maximum gradient is located at broadside, at center of scanning range, and at edge of scanning range.

which is measured using the zone of impact described before. For all scenarios, the mean biases are close to zero, which indicates that the algorithm did not introduce additional biases as expected. The results for mean radial velocity and spectrum width are similar to those of signal-power and are not shown. Figures 4.28 and 4.29 show the zone of impact for a PAR using the adaptive

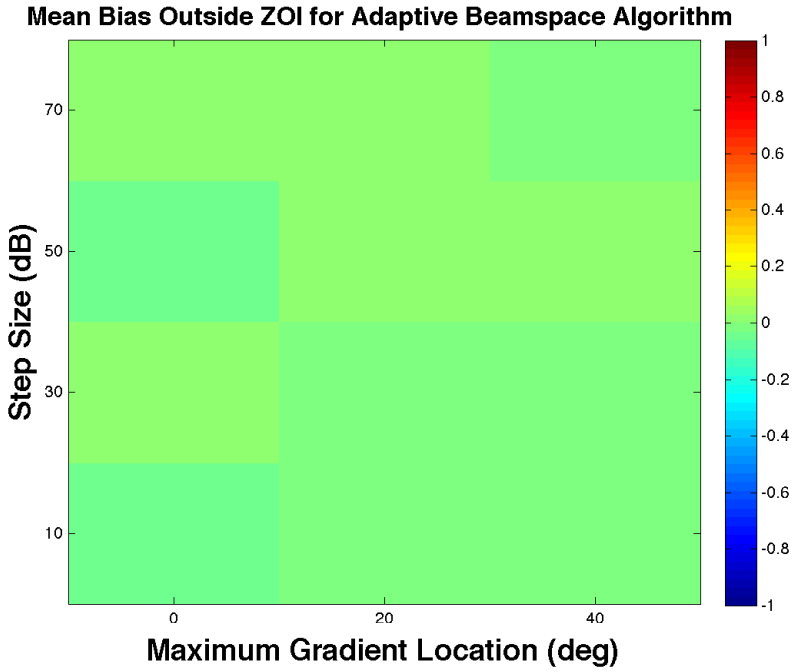

Figure 4.27: Mean biases in signal-power estimates from directions at least 5° away from the location of the maximum gradient. The algorithm performed as expected in these weather-only situations producing estimates with near-zero biases for all scenarios. The results for mean Doppler velocity and spectrum width are similar but not shown.

beamspace algorithm and a dish-antenna system, respectively. The x-axis indicates where the maximum gradient is located with respect to the broadside of the array, the y-axis indicates the step size of the gradient, and the color scale indicates the zone of impact of the gradient measured in degrees. It is clear that for small gradients (10-dB step size), a PAR using the adaptive beamspace algorithm and a dish-antenna system can accurately estimate the signal power leading to 0° with large biases regardless where the maximum gradient is located. For very large gradients (70-dB step size), a PAR using the adaptive beamspace algorithm performs worse than a dish-antenna system regardless

of where the gradient is located, and the zone of impact is constant. The constant zone of impact indicates that it is the result of contamination through the sidelobe since the narrower main lobe at broadside did not lead to improved performance. For 30 and 50 dB steps, the zone of impact gets smaller as the the gradient shifts toward the broadside of the array, which is a direct result of the narrowing of the main lobe while the contamination through the sidelobes is limited. Comparing the results of a PAR using the adaptive beamspace algorithm to a dish-antenna system shows similar performance near the edge of the scanning range for reflectivity profiles with up to 50-dB changes in SNR, which is expected since the phased-array system was simulated to have the same beamwidth as a dish antenna system when scanned to $\pm 45^{\circ}$.

Similar to the point interference case, the location of the maximum gradient with respect to the transmit beam could also impact the performance of the algorithm since profiles located at different locations within the transmit beam will have different parts of the profile illuminated at once. Using Figure 4.4 as an illustration, if the maximum gradient is located in the direction of $\mathrm{Rx}_{1,2}$, the side of the profile with low signal-power (low side) would be in the directions of $\mathrm{Rx}_{1,1}$ to $\mathrm{Rx}_{5,1}$. The contamination to these beams due to the side of the profile with high signal-power (high side) would be greatly reduced since Tx_1 did not illuminate those directions. These conditions suggest improved performance in estimating the signal-power of the low side of the profile. A similar

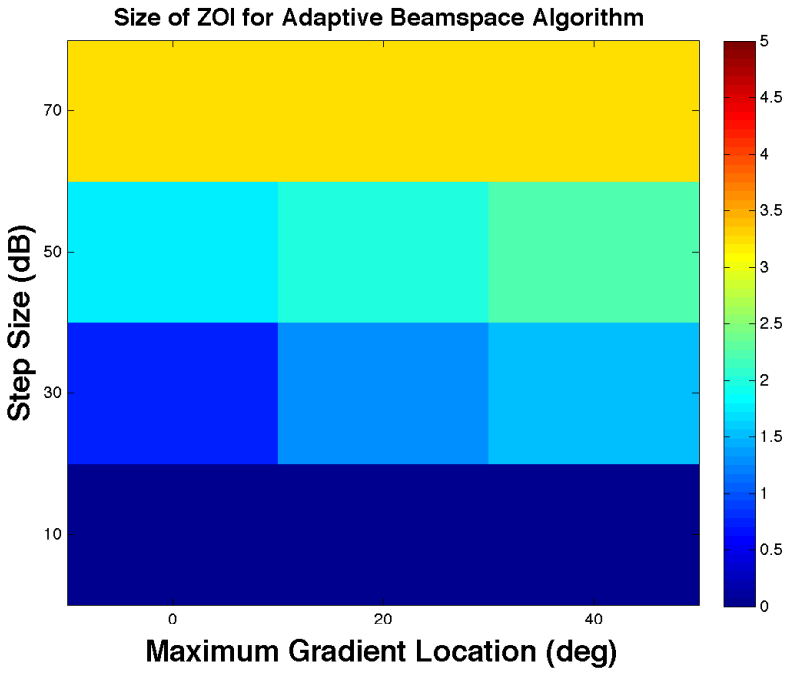

Figure 4.28: Zone of impact for reflectivity profiles with different step sizes and maximum gradient located at 0°, 20°and 40°. For a profile with a 10-dB step size, the algorithm can accurately estimate the signal power with no angles with biases exceeding 1 dB. For profiles with 30 and 50-dB step sizes, the narrower mainlobe leads to improved performance as gradients shift toward the broadside of the array. For profile with 70-dB step size, the contamination through sidelobes is strong and overpowers improvements from a narrower main lobe.

argument can be made for cases where the maximum gradient is located in the direction of $Rx_{5,2}$ in Figure 4.4. In this case, Tx_2 does not illuminate the high side of the profile, and estimating the low side of the profile becomes easier. When the maximum gradient is located at the center of the transmit beam (e.g., $Rx_{3,1}$), both side of the profile are illuminated by a single transmit beam, and the initial beams pointed toward the low side are most likely to be

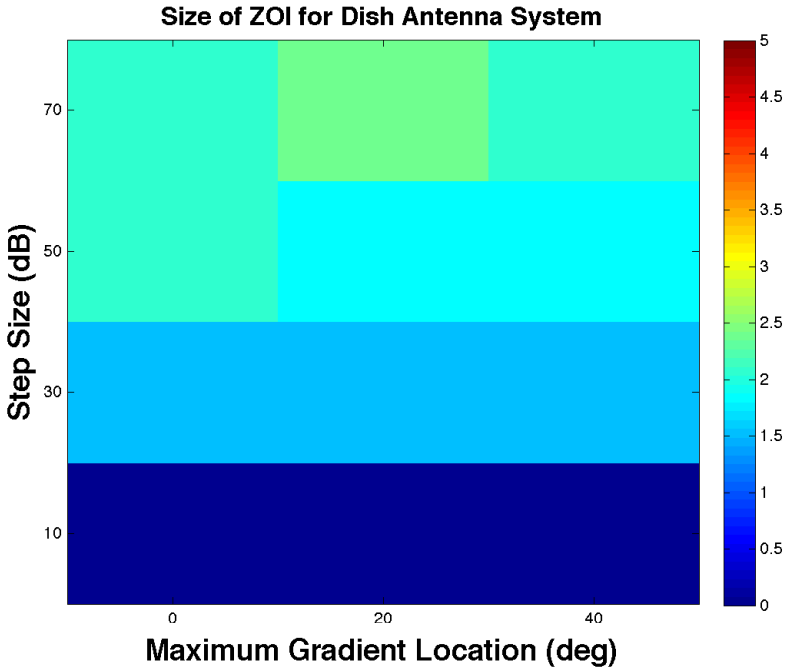

Figure 4.29: Same as Figure 4.28, except for dish-antenna system. Since the beamwidth of a dish-antenna is constant, the location of the gradients did not significantly impact the performance.

contaminated by the high side of the gradient. In this set of simulations, the spoiled transmit beam is centered at 25°, and profiles with step sizes of 30, 50, and 70 dB were placed at 23°, 25°, and 27°. These configurations correspond to maximum gradients located by the left edge, center, and right edge of the transmit beam. Figure 4.30 shows the zone of impact for the different profile step sizes and maximum gradient locations. The x-axis indicates where the maximum gradient is located, the y-axis indicates the step size of the gradient, and the color scale indicates the zone of impact of the gradient measured in degrees. For profiles with 30 and 50-dB step sizes, the location of the maximum gradient within the transmit beam does not produce any significant impact on

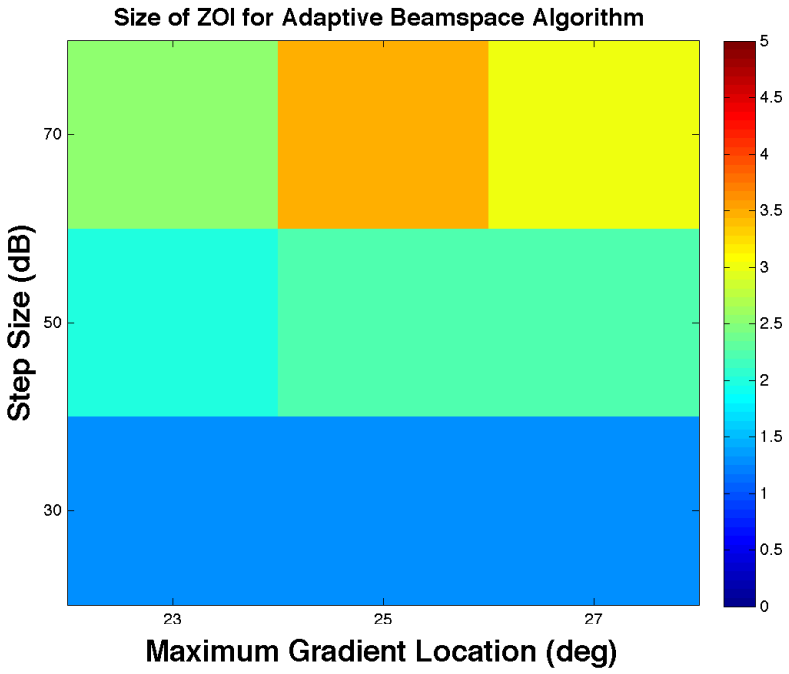

Figure 4.30: Zone of impact for gradients with different step sizes located at 23°, 25°, and 27°. Since the transmit beam is centered at 25°, the three maximum gradient locations evaluate the adaptive algorithm for cases where the maximum gradient is located by the left edge, center, and right edge of the transmit beam. The worst performance occurs for a profile with a large (70-dB) step size and the maximum gradient is located at the center of the transmit beam because in such scenarios, both the low and high side of the profile are illuminated simultaneously. When the maximum gradients are located at the edge of the transmit beam, the high side of the profiles not being illumined simultaneously with the low side helps the algorithm produce more accurate signal-power estimates on the low side of the profiles and reduces the zone of impact.

the performance since the sidelobe levels of the initial beams in conjunction with the adaptive step can successfully attenuate the high side of the gradients to minimize the contamination. For a profile with a 70-dB step size, the

location of the maximum gradient produces a noticeable difference in performance. As expected, when the gradient is located at the center of the transmit beam, the adaptive algorithm performed the worst, and when the gradient is located near the edge of the transmit beams, the adaptive algorithm performed better due to the transmit beam being helpful in attenuating the high side of the gradient. Having established that the worst performance occurs when the maximum gradient is located near the center of the transmit beam, the rest of the simulations place the maximum gradients in the center of the transmit beam to show the worst-case results.

The last set of simulations evaluates the algorithm with different types of gradients. Figure 4.31 shows a family of profiles with step sizes from 10 to 70 dB with maximum gradient located at 25° and having spatial extent of 2°. In these simulations, the spatial extent of the gradients, delimited by the vertical black dashed line in Figure 4.31, is defined as the angular region where the signal-power is greater than the constant signal-power on the low side by 1 dB but less than the constant signal-power on the high side by 1 dB. With a constant spatial extent, a larger step size implies larger gradients. Figure 4.32 shows gradients with the same step size but different spatial extents. By spreading the change in signal power over a larger spatial extent, the profiles with larger spatial extent have less steep slopes. In the last set of simulations, the step size of the profile was varied from 10 to 70 dB in 10-dB increments,

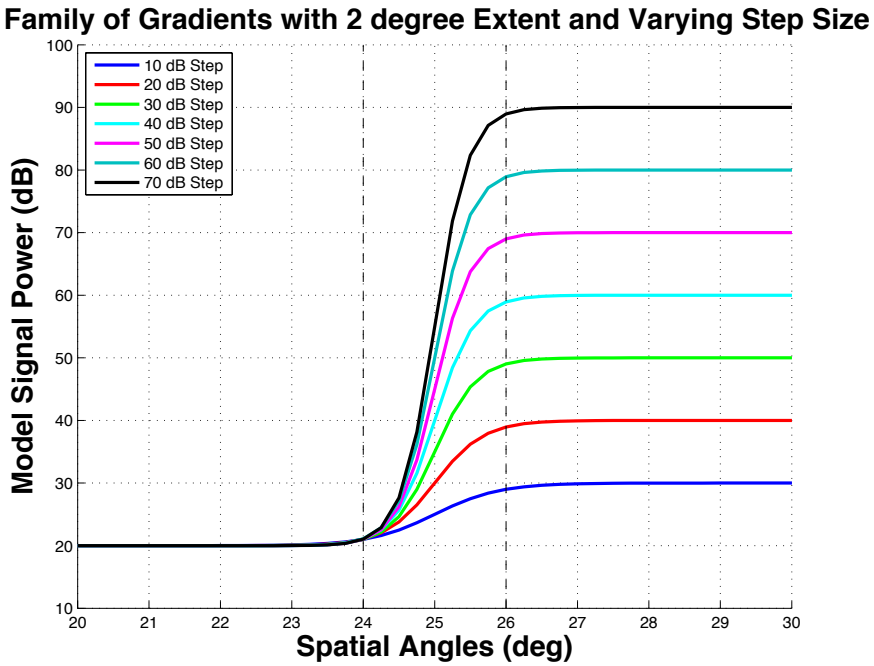

Figure 4.31: Family of profiles with varying step size but same 2° spatial extent. The vertical black dashed line delimits the spatial extent of the gradient, which is defined as the angular region where the signal power is greater than the signal power on the low side by 1 dB and less than the signal power on the high side by 1 dB. For gradients with the same spatial extent, a larger step size implies a steeper transition, which is more challenging to the adaptive algorithm.

and the spatial extent was varied from 1° to 5° in 1° increments to generate a variety of gradients to fully evaluate the adaptive algorithm. Figures 4.33 and 4.34 show the zone of impact in signal-power estimates for a PAR using the adaptive beamspace algorithm and a dish-antenna system, respectively, where the x-axis is the spatial extent of the gradient, the y-axis is the step size of the gradient, and the color scale is the zone of impact measured in degrees. Comparisons between Figures 4.33 and 4.34 show that for profiles with step sizes

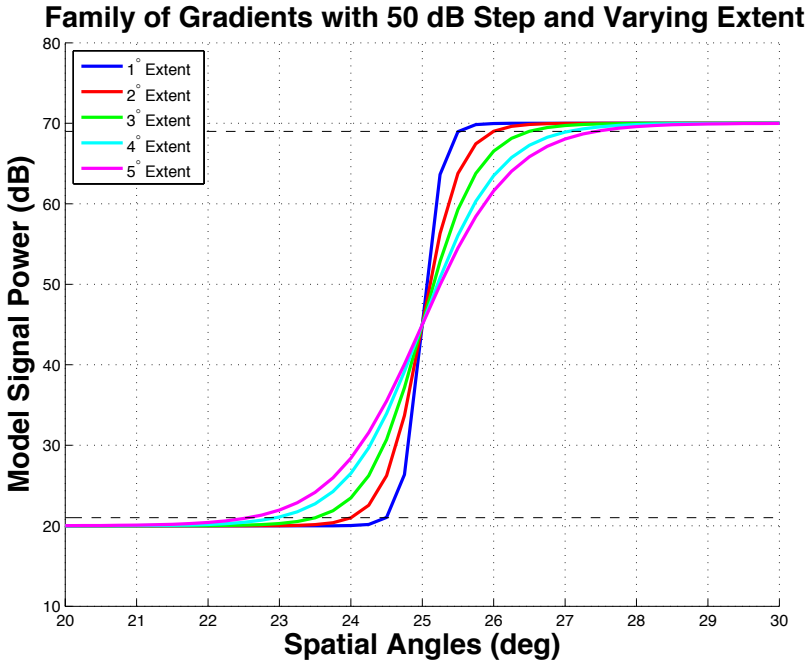

Figure 4.32: Family of profiles with varying spatial extent but same 50-dB step size. The horizontal black dashed line delimits the 1-dB threshold used to determine the spatial extent of a gradient. For profiles with the same step size, a smaller spatial extent implies a steeper transition, which is more challenging to the adaptive algorithm.

less than 60 dB, a PAR using the adaptive beamspace algorithm has a smaller zone of impact for all spatial extents, and for profiles with a 60-dB step size, the performance of a PAR using the adaptive beamspace algorithm is similar to that of a dish antenna system for 4°and 5° spatial extents and worse than that of the dish-antenna system for 1°, 2°, and 3° spatial extents. For profiles with a 70-dB step size, a PAR using the adaptive beamspace algorithm performs worse than a dish-antenna system. This clear distinction is due to the inability of the adaptive algorithm to push the sidelobe down far enough in the cases with large step sizes. Figure 4.35 shows a beam pattern pointed at the

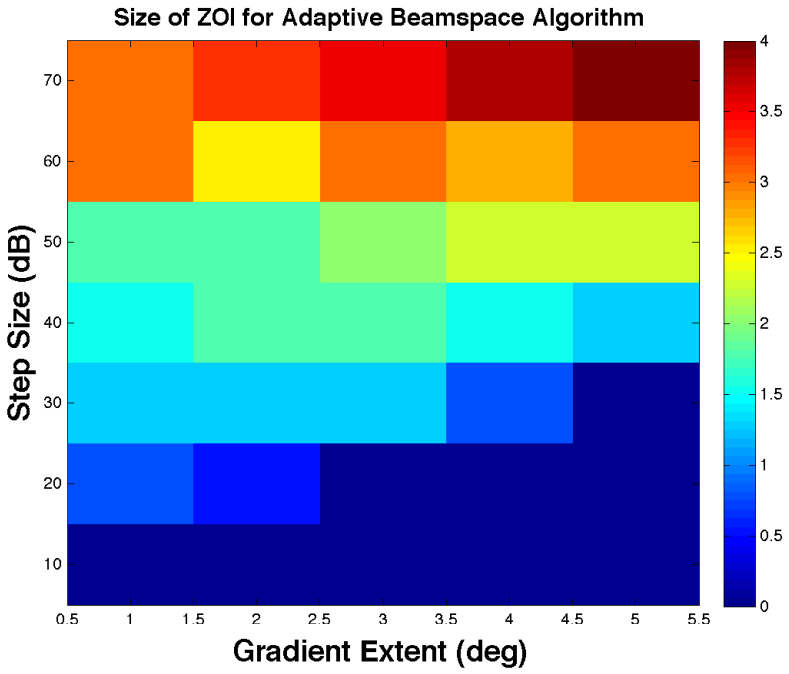

Figure 4.33: Zone of impact for different profiles with varying step size and spatial extent for a PAR using the adaptive beamspace algorithm. The x-axis indicates the varying spatial extent of the gradients from 1° to 5° in 1° increments, the y-axis indicates the varying step size from 10 to 70 dB in 10-dB increments, and the color scale indicates the zone of impact measured in degrees. A PAR using the adaptive beamspace algorithm matches or exceeds the performance of a dish-antenna system for profiles with step sizes of up to 50 dB, and the performance of a PAR using the adaptive beamspace algorithm degrades significantly for profiles with step sizes of 60 or 70 dB.

same direction for profiles with different step sizes and a 1° spatial extent. The dark black line in each plot indicates the required sidelobe envelope to minimize the contamination from the high side to the low side. For example, in the 30-dB step plot, the maximum gradient is located at 40° and transitions from 20 to 50 dB from 39.5° to 40.5°. Since the beam in the example is steered to 38.5°, to accurately estimate the signal power, the beam pattern needs to

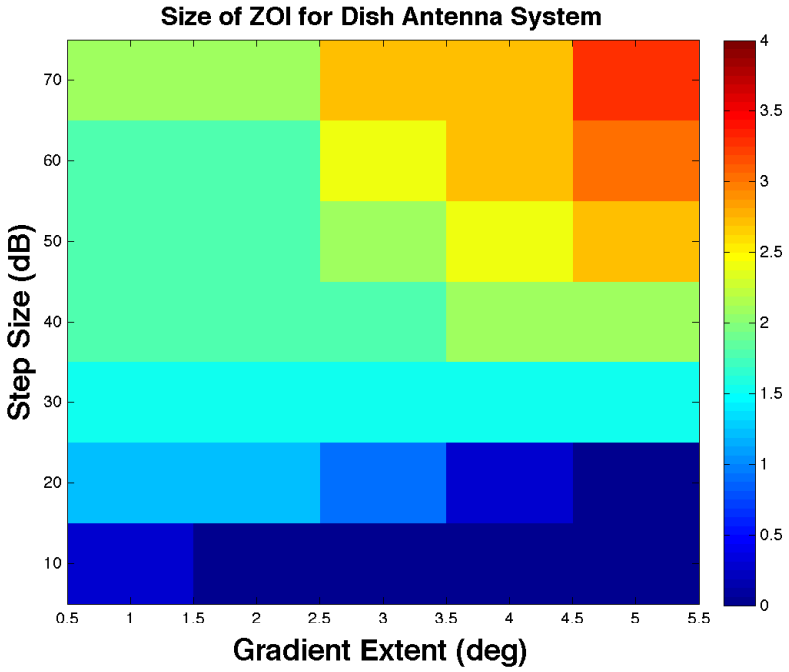

Figure 4.34: Same as Figure 4.33 except for a dish-antenna system. The performance degrades for profiles with larger step sizes as expected.

have sidelobe levels transition from 0 dB at 39.5° to -30 dB at 40.5° and stay below -30 dB for angles greater than 40.5°. It is clear that the adaptive beam pattern achieves this desired sidelobe envelope and the signal power estimates at 38.5° should not be impacted by the presence of the gradient at 40° in this case. The same argument applies to the other profiles, and it is clear that for profiles with step sizes of 60 or 70 dB the adaptive algorithm could no longer push the sidelobe levels to achieve the desired envelope. In the 70-dB step size case, the second sidelobe located at 40.5° is only -40 dB instead of the desired -70 dB, which resulted in large biases in the signal-power estimates at the steering angle. By comparing the beam patterns, it is clear that the adaptive

step of the adaptive beamspace algorithm can automatically adjust the sidelobe levels to mitigate contamination in the presence of reflectivity gradients. For small gradients, the algorithm successfully allows for higher sidelobe levels that would not result in biased estimates, the trade-off for higher sidelobe levels is a slightly narrower main beam compared that of the initial beams. The peak sidelobe level for spatial angles less than 38.5° is approximately -20 dB, which is expected based on the weight constraint on the side beams not used for signal cancellation. Since the adaptive algorithm failed with profiles with large step sizes and small spatial extents, it is important to characterize how likely are these failures to occur. In the physical world, reflectivity gradients occur over distance and are measured in dB per kilometer. The simulated gradients can be converted to physical units by taking into account the distance from the radar, and Table 4.4 shows the equivalent gradient in dB per kilometer for different ranges. Using available statistics of reflectivity gradients in Torlaschi and Humphries (1983), the frequency of occurrence of such gradients are estimated (using Figure 1 in Torlaschi and Humphries (1983)) and presented in Table 4.5, where a number like 10^{-4} can be interpreted as one in 10000 cases. These estimates are not perfect since they only use the slope of the gradient. A profile with a step size of 30 dB and a spatial extent of 2° produces a similar slope as a profile with a 70-dB step size and a 5° spatial extent. However, the adaptive algorithm performs much better in the first case

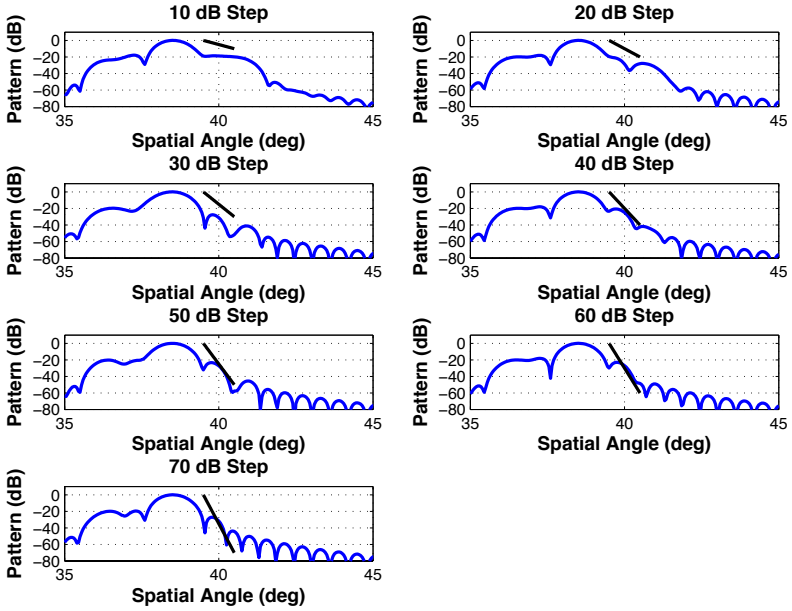

Figure 4.35: Adaptive beam patterns steered to 38.5° for profiles with maximum gradient located at 40° with varying step sizes and a 1° spatial extent. The dark black line in each plot indicates the required sidelobe envelope to attenuate the gradient. As the step size of the gradient increases, the adaptive algorithm lowers the sidelobe levels to achieve the desired sidelobe envelope until the step size reaches 60 dB. For 60 or 70 dB step sizes, the adaptive algorithm could no longer achieve the desired envelope, resulting in large biases in the signal-power estimates at the pointing direction.

Table 4.4: Conversion between simulated gradients to equivalent gradients measured in dB km^{-1} at different distances from the radar

Distance from Radar (km)	**60 dB over 1°**	**60 dB over 3°**	**70 dB over 5°**
30	114.6	38.2	26.7
50	68.8	22.9	16.0
100	34.4	11.5	8.0
150	22.9	7.6	5.3

than in the second case. At a range of 150 km, it is more plausible that the gradient extends over a distance of 5.2 km (2°) than 13 km (5°) since the beam

Table 4.5: Frequency of occurrence for different gradients

Distance from Radar (km)	**60 dB over 1°**	**60 dB over 3°**	**70 dB over 5°**
30	$\ll 10^{-4}$	$\ll 10^{-4}$	$\approx 10^{-3.5}$
50	$\ll 10^{-4}$	$< 10^{-4}$	$\approx 10^{-3.5}$
100	$\ll 10^{-4}$	$\approx 10^{-3.5}$	$\approx 10^{-2.5}$
150	$\ll 10^{-4}$	$\approx 10^{-4}$	$\approx 10^{-2.5}$

is illuminating the upper part of the storm structure. Therefore, the worst performance of a PAR using the adaptive beamspace algorithm for profiles with a 70-dB step size and a spatial extent of 5° is even less likely to occur than the estimation in Table 4.5 and should not be a significant concern. Also, the zone of impact degradation compared to a dish-antenna system is only about 0.5° for such cases. The worst degradation in performance compared to a dish-antenna system occurs for profiles with 60- or 70-dB step sizes and a 1° spatial extent, but such cases are much less likely to occur.

In summary, the simulations showed that a PAR using the adaptive beamspace algorithm can match or exceed the performance of a low-sidelobe dish-antenna system in terms of limiting the directions where the signal-power estimates are significantly biased due to the presence of a gradient for step sizes up to 50 dB. For gradients with larger step sizes, the adaptive algorithm performs worse when the spatial extent of the gradient is small. However, such cases are the least likely to occur with a frequency distribution of much lower than one in 10,000 regardless of range. For the more likely cases with large step

sizes and large spatial extents, the performance degradation compared to a dish-antenna system is small. Having completed a thorough evaluation via simulations, the next section presents limited results with real data collected using the Atmospheric Imaging Radar (AIR)(Isom et al. 2013).

4.4 Real Data Analysis

As shown in the previous section via simulations, the proposed adaptive beamsapce algorithm can produce accurate and calibrated estimates of the radar variables while automatically rejecting interference signals. However, the time-series simulator was simplistic and several assumptions about the array were required. It is important to test the algorithm with real data collected in the field to ensure it can still function when some of the assumptions in the simulator may be violated. An ideal instrument to collect data to evaluate adaptive beamspace processing is the University of Oklahoma's Atmospheric Imaging Radar (AIR) (Isom et al. 2013; Kurdzo et al. 2017). The AIR is a mobile X-band weather radar that transmits a 20° vertical fan beam and utilizes a ULA consisting of 36 receiving elements. On 16 May 2015, the AIR was used to collect data on a strong tornadic supercell near Tipton, OK. The signal-power estimates are shown in Figure 4.36. The left-side panels show the signal-power estimates from Fourier beamforming with a von Hann taper at 0° and 3° elevation angles, and the right-side panels show the signal-power

estimates from adaptive beamspace algorithm at the same elevations. Due to the fan shaped transmit beam, ground clutter can contaminate estimates of higher elevations if not properly rejected. As shown in Figure 4.36, ground clutter near the radar can be clearly seen in the windowed Fourier result at 0°, and even at 3° elevation, there is still visible ground clutter residue. For the adaptive beamspace algorithm, there is little ground clutter contamination visible in both 0° and 3° elevations. This small amount of ground clutter in the 0° elevation plots is not surprising since it is unlikely that most ground clutter targets are located exactly at 0° elevation. With adaptive beamforming, even if the clutter is located at 0.5° elevation, it will be severely attenuated when estimating the signal power at 0°. These results agree with the simulations showing that adaptive beamspace algorithm can successfully mitigate contamination from interference and clutter.

In the original data set, there is extensive ground clutter contamination near the radar, and the storm is located approximately 21 km away from the radar. To better evaluate the adaptive beamspace algorithm's ability to estimate meteorological variables, the I/Q weather signal was shifted in range and coherently summed to overlap with the ground clutter signal located near the radar. The results of adaptive beamspace algorithm and windowed Fourier beamforming are shown in Fig. 4.37. The two plan-position indicator (PPI)

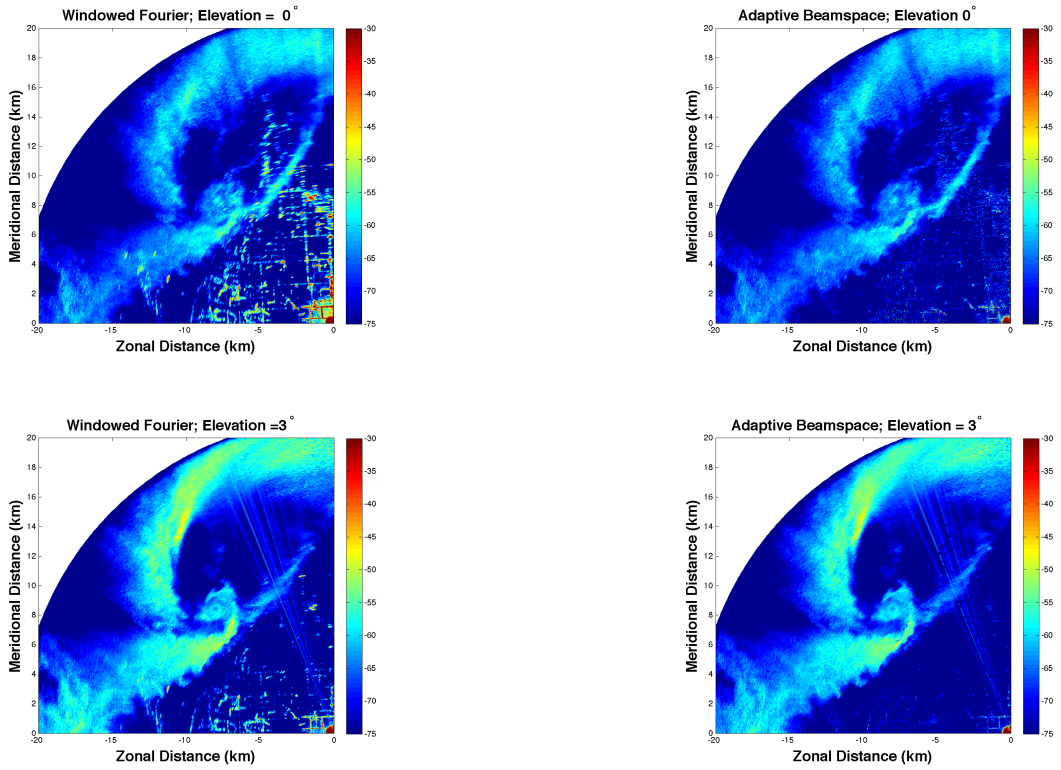

Figure 4.36: PPI fields corresponding to adaptive beamspace processing and windowed Fourier beamforming on data collected with the AIR on 16 May 2015 near Tipton OK. The PPI plots show the received signal power at 0° (top panels) and 3° elevation (bottom panels). For the windowed Fourier method (left panels), ground clutter at lower elevations contaminated signal-power estimates at higher elevations. With the adaptive beamspace algorithm (right panels), there is minimal ground clutter contamination in both elevations. These results agree with simulations showing that the adaptive beamspace algorithm can limit the spread of interference signals.

plots show the received signal power at 3° elevation, and despite the aggressive window used in the windowed Fourier beamforming to reduce the side-lobe levels of the receive beam, it is clear that ground clutter still contaminated

the weather signal-power estimates when they overlapped. In contrast, adaptive beamspace algorithm successfully rejected the ground clutter signal for the majority of the cases. There are some remnants of the ground clutter signal, but they are much weaker and have minimal impact on estimates of the weather signal power. The range-height indicator (RHI) plots are along the radial indicated by the white line in the PPI images. The RHI images clearly show that adaptive beamspace processing successfully rejected a ground clutter target located around 1 km, 1.5 km, and 2 km in range for higher elevations. Qualitatively, the weather signal-power estimates are similar between the two methods as expected from the simulation results. This example demonstrates that adaptive beamspace processing can function with a real system with non-ideal components, and the degradation in performance is not qualitatively apparent.

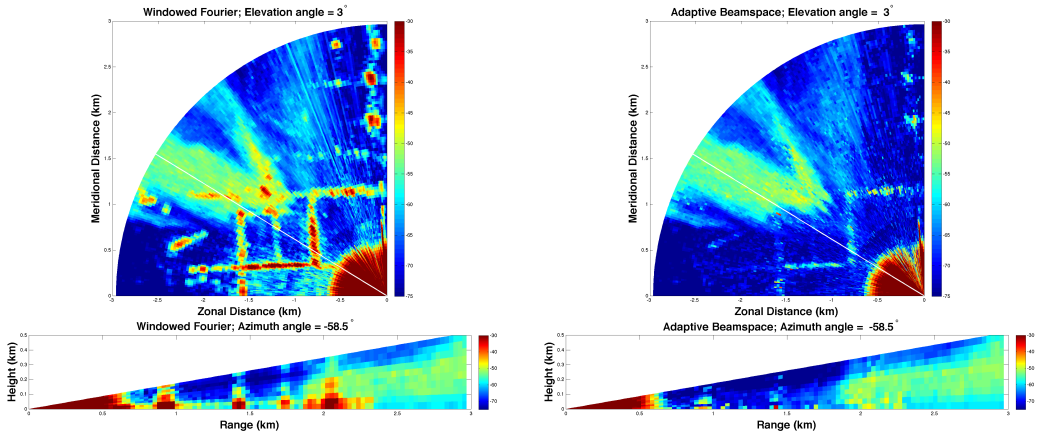

Figure 4.37: PPI and RHI fields corresponding to adaptive beamspace processing and windowed Fourier beamforming on data collected with the AIR on 16 May 2015 near Tipton OK. The PPI plots show the received signal power at 3° elevation, and the white line in the PPI plots indicates the azimuthal angle of the RHI plots. It can be clearly seen that the adaptive beamspace algorithm (right panel) successfully rejected the majority of the ground clutter signal that originated from lower elevation angles, and it performed much better than windowed Fourier beamforming (left panel). Moreover, it can be seen that estimates of received signal power are similar between the two methods.

Chapter 5

Comparison of Alternatives

The motivation for developing the adaptive beamspace algorithm is to utilize adaptive beamforming to form simultaneous receive beams so that timeline and data quality requirements for an MPAR system can be met. As discussed in Chapter 1, there are multiple approaches to generate the required simultaneous receive beams, and each approach has its own advantages and disadvantages. This chapter presents a preliminary comparison between some of the possible approaches to show that the adaptive beamspace algorithm used in conjunction with a spoiled transmit beam is a feasible solution.

5.1 System Simulations

There are many possible MPAR configurations that can meet the functional requirements. It is important to compare these different configurations with a solution that utilizes the adaptive beamspace algorithm to understand the advantages and disadvantages of each configuration. As discussed in Chapter 1, there are at least four different approaches that have been proposed in literature that can meet the MPAR requirements. The multiple frequency (Weber

et al. 2007) and time multiplexing (Melnikov et al. 2015) approaches are not studied further in this work since they do not involve beamforming and can be used in conjunction with any beamforming approach. This chapter will focus on three configurations: 1) a split transmit beam approach, 2) a spoiled transmit beam with non-adaptive receive beams, and 3) a spoiled transmit beam with receive beams formed with the adaptive beamspace algorithm. The functional requirements for an MPAR system listed in Table 5.1 (FAA 2013) drove a simplified design process for systems that utilize these configuations.

The two-way sidelobe requirements for nonadaptive beams are (FAA 2013): 1) a first sidelobe at -54 dB, 2) sidelobes between 2° and 10° below a straight line connecting -54 dB at 2° and -68 dB at 10°, and 3) sidelobes $\leq$-80 dB for angles greater than 10°. These stringent sidelobe requirements pose a significant challenge in antenna design and beamforming for MPAR systems.

The update time requirement leads to the use of simultaneous receive beams. That is, if current WSR-88D VCPs and dwell times are kept on an MPAR system, then a four-face MPAR system can automatically reduce the volumetric update time by a factor of four (Zrnić et al. 2015). Reducing the current update time of four to five minutes by a factor of four results in an update time slightly longer than the required 60 seconds. However, since an MPAR system must also allocate time for aircraft surveillance functions, the weather surveillance

must be completed in a time that is much shorter than 60 seconds to effectively achieve the desired update time. Based on dwell-time calculations done in Zrnić et al. (2015), three simultaneous receive beams per face are needed to successfully meet the update time requirement for weather surveillance in a multifunction context. Since the four faces of an MPAR system can be assumed to be identical, the design and analysis in this chapter will focus on one face of an MPAR system. With the desired number of simultaneous receive beams fixed, the remainder of the simple system design involves choosing the appropriate number of radiating elements, the transmit power per element, and the tapering required for each system. The tapering, especially tapering on receive, controls the two-way sidelobe levels for nonadaptive beams, and must be determined first. After the tapering is fixed, the number of radiating elements can be adjusted to provide the appropriate aperture size to achieve the desired beamwidth. With the number of elements and tapering fixed, the transmit power per element is the last parameter to be adjusted in the simplified design process to achieve the desired sensitivity.

Table 5.1: Functional requirements of an MPAR system to be met by different configurations.

Functional Requirement	**Specification**
Update time	60 s
Sensitivity	0 dB SNR for a -10 dBZ target at 50 km
Spatial resolution	1° beamwidth at ±45° and low sidelobes

5.1.1 Split Transmit Beam Approach

The first simplified design uses the split transmit beam approach to meet the MPAR requirements. A transmit beam that has three main lobes is used in this design, as shown in the top panel of Figure 5.1. The main lobes in the transmit beam are spaced 30° apart to have the maximum angular separation throughout a 90° sector. Pattern synthesis methods can be used to generate such a pattern (Van Trees 2002). However, synthesis of patterns using a phase-only approach to preserve maximum transmit power is more difficult, which is a significant disadvantage of this approach. With the three main lobes in the transmit beam, each lobe only needs to be steered to scan a 30° sector. On receive, three simultaneous receive beams are formed, where each beam points to a direction illuminated by one of the main lobes of the transmit beam. Since the directions of the other two main lobes in the transmit beam are known, deep nulls can be formed in the corresponding directions in a receive beam to attenuate the signals from those directions. Because the directions of the transmit and receive beams are all known, the weights required to generate the desired patterns can be pre-calculated to reduce the computational complexity in a real-time system.

In this approach, since the main lobes in the transmit beam are spaced apart, both the transmit and receive beams contribute to lower the two-way sidelobe

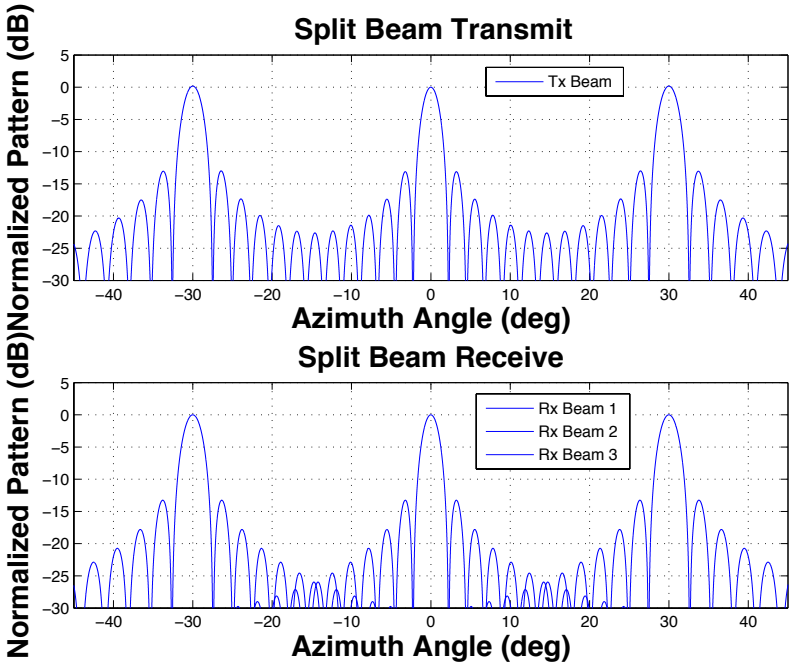

Figure 5.1: Illustration of the split transmit beam approach. A transmit beam (top panel) with three main lobes is used. The main lobes are spaced 30° apart, and each lobe would be steered to scan a 30° sector. On receive, three simultaneous beams are formed, where each receive beam is steered to the pointing direction of one of the main lobes of the transmit beam. The sidelobe levels of a receive beam in the directions of the other main lobes of the transmit beam can be lowered via pattern synthesis to reduce cross-contamination.

levels to meet the MPAR requirements, which allows for less aggressive tapering on receive. The less aggressive receive taper results in less sensitivity loss on receive and a narrower main beam. As a result of the less aggressive receive taper, the split transmit beam approach can achieve the desired 1° beamwidth at a 45° scanning angle with a smaller aperture size. After fixing the number of radiating elements, a transmit power per element can be chosen to provide

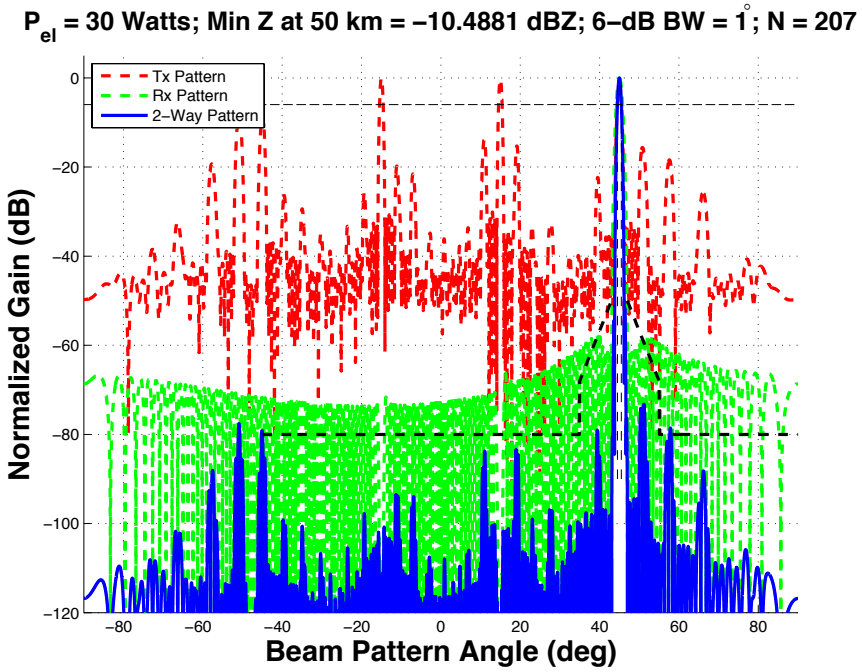

Figure 5.2: A potential configuration that uses the split transmit beam approach to meet MPAR requirements. The array has 207 elements at half-wavelength spacing. The transmit beam pattern (red dashed line) shows three main lobes steered to -15°, 15°, and 45°, respectively. A received beam (green dashed line) is steered to 45°, and sharp nulls are placed at -15° and 15° to attenuate signals from these directions. The two-way pattern (blue line) meets the sidelobe requirements (black dashed line) and has a 1° beamwidth at a 45° scanning angle.

the total transmit power that would achieve the desired sensitivity. One potential configuration that uses the split transmit beam approach to meet the MPAR requirements is an array with 207 elements at half-wavelength spacing with a transmit power of 30 watts per element. Figure 5.2 shows the transmit (red dashed line), receive (green dashed line), and two-way (blue line) beam patterns for this configuration. The transmit beam has main lobes pointed at -15°, 15° and 45°, and a receive beam is steered to 45° in this example. Sharp

nulls located at -15° and 15° are placed in the receive beam pattern to attenuate signals from these directions since it is known that the transmit beam has a main lobe pointed at these directions. A Taylor taper is used on receive to control the sidelobe levels. Despite the high sidelobes in the transmit beam, the two-way sidelobes are below the MPAR requirements (black dashed line), and a 1° beamwidth at 45° scanning angle is achieved. The sensitivity requirement is met as well with a minimum detectable reflectivity of -10.48 dBZ at 50 km.

The interference mitigation ability of the split transmit beam configuration is studied next for a fair comparison with other approaches. In the simulations, an interference signal at 0° is added (with the CSR varying from -10 to 70 dB in 10-dB increments), to a uniform weather profile with a 20-dB SNR. The angular spread of the interference is calculated as described in Chapter 4; it is a measure of the ability to mitigate interference contamination. Figure 5.3 shows the interference mitigation performance for the split transmit beam configuration on a PAR (magenta) and dish-antenna system (red). For a CSR of -10 dB, the interference is weak and does not contaminate the estimates. As the interference signal becomes stronger, both the dish antenna and a PAR antenna using the split transmit beam configuration suffer from increased spread of interference to nearby angles. The difference between two systems is caused

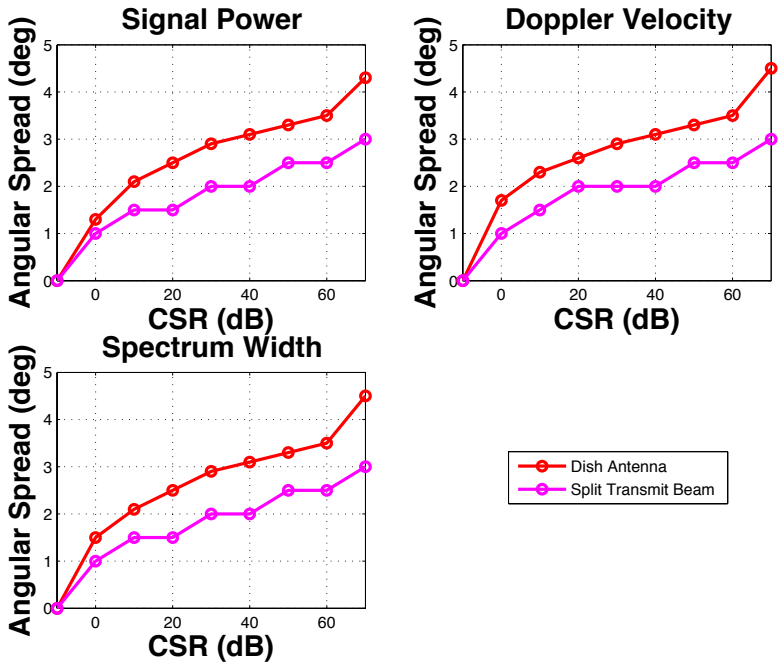

Figure 5.3: Angular spread of interference signal for a PAR using the split transmit beam (magenta) and a dish antenna (red) as a function of the CSRs and for the three spectral moments. For the lowest CSRs, the weak interference signal does not significantly impact the angles near it. As the interference signal becomes stronger, its angular spread increases in all three spectral moments. The PAR with the split transmit beam configuration exhibits a narrower spread compared to that of the dish antenna because the beamwidth of the PAR antenna is narrower than 1° at broadside.

by the narrower beamwidth of the PAR antenna at broadside. If the interference is located near 45°, the performance of the two systems should be similar. Away from the interference source, a PAR using the split transmit beam configuration has accurate estimates with biases close to zero for all three spectral moments, which is expected since its beam pattern is similar to that of the dish antenna by design. Moreover, having a beam pattern that is similar to that of the dish antenna also ensures that a PAR antenna using the split transmit beam

configuration has similar performance as that of a dish antenna when a signal-power gradient is present.

5.1.2 Spoiled Transmit Beam with Nonadaptive Receive Beams Approach

The second simplified design utilizes a spoiled transmit beam in conjunction with nonadaptive receive beams to meet the MPAR requirements. Similar to the split transmit beam case, a minimum of three simultaneous receive beams are needed to meet the timeline requirement. Since nonadaptive receive beams are used, the spoiled transmit beam should be wide enough to encompass the receive beams but narrow enough to reduce the loss of sensitivity and to prevent illuminating unwanted clutter targets. Therefore, a transmit beam that is spoiled to have a beamwidth of 3° is used in this design, and it is steered from -45° to 45° in 3° increments. Figure 5.4 illustrates the spoiled transmit beam (top panel) and the three simultaneous receive beams (bottom panel).

In contrast with the split transmit beam configuration, the angles near the mainlobe of the receive beams are within the 3-dB beamwidth of the transmit beam. Therefore, the two-way sidelobe levels close to the pointing direction are only determined by the one-way sidelobe levels of a receive beam. This implies that aggressive tapering must be used on receive to achieve the sidelobe level requirements. However, aggressive tapering results in loss of sensitivity and increased beamwidth, both of which must be compensated in the design

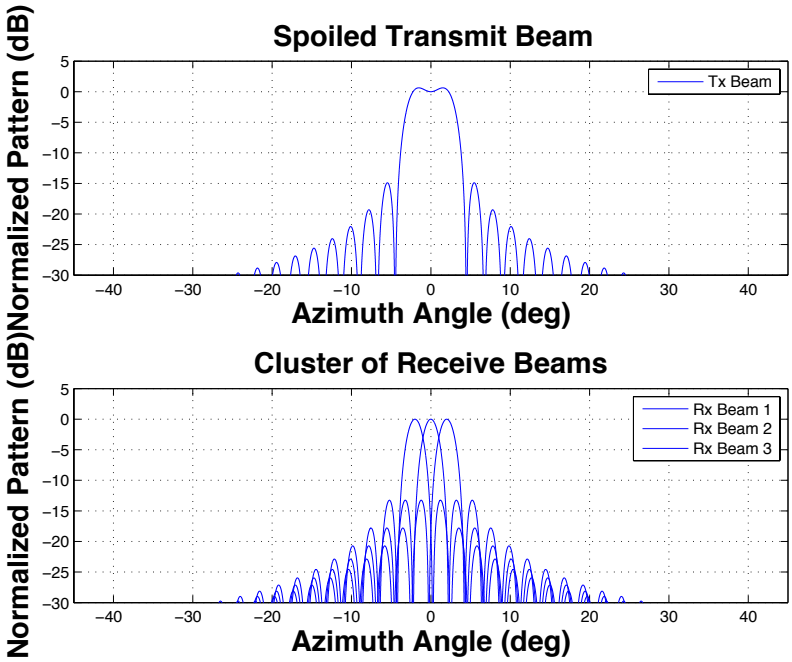

Figure 5.4: Illustration of the spoiled transmit beam with nonadaptive receive beam approach. A spoiled transmit beam with a 3° beamwidth is used. On receive, three simultaneous receive beams are formed to cover the volume illuminated by the transmit beam. In this approach, the transmit beam must be tapered aggressively to meet the two-way sidelobe requirements.

process. To compensate for the increased beamwidth, a larger aperture with more elements is required. With more radiating elements, the transmit power per element is less than that of the split transmit beam configuration, but the total transmit power is comparable. Figure 5.5 shows the transmit, receive and two-way beam pattern for a possible configuration that utilizes a 3° spoiled transmit beam with nonadaptive receive beams. This configuration has an array with 314 elements at half-wavelength spacing, and the transmit power per element is 15 watts. The green dashed line and blue line overlap for angles close to 45°, indicating that the two-way sidelobe levels close to the pointing

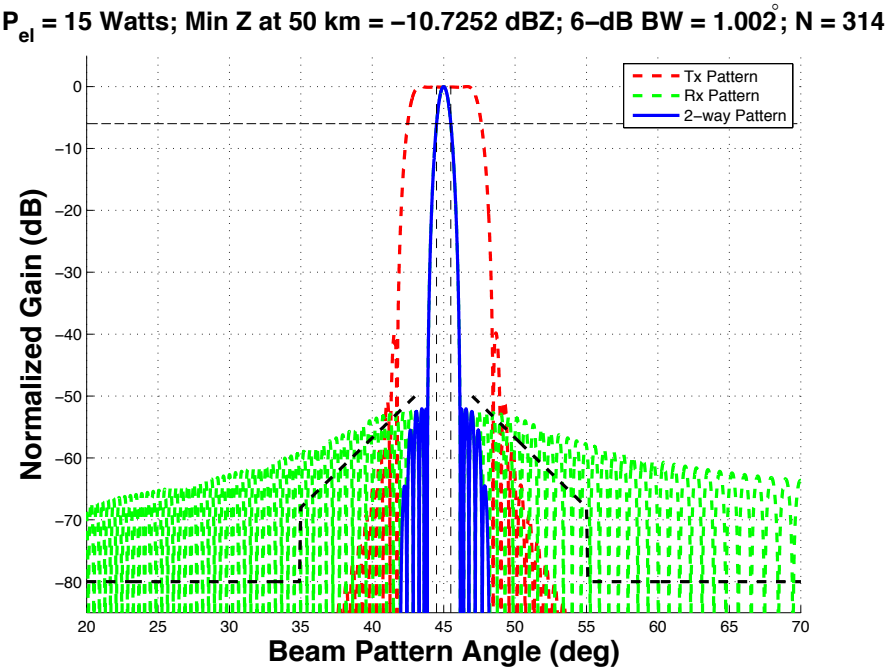

Figure 5.5: A potential configuration that uses the spoiled transmit beam with nonadaptive receive beams to meet MPAR requirements. The array has 314 elements at half-wavelength spacing. The transmit beam pattern (red dashed line) shows the spoiled transmit beam with a 3° beamwidth. A received beam (green dashed line) is steered to 45°. The two-way pattern (blue line) meets the sidelobe requirements (black dashed line) and has a 1° beamwidth at 45° scanning angle.

direction of the receive beam are determined by the one-way sidelobe levels of the receive beam. In this case, a Taylor taper with -54 dB first sidelobe is used to generate the required sidelobe levels. As a result of the aggressive tapering, this array needs to be about 150% the size of the array used in the split transmit beam configuration to achieve the same 1° beamwidth. With the additional radiating elements, the transmit power per element only needs to

be half of that for the split transmit beam case to meet the same sensitivity requirement. A significant advantage of using a spoiled transmit beam instead of a split transmit beam is that the transmit beam is much easier to synthesize and maintain. In a real radar system, hardware imperfections, temperature variations, and other factors play important roles in determining the transmit beam pattern, and the split transmit beam is much more sensitive to these factors than the spoiled transmit beam.

The same interference mitigation test used to assess the split transmit beam configuration was applied to this configuration as well. Figure 5.3 shows the angular spread of the interference signal for different CSRs. The performance of a PAR antenna with the spoiled transmit beam with nonadaptive receive configuration mostly matches that of a comparable PAR antenna with the split transmit beam configuration for CSRs up to 50 dB. This is expected since both configurations were designed to meet the same requirements. For the largest CSRs, the performance of the PAR antenna with the spoiled transmit beam and nonadaptive receive configuration is slightly worse than that of a PAR antenna with the split transmit beam configuration because the two-way sidelobe levels near the steering angle are higher. This results in extra angles near the interference source being contaminated by interference power leaking through the sidelobes. For estimates away from the interference source, the PAR antenna with the spoiled transmit beam and nonadaptive receive beams has near

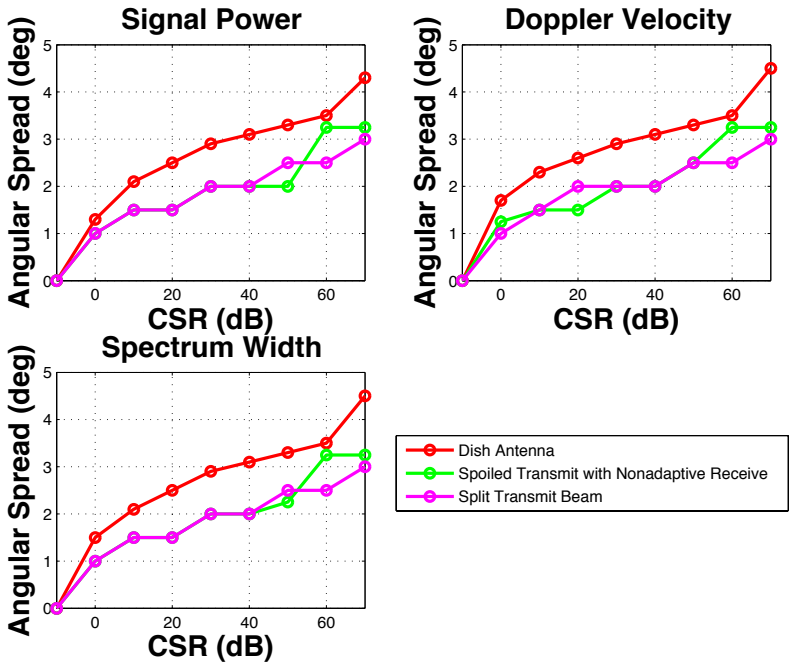

Figure 5.6: Angular spread of interference signal for a PAR antenna with spoiled transmit beam and nonadaptive receive beams (green), a PAR antenna with split transmit beam (magenta) and a dish antenna (red) as a function of the CSR and for the three spectral moments. The performance of the two beamforming approaches is similar across the different CSRs since both configurations were designed to meet the same requirements.

zero biases as expected. When a signal-power gradient is present, a PAR antenna with the spoiled transmit beam and nonadaptive receive beams performs similar to a dish antenna since the nonadaptive beam patterns have the same 1° beamwidth and low sidelobe levels as the dish-antenna beam pattern.

5.1.3 Spoiled Transmit Beam with Adaptive Receive Beams Approach

The final simplified design is a configuration that utilizes spoiled transmit beam with adaptive beams on receive where the proposed adaptive beamspace

algorithm is utilized. Since the proposed adaptive beamspace algorithm requires a set of initial beams centered around the direction of interest, it is perfectly suited for a spoiled transmit beam that would allow these beams to be formed simultaneously. As discussed before, a spoiled transmit beam with a 3° beamwidth is enough to meet the MPAR timeline requirements, but such a spoiled transmit beam would not work well with the proposed adaptive beamspace algorithm since it requires a set of five initial beams, as determined in Chapter 4. If a 3° spoiled beam is used, the set of five 1° initial beams for a direction of interest must span at least three different transmit beams, which would guarentee the received data from at least two receive beams from adjacent transmit beams will have a time-lag that reduces their correlation with the received data from the center beam. As argued in the previous chapter, a reduction in correlation is undesirable when mitigating interference signals with large spectral width, especially white-noise-like interference since it would limit the potential beams that could be used to cancel the interference signal. However, a spoiled transmit beam with a large beamwidth is also undesirable since it results in unnecessary spread of energy, which leads to loss of sensitivity. A larger array with more transmit power per element (more costly) would be needed to compensate for the additional sensitivity loss. In an attempt to minimize cost, a spoiled transmit beam with a 5° beamwidth was chosen for this simplified design as a compromise between best functionality

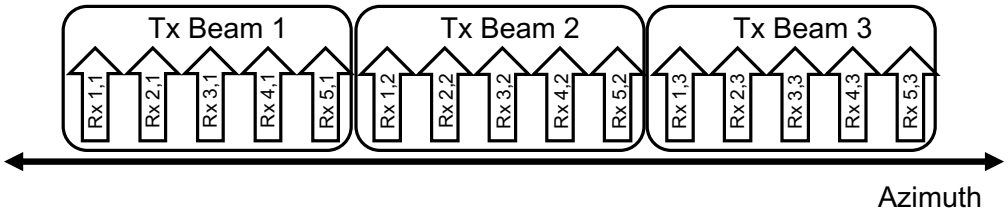

Figure 5.7: Illustration of a concept of operations involving beamspace adaptive processing. A spoiled transmit beam with a 5° beamwidth is used in conjunction with simultaneous receive beams covering the volume illuminated by the transmit beam. For any direction of interest, a contiguous set of five 1° receive beams (regardless of whether they come from the same transmit beam or not) centered on that direction is used as input to the adaptive beamspace algorithm to generate the final estimate for a particular direction.

of the adaptive algorithm and sensitivity loss. The spoiled transmit beam will be steered to scan from -45° to 45° in 5° increments. A benefit of requiring fewer transmit beams to cover the entire 90° sector is that each transmit beam could potentially have a longer dwell time to collect more samples while still meet the timeline requirements for an MPAR system. Both nonadaptive approaches described in previous sections could be implemented with a transmit beam that illuminates 5°, but the cost of the system would increase. Figure 4.4 is repeated here to illustrate the concept of operation.

In this concept of operation, simultaneous receive beams that cover the volume illuminated by the spoiled transmit beam are formed, and the output from these beams must be stored for at least two successive transmit beams. In the example in Figure 5.7, assuming Tx_1 is the first transmit beam, final estimates in the direction of $\mathrm{Rx}_{3,1}$ can be immediately calculated since the

required group of initial beams is available. To calculate the final estimates for angles corresponding to $Rx_{4,1}$ and $Rx_{5,1}$, the output of the receive beams corresponding to Tx_1 must be saved and combined with the output of receive beams from Tx_2. For example, beams $Rx_{2,1}$, $Rx_{3,1}$, $Rx_{4,1}$, $Rx_{5,1}$, and $Rx_{1,2}$ are used in the adaptive algorithm to provide the final estimates for the direction of $Rx_{4,1}$. With the data from Tx_2, final estimates for directions corresponding to $Rx_{4,1}$, $Rx_{5,1}$, $Rx_{1,2}$, $Rx_{2,2}$, and $Rx_{3,2}$ can be made. The data from Tx_3 will then replace the data from Tx_1 and the algorithm can proceed to calculate the final estimates for directions corresponding to $Rx_{4,2}$, $Rx_{5,2}$, $Rx_{1,3}$, $Rx_{2,3}$, and $Rx_{3,3}$. The impact of using initial beams with time-lags was discussed in detail in Chapter 4. The main conclusions from the simulation results are that point interference with wide spectrum width located at the edge of a transmit beam will cause performance degradation, especially for CSRs between 30 and 50 dB. On the other hand, a signal-power gradient located in the middle of a transmit beam is the worst-case scenario for the adaptive beamspace algorithm since both the low side and high side of the gradient are illuminated simultaneously by the transmit beam. However, despite these degradations in performance, the interference spread is still narrower for a PAR antenna with the adaptive beamspace algorithm when compared to that of a dish antenna.

Figure 5.8 shows a potential configuration that uses a PAR antenna with a spoiled transmit beam and adaptive beamspace algorithm on receive to meet

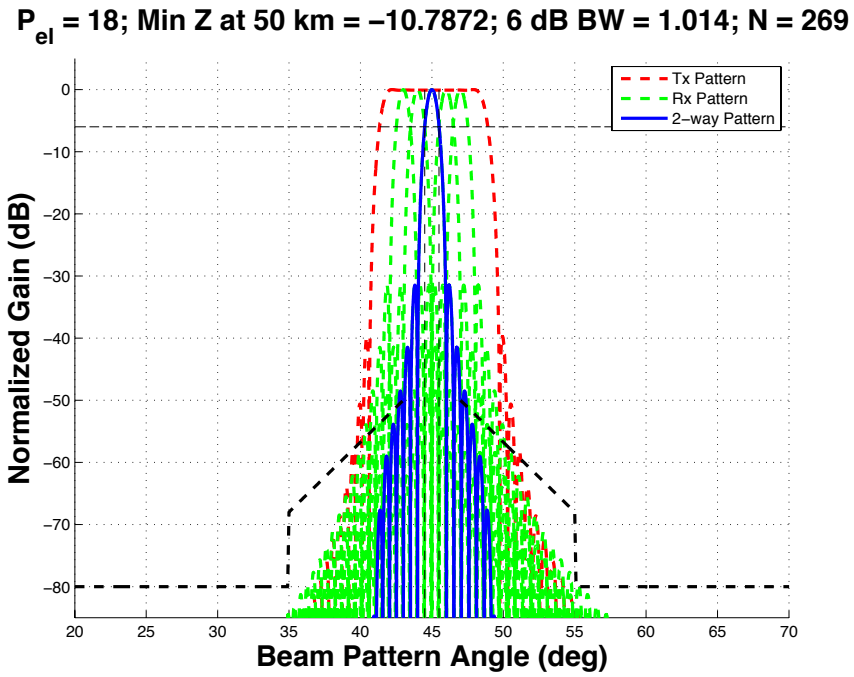

Figure 5.8: A potential configuration that uses the spoiled transmit beam with adaptive beamspace algorithm on receive to meet MPAR requirements. The array has 269 elements at half-wavelength spacing. The transmit beam pattern (red dashed line) shows the spoiled transmit beam with 5° beamwidth. The group of initial beams (green dashed line) is formed within the volume illuminated by the transmit beam. The two-way pattern (blue line) has a 1° beamwidth at 45° scanning angle when only the center beam has non-zero weight.

the MPAR requirements. In this configuration, the array has 269 elements at half-wavelength spacing, and 18 watts of transmit power per element are needed to achieve the sensitivity requirement. The transmit beam (red dashed line) in Figure 5.8 has a beamwidth of 5° at broadside and approximately 7° at a steering angle of 45°. The sensitivity calculation is done using the wider beamwidth to ensure that the configuration still meets the requirements in the worst-case scenario. The two-way beamwidth is harder to calculate

since it depends on the adaptive weights for the side beams, and the adaptive weights depend on the received signal. It is impossible to guarantee that a 1° beamwidth can be achieved for all scenarios. For the simplified design process, the two-way beamwidth is calculated assuming only the center beam has non-zero weight, which is close to the cases where only weather signals are present in the initial beams. Under this assumption, the two-way beamwidth is 1° at a 45° scanning angle, which meets the MPAR requirements. It is also clear that adaptive beam patterns would not meet the sidelobe requirements. However, the stringent sidelobe requirements were developed for nonadaptive beams that must account for the worst-cast scenario at all times. A PAR antenna with adaptive beamspace algorithm, on the other hand, can automatically adjust the sidelobe levels to attenuate unwanted signals, as shown in Figure 4.35. This flexibility to lower sidelobe levels as needed means that adaptive beam patterns do not have to meet the sidelobe requirements at all times. MPAR's functional requirement on data quality is to obtain localized measurements (FAA 2013). To assist in achieving the desired data quality, the sidelobe requirements were developed to reduce biases in resolution volumes with weak signals that are caused by resolution volumes with strong signals. As long as the estimates from the adaptive beamspace algorithm have acceptable biases, whether the beam pattern meets the sidelobe requirements or not

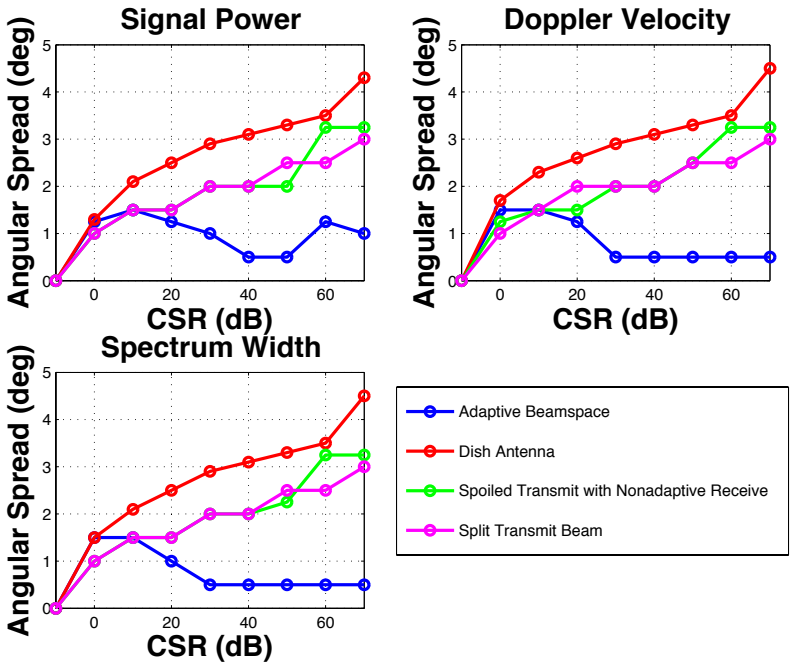

Figure 5.9: Angular spread of interference signal for all configurations as a function of the CSR. The performance of the two nonadaptive beamforming approaches is similar across the different CSRs since both configurations were designed to meet the same requirements. The adaptive beamspace algorithm performs much better than nonadaptive beamforming for CSRs greater than 20 dB.

should not impact its viability as a solution for MPAR to meet its timeline requirements.

Simulations described in previous sections were used to assess the ability of a PAR antenna with the adaptive algorithm to mitigate interference. Figure 5.9 shows the performance of all the different configurations discussed in this chapter. Both PAR antenna with nonadaptive beamforming and the dish antenna show increased angular spread as the interference signal increases in power, which is expected since the sidelobe levels in these configurations are

fixed. Once the interference power exceeds the sidelobe attenuation, more angles would be contaminated by it. For a PAR antenna with the adaptive beamspace algorithm, the performance actually improves for stronger interference signals (greater than 20 dB) because the algorithm can detect the presence of such interference more reliably. By automatically placing nulls in the direction of the interference, the adaptive beamspace algorithm can successfully limit the impact of strong interference sources. This result shows that having adaptivity is much more beneficial to interference mitigation than having sidelobe levels below specified requirements. The gradient simulations in Chapter 4 showed the breakdown point of the adaptive beamspace algorithm. When gradients have step sizes above 60 dB, the higher sidelobe levels cause the adaptive beam configuration to have more angles with large biases when compared to a system with fixed low sidelobe levels. However, gradients with a large step size and a small spatial extent are the least likely to occur (Torlaschi and Humphries 1983). In the more likely situation where the gradients have large step sizes and large spatial extents, the degradation in performance is small. Both of these factors alleviate some of the concerns about the high sidelobe levels produced by the adaptive beamspace algorithm.

5.2 System Comparison

In the previous section, three configurations that meet key MPAR functional requirements were designed in using a simplified process. This section will compare and contrast these different configurations and provide a first order estimate on the cost of each system. Table 5.2 summarizes the different systems.

Table 5.2: Summary of different systems that meet key MPAR functional requirements

	Split Transmit Beam	**Spoiled Transmit Beam with Nonadaptive Receive Beams**	**Spoiled Transmit Beam with Adaptive Receive Beams**
Receive taper	Taylor	Taylor	von Hann
Number of elements in one dimension	207	314	269
Transmit power per element (Watt)	30	15	18
Total transmit power (MW)	1.29	1.48	1.30
Total cost (millions of Dollars)	5.14	5.9	5.21
Sensitivity (dBZ)	-10.5	-10.7	-10.8
Beamwidth (deg)	$\leq$1.0	$\leq$1.0	$\leq$1.0
Angular spread of interference source	Matches dish antenna	Matches dish antenna	Superior to dish antenna
Zone-of-impact of signal-power gradient	Matches dish antenna	Matches dish antenna	Matches dish antenna
Computation Complexity	Simple	Simple	Complex

One of the largest differences between the three configurations is the number of elements required for each. Assume the elements are arranged in a square aperture to provide two dimensional steering, a rough estimate for the number of elements required per face for the split transmit beam configuration, the spoiled transmit beam with nonadaptive receive beam configuration, and

the spoiled transmit beam with adaptive receive beam configuration would be 42,894, 98,596 and 72,361 elements, respectively. The number of elements also translates directly into the aperture size. Assume the radar operates at S-band with a 10-cm wavelength, the diameters of the aperture for the three configurations are 10.35, 15.70, and 13.45 m, respectively. In both measures, a PAR antenna with the split transmit beam configuration can achieve the requirements with the least amount of resources. For configurations using spoiled transmit beams, using adaptive beamforming on receive can result in 27% less radiating elements and 14% smaller aperture compared to those with nonadaptive receive beams. When comparing the required transmit power per element, the situation is reversed where a PAR antenna with the split transmit beam configuration would require the highest transmit power per element while a PAR antenna with the spoiled transmit beam and nonadaptive receive beam configuration would require the lowest transmit power per element. A PAR antenna with the spoiled transmit beam and adaptive receive beam configuration is between the other two options. The total transmit power for a PAR antenna with the split transmit beam configuration or the spoiled transmit beam and adaptive receive beam configuration is approximately 1.3 MW, while a PAR antenna with the spoiled transmit beam and nonadaptive receive beam configuration would require close to 1.5 MW of total transmit power. The number of radiating elements and the transmit power per element directly

affect the cost of the system. As discussed in Chapter 3, each radiating element would require its own transmit/receive (T/R) module with a power amplifier in the all digital architecture. The size consideration alone makes solid-state power amplifiers (SSPA) the most likely choice. Based on current technology, the cost of SSPA is roughly $4 per Watt in peak transmitting power (when purchased in bulk), at current-day prices (Kurdzo 2015). Ignoring the costs of other components in a T/R module, the rough price for a T/R module for each of the three systems listed in Table 5.2 is $120, $60, and $72, respectively. The cost per T/R module multiplied by the number of radiating elements gives the rough estimated cost for each system listed in Table 5.2. A PAR antenna with the split transmit beam configuration or the spoiled transmit beam and adaptive receive beam configuration has a total cost in the range of $5 million, while the total cost for a PAR antenna with the spoiled transmit beam and nonadaptive receive beam is closer to $6 million. Of course this cost estimate is only a rough estimate for a PAR antenna. A more accurate estimate would need to take into consideration the cost of other components (e.g., digital receivers, A/D converters, filters) in the backend of a PAR that increases as a function of the number of elements. Moreover, increased number of elements generally leads to increased system complexity requiring more monitoring and control. It can be expected that a PAR using the spoiled transmit beam and adaptive

receive beam configuration would cost more than a comparable PAR using the spilt transmit beam configuration.

All three proposed configurations have similar beamwidth at a 45° scanning angle. A PAR antenna with the split transmit beam or the spoiled transmit beam and nonadaptive receive beam configuration would meet the sidelobe requirements, which ensures that its performance is similar to that of a dish antenna when a power gradient is present. Simulations in Chapter 4 showed that a PAR antenna using a spoiled transmit beam and the adaptive beamspace algorithm on receive has performance that is similar to that of a dish antenna for power gradients with step sizes up to 50 dB. Gradients with larger step sizes can result in a larger zone of impact for the adaptive beamspace algorithm, but such gradients are unlikely to occur. Simulations also clearly showed that, out of the three configurations, a PAR antenna with adaptive receive beams has the best ability to reject interference signals. Nonadaptive beams can only rely on the sidelobe levels to provide attenuation of interference signals, which is inadequate when the interference signal is strong. In addition, the split transmit beam requires careful calibration of the hardware to maintain the pattern shape, which is difficult to achieve in a real radar system. The trade-off for the improved interference mitigation is increased computational complexity. First, the adaptive weights depend on the receive data; therefore, they cannot be pre-calculated for fast access as in the systems with nonadaptive receive

beams. Second, in the current form, the solution to the optimization problem in the adaptive step requires a significant amount of iterations to find a solution, which makes it impractical to run in real time unless analytical solutions to the optimization problem can be found. Third, as explained in the last section, the adaptive beamspace algorithm requires the storage of received data from two successive transmit beams, which also increases the computational burden. However, the last challenge is not as significant as the other two challenges due to the constant improvement in computational hardware that allows for more data storage and faster access.

Beyond computational concerns, the adaptive beamspace algorithm is also sensitive to errors on the weights, especially when deep nulls are needed to cancel strong interference signals. To test the sensitivity of the adaptive beamspace algorithm to errors on the adaptive weights, white gaussian noise was added to the adaptive weights to simulate errors that represent a sum of all possible error sources. The simulated scenario consists of a uniform weather profile and a 70-dB CSR interference at 0°. Figure 5.10 shows adaptive beam patterns pointed at -2° with no noise (blue line) and noise with -40-dB SNR (red line) added to the adaptive weights. It is clear that by adding the error to the adaptive weights, the resulting beam pattern no longer has a sharp null located at 0° to reject the interference source. In the beam pattern with no added noise, the null depth exceeds 80 dB, more than enough to completely

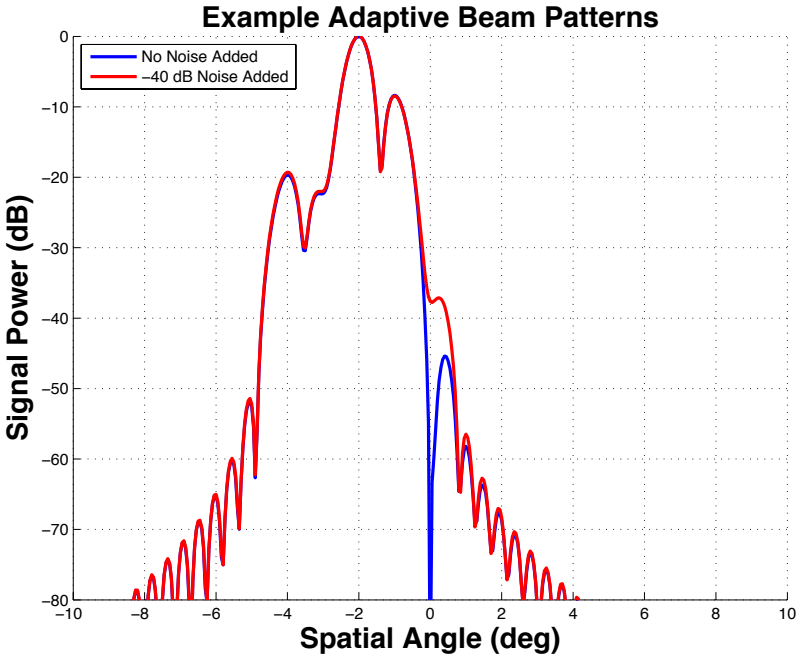

Figure 5.10: Adaptive beam patterns when no noise (blue) and noise with -40-dB SNR (red) was added to the adaptive weights. The errors added to the adaptive weights reduced the depth of the null located at 0° from more than 80 dB to less than 40 dB. Since the interference signal has a CSR of 70 dB, the errors lead to a 30-dB bias in signal-power estimates. In other directions away from the interference, the impact of the errors is minimal.

attenuate the interference signal. In the beam pattern with noise added, the null at 0° disappeared and the sidelobe level at 0° is less than -40 dB, which leads to a 30-dB bias in signal-power estimates. For directions away from 0°, the impact of the added noise is minimal, and the two beam patterns are nearly identical. Figures 5.11 and 5.12 show the cases when noise with -60 and -80-dB SNR was added, respectively. When noise with -60-dB SNR was added to the adaptive weights, the null in the beam pattern was preserved and located in the right direction. However, the null was not deep enough to completely

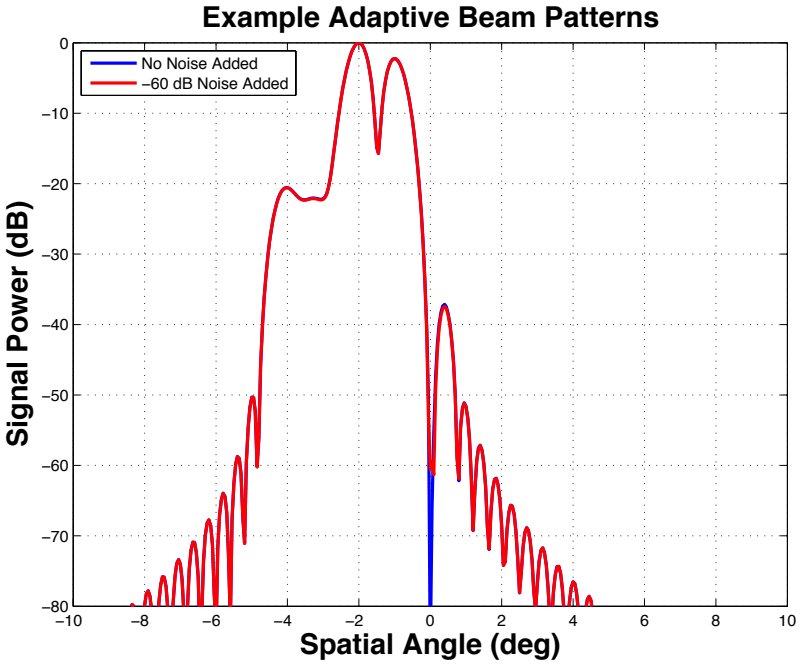

Figure 5.11: Same as Figure 5.10, except noise with -60-dB SNR was added to the adaptive weights. The null at 0° only has a depth of 60 dB, which is not enough to attenuate the interference signal completely.

attenuate the interference signal, resulting in a 10-dB bias in signal-power estimates. When noise with -80-dB SNR is added to the adaptive weights, its impact on the adaptive beam patterns becomes negligible. These simulations showed that errors on the adaptive weights can significantly degrade the interference mitigation performance of the adaptive beamspace algorithm, and efforts such as consistent hardware calibration and minimization of quantization noise should be made to reduce the magnitude of the errors as much as possible.

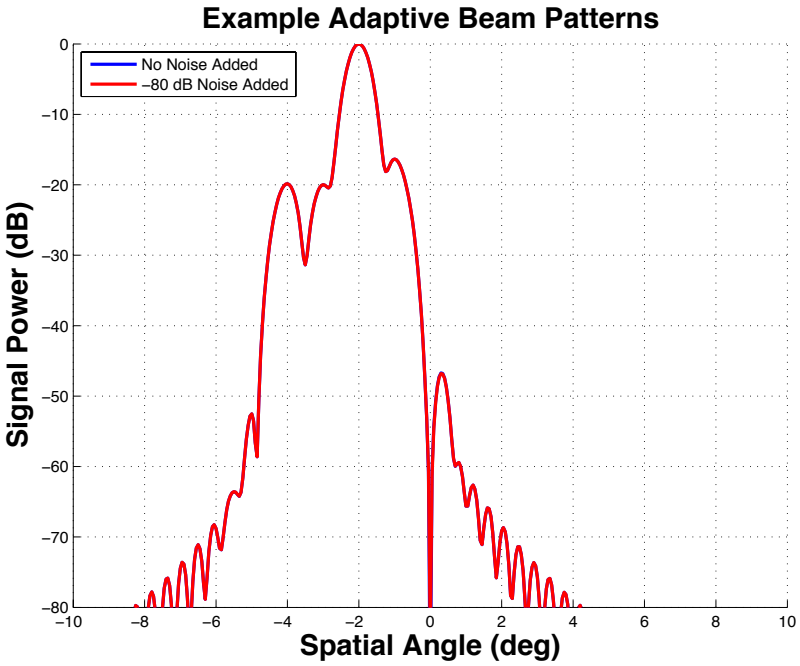

Figure 5.12: Same as Figure 5.10, except noise with -80-dB SNR was added to the adaptive weights. The added error has negligible impact on the beam pattern for all directions, and the interference signal is attenuated by the null at 0°.

Chapter 6

Conclusions and Future Work

In order to protect people and property from hazardous weather, the NWS utilizes a weather radar network to monitor the atmosphere and to provide early warnings for severe weather. Despite continuous upgrades to the hardware and software, there is still a desire for more rapid volumetric updates, which can lead to increased warning lead times and warning confidence levels in tornado, severe hail, and high-wind events. Phased-array radars have been shown to be a natural candidate to achieve the desired update time. Moreover, there are multiple radar networks in the USA for aviation missions, such as the TDWR, ASR, and ARSR networks. The operational and maintenance cost of these single-mission radars can be greatly reduced if their functionality can be combined into a multifunction phased-array radar (MPAR). With the WSR-88D nearing its expected lifetime, an MPAR network has been proposed where each radar can perform the weather surveillance function of the WSR-88D and the aviation-support functions of the TDWR, ASR, and ARSR. Since an MPAR system must complete both weather and aircraft surveillance missions, the update time reduction provided by having multiple faces is insufficient to

achieve the desired 60 second update time for weather surveillance. Therefore, it is likely that multiple beams per face will be needed to meet the timeline requirements. There are many different ways to achieve multiple scanning beams including multiple frequencies, time multiplexing, and beamforming approaches. In the category of beamforming approaches, a potential solution is to use a spoiled transmit beam and to form a cluster of simultaneous receive beams. This approach is attractive because the transmit and receive beams are relatively simple to generate and maintain compared to more exotic transmit beams that have multiple main lobes. However, a significant challenge for this approach is the potential of high sidelobe levels in the two-way pattern, which can result in significantly biased estimates of the spectral moments in situations where the signal power has large spatial variations. Nonadaptive beams must be tapered aggressively to drive down the sidelobe levels to meet the specifications, which leads to loss of sensitivity and spatial resolution. On the other hand, adaptive beamforming can automatically adjust the sidelobe levels to attenuate unwanted signals. By having the flexibility to adjust the sidelobe levels automatically, adaptive beams do not have to meet the sidelobe requirements for the worst-case scenario. In most cases, the worst-case scenario is not present, and the adaptive beams can trade higher sidelobe levels for better spatial resolution. There are many adaptive beamforming methods in the literature, but most are designed to operate on signals from discrete point targets.

When applied to distributed targets that are of interest to weather radars, the existing adaptive beamforming methods result in biased estimates of the radar variables. Furthermore, the uncontrolled behavior of the sidelobes prevents a straightforward calibration process to convert from signal power to reflectivity factor, which is the quantity of interest for quantitative precipitation estimation (QPE), for example.

To address these issues of adaptive beamforming for weather radar applications, an adaptive beamspace algorithm was developed and presented in this dissertation. The proposed adaptive beamspace algorithm is a two-step process that first forms a set of deterministic beams and feeds the output of the deterministic beams into an adaptive algorithm to generate the final output time-series that can be used directly to estimate the radar variables. Since the number of initial beams is usually much smaller than the number of receiving elements, the data dimensionality of the adaptive algorithm is significantly reduced, which leads to requiring smaller number of samples and reduced computational complexity when compared to adaptive algorithms that operate in element space. However, reduced data dimensionality results in loss of degrees of freedom that could be used to reject interference signals. The adaptive algorithm solves an optimization problem that seeks to minimize the total output power while ensuring that signals from the direction of interest

are minimally distorted. The novelty of the proposed adaptive beamspace algorithm is the additional adaptive weight magnitude constraints that must be met. These adaptive weight magnitude constraints are designed to balance two competing goals: to minimize the interference power and to prevent cancellation of weather signals. When interference cancellation is required, the adaptive weights are unconstrained, which ensures that signals in the side beams are properly scaled and phase-shifted to cancel the interference signal in the center beam. Otherwise, the adaptive weights are constrained to be at least one order of magnitude smaller than the weight for the center beam, which prevents cancellation of weather signals and minimizes the adverse effects of combining signals from different resolution volumes.

Simulations were used to determine the appropriate choices for the parameters of the adaptive beamspace algorithm. It was shown that as the number of initial beams increased, the signal-power estimates became more negatively biased, which is caused by weather signal cancellation allowed by the increased degrees of freedom. Similarly, negative biases in signal-power estimates occurred when the initial beams were spaced closely together, which is the result of having highly correlated outputs from the initial beams. From these simulations, it was determined that having five initial beams spaced 1° apart results in near-zero biases. A von Hann taper was chosen as the taper of the initial beams because its fast roll off away from the main lobe helps shape the final

beam pattern away from the pointing direction. The higher sidelobe levels near the main lobe were not a concern because the adaptive algorithm determines the sidelobe levels of the final beam pattern in those directions. The correlation threshold used to determine which beam contains interference signal was set to 0.75 based on simulation results showing near-zero biases for a range of CSRs that are most challenging to the algorithm. Similarly, the weight magnitude constraint was set to 0.1 based simulation results showing zero biases in the estimates of the spectral moments.

With the algorithm parameters determined, the adaptive beamspace algorithm was evaluated with two scenarios that could result in significant biases in estimates of the radar variables. The first scenario involves an interference source in a uniform weather profile, which is designed to evaluate the algorithm's ability to automatically mitigate interference signals. Simulation results showed that the adaptive beamspace algorithm can significantly reduce the angles impacted by the interference signal compared to a dish-antenna system with low sidelobe levels. For all simulated CSRs, the impact of the interference signal is the same or smaller for the adaptive beamspace algorithm compared to that for the dish-antenna system. For interference with CSRs greater than 20 dB, the adaptive beamspace algorithm limited the angles impacted by the interference signal to less than half of that for dish-antenna system. In the extreme 70-dB CSR case, the angles impacted by the interference

signal were reduced from close to 4° to 1°. The adaptive beamspace algorithm also showed no significant performance degradation for SNRs greater than 0 dB. Due to a finite transmit beam width, in some cases the initial beams are from different transmit beams, and the time-lag could impact the performance of the algorithm, especially when the interference signal has large spectrum width. This situation is most likely to occur when the interference is located near the edge of a transmit beam, and simulations confirmed the degradation in performance. However, even in this worst-case scenario, the adaptive beamspace algorithm still reduced the impact of the interference signal compared to that for a dish-antenna system.

The second scenario used to evaluate the adaptive beamspace algorithm involves signal-power gradients. MPAR's functional requirement on data quality is to obtain localized measurements, and the sidelobe requirements for non-adaptive beams were designed to reduce biases in resolution volumes with weak signals that are caused by resolution volumes with strong signals. As long as the estimates from the adaptive beamspace algorithm have acceptable biases, the beam pattern does not have to meet the sidelobe requirements. Simulations showed that the proposed adaptive beamspace algorithm can have similar performance as the dish-antenna system for gradients up to 50 dB in step size. For gradients with larger step sizes, the adaptive beamspace algorithm results in more angles having large biases. However, these gradients

with large step size and small spatial extent are quite unlikely to occur in practice. The improved performance of the adaptive beamspace algorithm as the gradients shifted from the edge of the scanning range to the broadside of the array is mainly due to the narrowing of the main lobe that occurs naturally in all phased-array systems. Moreover, unlike the interference case, gradients located near the edge of a transmit beam lead to improved performance due to the gradient not being illuminated simultaneously. In both the interference and gradient scenarios, for angles away from the contamination source, the adaptive beamspace algorithm produced estimates with near-zero biases when compared to estimates produced by a dish-antenna system. This supports that in weather-only situations, the adaptive beamspace algorithm can produce accurate and calibrated estimates. Real data collected by the AIR were used to demonstrate that the adaptive beamspace algorithm can perform spatial filtering of ground clutter signals, and the weather estimates were qualitatively comparable to nonadaptive beamforming results.

Since there are many different beamforming approaches to achieve the desired multiple beams in an MPAR system, the proposed adaptive beamspace algorithm was compared to other potential configurations to determine the advantages and limitations of each approach. A simplified design process was used to design three configurations that met MPAR requirements regarding update time, sensitivity, and spatial resolution. A PAR antenna using the split

transmit beam approach requires the least elements and the smallest aperture size, but requires the highest transmit power per element. A PAR antenna with a spoiled transmit beam and nonadaptive receive beams requires the most elements and the largest aperture size, but the least transmit power per element. A PAR antenna with a spoiled transmit beam and adaptive receive beams that utilizes the proposed adaptive beamspace algorithm is between the two nonadaptive approaches in terms of amount of elements and transmit power per element. Assuming solid-state power amplifiers (SSPA) that have prices linearly related to the transmit power per element are used in the T/R modules, a first-order cost estimation showed that a PAR antenna with the split transmit beam or the spoiled transmit beam and adaptive beamspace on receive configuration would have a similar cost while a PAR antenna with the spoiled transmit beam and nonadaptive receive beam configuration would be costly. When the cost of the backend of a PAR is taken into consideration, it can be expected that a PAR using the spoiled transmit beam and adaptive receive beam configuration would cost more than a PAR using the split transmit beam configuration. Both nonadaptive approaches are computationally simple since the weights only need to be calculated once, but do not offer any interference rejection except the natural sidelobe attenuation. In addition, the split transmit beam requires careful calibration of the hardware to maintain the pattern shape, which is difficult to achieve in a real radar system. The configuration utilizing adaptive

beamspace on receive is computationally complex due to the need to recalculate the adaptive weights and to store data from successive transmit beams. However, its ability to reject interference signals is superior compared to configurations with nonadaptive receive beams. The interference rejection ability also makes the adaptive beamspace algorithm sensitive to adaptive weights errors. Simulations showed that if the error is large enough, the nulls in the adaptive beam pattern to attenuate the interference signal would become shallow, which leads to large biases in signal-power estimates. All three proposed configurations have similar beamwidth at a 45° scanning angle, and have similar performance to that of a dish antenna when a signal-power gradient is present.

In summary, it has been shown that the proposed adaptive beamspace algorithm can produce accurate and calibrated estimates of the spectral moments. The algorithm can automatically adjust the sidelobe levels to reject interference and clutter, and can also produce estimates similar to those of a low-sidelobe dish-antenna system in the presence of signal-power gradients despite its higher sidelobe levels. Moreover, preliminary analysis has shown that the adaptive beamspace algorithm used in conjunction with a spoiled transmit beam is a viable configuration that can meet the timeline, sensitivity, and spatial resolution requirements of an MPAR. Compared to configurations that have nonadaptive receive beams, having adaptive receive beams formed with

the adaptive beamspace algorithm can lead to superior interference rejection. The major trade-off is increased computational complexity. With advances in computing technology, the additional computational burden should not be a major concern for an upgradable MPAR system with an expected life span longer than 30 years.

6.1 Future Work

The next steps for further development of the adaptive beamspace algorithm should focus on three aspects:

- Evaluate its performance in estimating the polarimetric variables.
- Analyze the impact of non-ideal components on the performance of the algorithm.
- Find an analytical or approximate solution to the optimization problem that can speed up the calculation of adaptive weights to facilitate real-time implementation of the algorithm.

Since this is the first time that adaptive beamspace algorithm is applied to weather radar, the work focused on estimation of the spectral moments to simplify the analysis of the first-order trade-offs. However, future MPAR systems will have polarimetric capabilities and the impact of using adaptive beamforming on the estimation of polarimetric variables must be analyzed. When beam

patterns for the horizontal and vertical polarization are mismatched, it is possible that different adaptive weights can be applied to the different polarizations to mitigate the effects of the mismatched patterns. Furthermore, polarization dependent adaptivity could offer new ways to filter out unwanted signals that are difficult to distinguish in time, frequency, or space. Similarly, the sensitivity of the adaptive algorithm to different sources of errors was not analyzed thoroughly in this study. In Chapter 5, a preliminary analysis showed that small errors on the adaptive weights can significantly change the adaptive beam pattern, resulting in a failure to reject interference signals. The impact of other sources of error such as steering vector error and covariance matrix errors that impact traditional adaptive beamforming algorithms has not been considered in detail. Lastly, the optimization problem in the adaptive step is currently solved using the iterative interior-point method in MATLAB's optimization toolbox. Unless an analytical or approximate solution that can be calculated efficiently is found, the real-time implementation of the adaptive beamspace algorithm will be challenging.

References

Bienvenu, G. and L. Kopp, 1984: Decreasing high resolution method sensitivity by conventional beamformer preprocessing. *Acoustics, Speech, and Signal Processing, IEEE International Conference on ICASSP '84.*, volume 9, 714–717.

Bodine, D. J., M. R. Kumjian, R. D. Palmer, P. L. Heinselman, and A. V. Ryzhkov, 2013: Tornado damage estimation using polarimetric radar. *Wea. Forecasting*, **28**, 139–158.

Bowden, K. A. and P. L. Heinselman, 2016: A qualitative analysis of NWS forecasters' use of phased-array radar data during severe hail and wind events. *Weather and Forecasting*, **31**, 43–55.

Bowden, K. A., P. L. Heinselman, D. M. Kingfield, and R. P. Thomas, 2015: Impacts of phased-array radar data on forecaster performance during severe hail and wind events. *Weather and Forecasting*, **30**, 389–404.

Brandes, E. A., G. Zhang, and J. Vivekanandan, 2004a: Comparison of polarimetric radar drop size distribution retrieval algorithms. *J. Atmos. Oceanic Technol.*, **21**, 584–598.

—, 2004b: Drop size distribution retrieval with polarimetric radar: Model and application. *J. Appl. Meteor.*, **43**, 461–475.

Bringi, V. N. and V. Chandrasekar, 2001: *Polarimetric Doppler Weather Radar: Principles and Applications*. Cambridge University Press.

Brookner, E. and J. Howell, 1986: Adaptive-adaptive array processing. *Proceedings of the IEEE*, **74**, 602–604.

Brown, R. A., L. R. Lemon, and D. W. Burgess, 1978: Tornado detection by pulsed Doppler radar. *Mon. Wea. Rev.*, **106**, 29–38.

Byrd, R., J. C. Gilbert, and J. Nocedal, 2000: A trust region method based on interior point techniques for nonlinear programming. *Mathematical Programming*, **89**, 149–185.

Cao, Q., G. Zhang, E. A. Brandes, and T. J. Schuur, 2010: Polarimetric radar rain estimation through retrieval of drop size distribution using a Bayesian approach. *J. Appl. Meteor. Climatol.*, **49**, 973–990.

Capon, J., 1969: High-resolution frequency-wavenumber spectrum analysis. *Proceedings of the IEEE*, **57**, 1408–1418.

Carbone, R. E., M. J. Carpenter, and C. D. Burghart, 1985: Doppler radar sampling limitations in convective storms. *Journal of Atmospheric and Oceanic Technology*, **2**, 357–361.

Chapman, D., 1976: Partial adaptivity for the large array. *Antennas and Propagation, IEEE Transactions on*, **24**, 685–696.

Cheong, B. L., M. W. Hoffman, R. D. Palmer, S. J. Frasier, and F. J. López-Dekker, 2004: Pulse pair beamforming and the effects of relfectivity field variations on imaging radars. *Radio Science*, **39**, 1–13.

Cheong, B. L., R. Kelley, R. D. Palmer, Y. Zhang, M. Yeary, and T. Y. Yu, 2013: PX-1000: A solid-state polarimetric X-band weather radar and time–frequency multiplexed waveform for blind range mitigation. *IEEE Transactions on Instrumentation and Measurement*, **62**, 3064–3072.

Chilson, P. B., W. F. Frick, P. M. Stepanian, J. R. Shipley, T. H. Kunz, and J. F. Kelly, 2012: Estimating animal densities in the aerosphere using weather radar: To Z or not to Z? *Ecosphere*, **3**, art72.

Chrisman, J. N., 2012: Automated volume scan evaluation and termination (AVSET). Technical report, Radar Operation Center.

—, 2014: Multiple elevation scan option for sails (MESO-SAILS). Technical report, Radar Operation Center.
URL `http://www.roc.noaa.gov/wsr88d/PublicDocs/NewTechnology/MESO-SAILS_Description_Briefing_Jan_2014.pdf`

Cox, H., R. Zeskind, and M. Owen, 1987: Robust adaptive beamforming. *Acoustics, Speech and Signal Processing, IEEE Transactions on*, **35**, 1365–1376.

Crum, T. and R. Alberty, 1993: The WSR-88D and the WSR-88D Operational Support Facility. *Bull. Amer. Meteor. Soc.*, **74**, 1669–1687.

Crum, T., S. Smith, J. Chrisman, R. Vogt, M. Istok, R. Hall, and B. Saffle, 2013: WSR-88D radar projects 2013 update. *EIPT, 29th Conference on*, Austin, TX.

Curtis, C. D. and S. M. Torres, 2011: Adaptive range oversampling to achieve faster scanning on the National Weather Radar Testbed phased-array radar. *Journal of Atmospheric and Oceanic Technology*, **28**, 1581–1597.

Doviak, R. J. and D. S. Zrnić, 1993: *Doppler Radar and Weather Observations*. Dover Publictions, Inc., 2nd edition.

Elnashar, A., S. Elnoubi, and H. El-Mikati, 2006: Further study on robust adaptive beamforming with optimum diagonal loading. *Antennas and Propagation, IEEE Transactions on*, **54**, 3647–3658.

Er, M. and A. Cantoni, 1985: An alternative formulation for an optimum beamformer with robustness capability. *Communications, Radar and Signal Processing, IEE Proceedings F*, **132**, 447–460.

FAA, 2013: Multifunction phased array radar: Notional functional requirements document and clarifications. Technical Report Version 2.2 16 pp.

Fadlallah, N., M. Rammal, H. Rammal, P. Vaudon, R. Ghayoula, and A. Gharsallah, 2008: General synthesis method for linear phased antenna array. *Microwaves, Antennas Propagation, IET*, **2**, 338–342.

FMH, Apr. 2006: *Federal Meteorological Handbook No. 11: Doppler Radar Meteorological Observations*. Washington, D.C., USA, FCM-H11C-2006.

French, M. M., D. W. Burgess, E. R. Mansell, and L. J. Wicker, 2015: Bulk hook echo raindrop sizes retrieved using mobile, polarimetric Doppler radar observations. *J. Appl. Meteor. Climatol.*, in press.

Frick, W. F., P. M. Stepanian, J. F. Kelly, K. W. Howard, C. M. Kuster, T. H. Kunz, and P. B. Chilson, 2012: Climate and weather impact timing of emergence of bats. *PLoS ONE*, **7**, e42737.

Fulton, C., M. Yeary, D. Thompson, J. Lake, and A. Mitchell, 2016: Digital phased arrays: Challenges and opportunities. *Proceedings of the IEEE*, **104**, 487–503.

Harris, F., 1978: On the use of windows for harmonic analysis with the discrete Fourier transform. *Proceedings of the IEEE*, **66**, 51–83.

Hassanien, A. and S. Vorobyov, 2009: A robust adaptive dimension reduction technique with application to array processing. *Signal Processing Letters, IEEE*, **16**, 22–25.

Heinselman, P., D. LaDue, D. M. Kingfield, and R. Hoffman, 2015: Tornado warning decisions using phased-array radar data. *Weather and Forecasting*, **30**, 57–78.

Heinselman, P. L., D. S. LaDue, and H. Lazrus, 2012: Exploring impacts of rapid-scan radar data on NWS warning decisions. *Weather and Forecasting*, **27**, 1031–1044.

Heinselman, P. L., D. L. Priegnitz, K. L. Manross, T. M. Smith, and R. W. Adams, 2008: Rapid sampling of severe storms by the National Weather Radar Testbed phased array radar. *Weather and Forecasting*, **23**, 808–824.

Heinselman, P. L. and S. M. Torres, 2011: High-temporal-resolution capabilities of the National Weather Radar Testbed phased-array radar. *Journal of Applied Meteorology and Climatology*, **50**, 579–593.

Hood, K., S. Torres, and R. Palmer, 2010: Automatic detection of wind turbine clutter for weather radars. *Journal of Atmospheric and Oceanic Technology*, **27**, 1868–1880.

Horton, K. G., P. M. Stepanian, C. E. Wainwright, and A. K. Tegeler, 2015: Influence of atmospheric properties on detection of wood-warbler nocturnal flight calls. *International Journal of Biometeorology*, 1–10.

Ice, R., A. K. Heck, J. G. Cunningham, W. D. Zittel, R. R. Lee, L. M. Richardson, and B. J. McGuire, 2015: Polarimetric weather radar calibration using solar scans. *31st Conference on Environmental Information Processing Technologies*.

Isom, B., R. Palmer, R. Kelley, J. Meier, D. Bodine, M. Yeary, B.-L. Cheong, Y. Zhang, T.-Y. Yu, and M. I. Biggerstaff, 2013: The Atmospheric Imaging Radar: Simultaneous volumetric observations using a phased array weather radar. *Journal of Atmospheric and Oceanic Technology*, **30**, 655–675.

Isom, B. M., R. D. Palmer, G. S. Secrest, R. D. Rhoton, D. Saxion, T. L. Allmon, J. Reed, T. Crum, and R. Vogt, 2009: Detailed observations of wind turbine clutter with scanning weather radars. *Journal of Atmospheric and Oceanic Technology*, **26**, 894–910.

Kumjian, M. R., 2013: Principles and applications of dual polarization weather radar. Part I: Description of the polarimetric radar variables. *J. Oper. Meteor*, **1**, 226–242.

Kumjian, M. R. and A. V. Ryzhkov, 2008: Polarimetric signatures in supercell thunderstorms. *J. Appl. Meteor. Climatol.*, **47**, 1940–1961.

Kurdzo, J. M., 2015: *Pulse compression waveforms and applications for weather radar*. Ph.D. dissertation, Univerisity of Oklahoma.

Kurdzo, J. M., F. Nai, D. J. Bodine, T. A. Bonin, R. D. Palmer, B. L. Cheong, J. Lujan, A. Mahre, and A. Byrd, 2017: Observations of severe local storms and tornadoes with the Atmospheric Imaging Radar. *Bulletin of the American Meteorological Society*, in press.

LaDue, D. S., P. L. Heinselman, and J. F. Newman, 2010: Strengths and limitations of current radar systems for two stakeholder groups in the southern plains. *Bulletin of the American Meteorological Society*, **91**, 899–910.

Lamare, R. D., L. Wang, and R. Fa, 2010: Adaptive reduced-rank LCMV beamforming algorithms based on joint iterative optimization of filters: Design and analysis. *Signal Processing*, **90**, 640 – 652.

Lazo, J. K., M. Lawson, P. H. Larsen, and D. M. Waldman, 2011: U.S. economic sensitivity to weather variability. *Bulletin of the American Meteorological Society*, **92**, 709–720.

Li, F. and H. Liu, 1994: Statistical analysis of beam-space estimation for direction-of-arrivals. *Signal Processing, IEEE Transactions on*, **42**, 604–610.

Li, J., P. Stoica, and Z. Wang, 2003: On robust Capon beamforming and diagonal loading. *Signal Processing, IEEE Transactions on*, **51**, 1702–1715.

—, 2004: Doubly constrained robust Capon beamformer. *Signal Processing, IEEE Transactions on*, **52**, 2407–2423.

Li, M. and Y. Lu, 2006: Dimension reduction for array processing with robust interference cancellation. *Aerospace and Electronic Systems, IEEE Transactions on*, **42**, 103–112.

Lie, J., X. Li, W. Ser, C. See, and L. Lei, 2010: Adaptive uncertainty based iterative robust Capon beamformer. *Acoustics Speech and Signal Processing (ICASSP), 2010 IEEE International Conference on*, 2526 –2529.

Melnikov, V., R. Doviak, and D. Zrnić, 2015: A method to increase the scanning rate of phased-array weather radar. *Geoscience and Remote Sensing, IEEE Transactions on*, **53**, 5634–5643.

Michelson, M., W. Shrader, and J. Wieler, 1990: Terminal Doppler Weather Radar. *Microwave Journal*, **33**, 139–148.

Miller, L. J. and R. A. Kropfli, 1980: The multiple radar workshop, November 29179. Part II: Experimental design and procedures. *Bulletin of the American Meteorological Society*, **61**, 1173–1177.

Nai, F., S. Torres, and R. Palmer, 2013a: Adaptive beamforming for weather observations using the Atmospheric Imaging Radar. *Phased Array Systems Technology, 2013 IEEE International Symposium on*, 709–713.

—, 2013b: On the mitigation of wind turbine clutter for weather radars using range-Doppler spectral processing. *Radar, Sonar Navigation, IET*, **7**, 178–190.

Nai, F., S. M. Torres, and R. D. Palmer, 2016: Adaptive beamspace processing for phased-array weather radars. *IEEE Transactions on Geoscience and Remote Sensing*, **54**, 5688–5698.

National Centers for Environmental Information (NCEI), 2016: U.S. billion-dollar weather and climate disasters.
URL `https://www.ncdc.noaa.gov/billions/`

Nilsen, C. and I. Hafizovic, 2009: Beamspace adaptive beamforming for ultrasound imaging. *Ultrasonics, Ferroelectrics and Frequency Control, IEEE Transactions on*, **56**, 2187–2197.

Nuttall, A., 1981: Some windows with very good sidelobe behavior. *IEEE Transactions on Acoustics, Speech, and Signal Processing*, **29**, 84–91.

Palmer, R. D., S. Gopalam, T.-Y. Yu, and S. Fukao, 1998: Coherent radar imaging using Capon's method. *Radio Science*, **33**, 1585–1598.

Park, H. S., A. V. Ryzhkov, D. S. Zrnić, and K.-E. Kim, 2009: The hydrometeor classification algorithm for the polarimetric WSR-88D: Description and application to an MCS. *Wea. Forecasting*, **24**, 730–748.

Priegnitz, D., P. Heinselman, and R. Brown, 2014: Adaptive storm-based scanning at the National Weather Radar Testbed phased-array radar. *Proc. 30th Conf. Environ. Inf. Process. Technol.*.

Reinoso-Rondinel, R., T.-Y. Yu, and S. Torres, 2010: Multifunction phased-array radar: Time balance scheduler for adaptive weather sensing. *Journal of Atmospheric and Oceanic Technology*, **27**, 1854–1867.

ROC, 2013: Description document supplemental adaptive intra-volume low-level scan (sails). Technical report, Radar Operation Center.
URL `http://www.roc.noaa.gov/wsr88d/PublicDocs/NewTechnology/Supplemental_Adaptive_Intra_Volume_Low_Level_Scan_Description_Document_Final.pdf`

Rockney, V., 1958: The WSR-57 radar. *Proc. Seventh Conf. on Weather Radar*, Amer. Meteor. Soc., Miami Beach, FL, F14–F20.

Rodriguez-Rivera, A., B. Baryshnikov, B. Van Veen, and R. Wakai, 2006: MEG and EEG source localization in beamspace. *Biomedical Engineering, IEEE Transactions on*, **53**, 430–441.

Ryzhkov, A., D. Burgess, D. Zrnić, T. Smith, and S. Giangrande, 2002: Polarimetric analysis of a 3 May 1999 tornado. *Preprints, 21st Conf. on Severe Local Storms*, Amer. Meteor. Soc., San Antonio, TX.

Ryzhkov, A. V., S. E. Giangrande, and T. J. Schuur, 2005a: Rainfall estimation with a polarimetric prototype of WSR-88D. *J. Appl. Meteor. Climatol.*, **44**, 502–515.

Ryzhkov, A. V., T. J. Schurr, D. W. Burgess, and D. Zrnić, 2005b: Polarimetric tornado detection. *J. Appl. Meteor. Climatol.*, **44**, 557–570.

Serafin, R. J. and J. W. Wilson, 2000: Operational weather radar in the United States: Progress and opportunity. *Bulletin of the American Meteorological Society*, **81**, 501–518.

Siggia, A. and R. Passarelli, 2004: Gaussian model adaptive processing (GMAP) for improved ground clutter cancellation and moment calculation. *Proceedings of ERAD-2004*, 67–73.

Simmons, K. M. and D. Sutter, 2005: WSR-88D radar, tornado warnings, and tornado casualties. *Weather and Forecasting*, **20**, 301–310.

Skolnik, M. I., 2001: *Introduction to Radar Systems*. McGraw Hill.

Somasundaram, S., 2011: Reduced dimension robust Capon beamforming for large aperture passive sonar arrays. *Radar, Sonar Navigation, IET*, **5**, 707–715.

Stepanian, P. M. and K. G. Horton, 2015: Extracting migrant flight orientation profiles using polarimetric radar. *IEEE Transactions on Geoscience and Remote Sensing*, **53**, 6518–6528.

Stoica, P. and R. Moses, 2005: *Spectral Analysis of Signals*. Pearson Education, Inc., Upper Saddle River, New Jersey.

The U.S. Natural Hazard Statistics, 2016: Weather fatalities. URL `http://www.nws.noaa.gov/om/hazstats/resources/weather_fatalities.pdf`

Torlaschi, E. and R. G. Humphries, 1983: Statistics of reflectivity gradients. *21st Conference on Radar Meteorology*, 173–175.

Torres, S. M., R. Adams, C. D. Curtis, E. Forren, D. E. Forsyth, I. R. Ivić, D. Priegnitz, J. Thompson, and D. A. Warde, 2016: Adaptive-weather-surveillance and multifunction capabilities of the National Weather Radar Testbed phased array radar. *Proceedings of the IEEE*, **104**, 660–672.

Torres, S. M. and D. S. Zrnić, 1999: Ground clutter canceling with a regression filter. *Journal of Atmospheric and Oceanic Technology*, **16**, 1364–1372.

Van Trees, H. L., 2002: *Optimum Array Processing Part IV of Detection, Estimation, and Modulation Theory*. A John Wiley & Sons, Publication, Inc.

Vook, F. W., T. A. Thomas, and E. Visotsky, 2013: Elevation beamforming with beamspace methods for LTE. *Personal Indoor and Mobile Radio Communications (PIMRC), 2013 IEEE 24th International Symposium on*, 554–558.

Warde, D. and S. Torres, 2009: Automatic detection and removal of ground clutter contamination on weather radars. *34th International Conference on Radar Meteorology, Williamsburg, VA.*.

Weadon, M., P. Heinselman, D. Forsyth, J. Kimpel, W. E. Benner, and G. S. Torok, 2009: Multifunction phased array radar. *Bulletin of the American Meteorological Society*, **90**, 385–389.

Weber, M. E., J. Y. N. Cho, J. S. Herd, J. M. Flavin, W. E. Benner, and G. S. Torok, 2007: The next-generation multimission U.S. surveillance radar network. *Bulletin of the American Meteorological Society*, **88**, 1739–1751.

Whiton, R. C., P. L. Smith, S. G. Bigler, K. E. Wilk, and A. C. Harbuck, 1998: History of operational use of weather radar by U.S. weather services. Part I: The pre-NEXRAD era. *Wea. Forecasting*, **13**, 219–243.

Wilson, J. W., R. D. Roberts, C. Kessinger, and J. McCarthy, 1984: Microburst wind structure and evaluation of Doppler radar for airport wind shear detection. *Journal of Climate and Applied Meteorology*, **23**, 898–915.

Wolfson, M., R. Delanoy, B. Forman, R. Hallowell, M. Pawlak, and P. Smith, 1994: Automated microburst wind-shear prediction. *Lincoln Laboratory Journal*, **7**, 399–426.

Xu, G., S. Silverstein, R. Roy, and T. Kailath, 1994: Beamspace ESPRIT. *Signal Processing, IEEE Transactions on*, **42**, 349–356.

Yoshikawa, E., T. Ushio, Z. Kawasaki, S. Yoshida, T. Morimoto, F. Mizutani, and M. Wada, 2013: MMSE beam forming on fast-scanning phased array weather radar. *Geoscience and Remote Sensing, IEEE Transactions on*, **51**, 3077–3088.

Yu, T., R. Rondinel, and R. Palmer, 2009: Investigation of non-Gaussian Doppler spectra observed by weather radar in a tornadic supercell. *Journal of Atmospheric and Oceanic Technology*, **26**, 444–461.

Yu, T.-Y., M. B. Orescanin, C. D. Curtis, D. S. Zrnić, and D. E. Forsyth, 2007: Beam multiplexing using the phased-array weather radar. *Journal of Atmospheric and Oceanic Technology*, **24**, 616–626.

Zhang, G., R. J. Doviak, D. S. Zrnić, J. Crain, D. Staiman, and Y. Al-Rashid, 2009: Phased array radar polarimetry for weather sensing: A theoretical formulation for bias corrections. *IEEE Transactions on Geoscience and Remote Sensing*, **47**, 3679–3689.

Zhang, G., R. J. Doviak, D. S. Zrnić, R. Palmer, L. Lei, and Y. Al-Rashid, 2011: Polarimetric phased-array radar for weather measurement: A planar or cylindrical configuration? *Journal of Atmospheric and Oceanic Technology*, **28**, 63–73.

Zoltowski, M., G. Kautz, and S. Silverstein, 1993: Beamspace Root-MUSIC. *Signal Processing, IEEE Transactions on*, **41**, 344–364.

Zrnić, D., V. Melnikov, R. Doviak, and R. D. Palmer, 2015: Scanning strategy for the multifunction phased-array radar to satisfy aviation and meteorological needs. *Geoscience and Remote Sensing Letters, IEEE*, **12**, 1204–1208.

Zrnić, D. S., 1975: Simulation of weatherlike Doppler spectra and signals. *Journal of Applied Meteorology and Climatology*, **14**, 619–620.

Zrnić, D. S., J. F. Kimpel, D. E. Forsyth, A. Shapiro, G. Crain, R. Ferek, J. Heimmer, W. Benner, T. J. McNellis, and R. J. Vogt, 2007: Agile-beam phased array radar for weather observations. *Bulletin of the American Meteorological Society*, **88**, 1753–1766.

Appendix A : List of Acronyms

ACF	Autocorrelation Function
A/D	Analog to Digital
AIR	Atmospheric Imaging Radar
ARRC	Advanced Radar Research Center
ARSR	Air Route Surveillance Radar
ASR	Airport Surveillance Radar
ATC	Air Traffic Control
AVSET	Automated Volume Scan Evaluation and Termination
C-band	IEEE band classification for 5 cm-wavelength
CLEAN-AP	Clutter Environment Analysis using Adaptive Processing
CPPAR	Cylindrical Polarimetric Phased Array Radar
CSR	Clutter-to-Signal Ratio
DDS	Direct Digital Synthesizer
DSD	Drop Size Distribution
DTFT	Discrete-Time Fourier Transform
ESPIRT	Estimation of Signal Parameters by Rotational Invariance Techniques
FAA	Federal Aviation Administration
GCF	Ground Clutter Filter
GMAP	Gaussian Model Adaptive Processing
IEEE	Institute of Electrical and Electronics Engineers
I/Q	In-Phased and Quadrature

LPF	Low Pass Filter
MESO-SAILS	Multiple Elevation Scan Option for SAILS
MMSE	Minimum Mean Squared Error
MPAR	Multi-Function Phased Array Radar
MUSIC	Multiple Signal Characterization
MVDR	Minimum Variance Distortionless Response
NCEI	National Center for Environmental Information
NOAA	National Oceanic and Atmospheric Administration
NWRT	National Weather Radar Testbed
NWS	National Weather Service
OU	University of Oklahoma
PAIR	Polarimetric Atmospheric Imaging Radar
PAR	Phased Array Radar
PARISE	Phased-Array Innovative Sensing Experiment
PPI	Plan-Position Indicator
PRF	Pulse Repetition Frequency
PRT	Pulse Repetition Time
QPE	Quantitative Precipitation Estimation
RCB	Robust Capon Beamformer
RF	Radio Frequency
RHI	Range-Height Indicator
ROC	Radar Operations Center
S-band	IEEE band classification for 10 cm-wavelength
SAILS	Supplemental Adaptive Intra-Volume Low-Level Scan

SNR	Signal-to-Noise Ratio
SSPA	Solid-State Power Amplifier
STALO	Stable Local Oscillator
TDWR	Terminal Doppler Weather Radar
T/R	Transmit/Receive
ULA	Uniform Linear Array
USA	United States of America
VCP	Volume Coverage Pattern
WSR-57	Weather Surveillance Radar-1957
WSR-74	Weather Surveillance Radar-1974
WSR-88D	Weather Surveillance Radar-1988 Doppler
WTC	Wind Turbine Clutter
X-band	IEEE band classification for 3 cm-wavelength
Xcvr	Transceiver

Appendix B : List of Commonly Used Symbols

$\mathbf{a}(\theta)$	steering vector
$\mathbf{A}$	steering vector matrix
$\|A\|$	amplitude of received signal, m^2
c	speed of light, m s^{-1}
$\mathbf{C}$	constraint matrix
d	separation between adjacent elements, m
D	drop diameter, mm
f_o	carrier frequency, Hz
f_r	normalized receive beam pattern
f_s	sampling frequency, Hz
f_t	normalized transmit beam pattern
$f(t)$	transmit signal
g_r	directive gain of receive antenna
g_t	directive gain of transmit antenna
H	step size of gradient
$H_d(\theta)$	desired beam pattern
$\mathbf{I}$	identity matrix
$I(t,r)$	in-phase component
K_{DP}	specific differential phase, rad km^{-1}
K_w	complex refractive index, unitless
l	losses, unitless
L	number of sources
M	number of samples
$\mathbf{n}$	white noise vector

N	number of elements
$N(D)$	drop size distribution
N_o	mean noise power, W
P	signal power profile
$\overline{P}$	expected receive power, W
P_r	received signal power, W
P_t	peak transmit power, W
$Q(t,r)$	quadarture component
r	range, m
r_a	maximum unambiguous range, m
r_b	blind range, m
r_0	range to resolution volume, m
$\mathbf{R}$	covariance matrix
$R(lT_s)$	autocorrelation function
S	signal power, W
$\mathbf{S}$	source signal matrix
$S(f)$	Doppler spectrum
$s(t)$	received signal of first element
$s_n(t)$	received signal of nth element
t	time, s
$\mathbf{T}$	beamforming matrix
T_d	dwell time, s
T_s	pulse repetition time, s
$U(t)$	pulse modulation function
v_a	maximum unambiguous velocity, m s^{-1}
v_r	radial velocity, m s^{-1}

$V(t,r)$	received signal
V	resolution volume, m^3
$\mathbf{w}(\theta)$	complex weight vector
$\mathbf{w}_B$	beamspace weight vector
$W(r)$	range weighting function
$\mathbf{x}$	received data vector
$\mathbf{X}$	received data matrix
$y(t)$	output of beamformer
$y_B(t)$	output of adaptive beamspace algorithm
Z	reflectivity factor, $mm^6\ m^{-3}$
Z_e	equivalent reflectivity factor, $mm^6\ m^{-3}$
Z_{DR}	differential reflectivity, dB
Δr	range resolution, m
$\Delta\theta$	separation between initial beams, degree
ε	squared error between beam patterns
η	reflectivity, m^{-1}
θ	elevation angle, degree
λ	wavelength, m
ρ_{hv}	correlation coefficient, unitless
σ_b	backscattering cross-section, m^2
σ_v	spectrum width, $m\ s^{-1}$
τ	pulse width, s
τ_s	range-time sampling delay, s
ϕ	azimuth angle, degree
ϕ_{DP}	differential phase, rad
ψ_e	phase of received signal, rad

ψ_s	backscattering phase, rad
ψ_t	initial transmitter phase, rad
ω_d	Dopper shift, rad s^{-1}

Appendix C : Index